

Final work : Computational Study of the Unsteady Pressure Around a 2D Circular Cylinder Undergoing Forced Motion

Auteur : Jauntsarats Sacedo, Oier

Promoteur(s) : Dimitriadis, Grigorios

Faculté : Faculté des Sciences appliquées

Diplôme : Master en ingénieur civil en aérospatiale, à finalité spécialisée en "turbomachinery aeromechanics (THRUST)"

Année académique : 2019-2020

URI/URL : <http://hdl.handle.net/2268.2/10379>

Avertissement à l'attention des usagers :

Tous les documents placés en accès ouvert sur le site le site MatheO sont protégés par le droit d'auteur. Conformément aux principes énoncés par la "Budapest Open Access Initiative"(BOAI, 2002), l'utilisateur du site peut lire, télécharger, copier, transmettre, imprimer, chercher ou faire un lien vers le texte intégral de ces documents, les disséquer pour les indexer, s'en servir de données pour un logiciel, ou s'en servir à toute autre fin légale (ou prévue par la réglementation relative au droit d'auteur). Toute utilisation du document à des fins commerciales est strictement interdite.

Par ailleurs, l'utilisateur s'engage à respecter les droits moraux de l'auteur, principalement le droit à l'intégrité de l'oeuvre et le droit de paternité et ce dans toute utilisation que l'utilisateur entreprend. Ainsi, à titre d'exemple, lorsqu'il reproduira un document par extrait ou dans son intégralité, l'utilisateur citera de manière complète les sources telles que mentionnées ci-dessus. Toute utilisation non explicitement autorisée ci-avant (telle que par exemple, la modification du document ou son résumé) nécessite l'autorisation préalable et expresse des auteurs ou de leurs ayants droit.



UNIVERSITY OF LIÈGE - FACULTY OF APPLIED
SCIENCES

Computational Study of the Unsteady Pressure Around a 2D Circular Cylinder Undergoing Forced Motion

*End of studies work done with a view to obtaining the master's degree" Civil
Engineer in Aerospace, professional focus in "Turbomachinery Aeromechanics
(THRUST)"*

by OIER JAUNTSARATS SACEDO

Advisors: Prof. G. Dimitriadis (ULiège)
Prof. R. E. Kielb (Duke University)
Jury: Prof. T Andrianne (ULiège)

Academic Year 2019-2020



*Ze ederra izango den itzulera
Elkarren besoen zabalera
Zure fede guztiei eustea
Zure bi malkoak baretzea.*

Errefuxiatuena, Izaro Andrés

Abstract

The flow over bluff bodies, either static or oscillating, has always been a challenge to be modelled by numerical methods. Due to their geometrical shape, the separation of the flow over them is inherent. The fluid-flow in the wake is highly unsteady and due to the natural instability of the periodic vortex shedding process, oscillatory fluid forces will arise over the circular cylinders. As a response to such excitation, freely supported cylinders can trigger a self-excited oscillatory motion. This aeroelastic behaviour is called Vortex Induced Vibration. However, an imposed sinusoidal motion at a specific frequency and amplitude can excite the natural behaviour of the wake and modify it completely. Consequently, the unsteady loading over the circular cylinder will be modified too.

The unsteady behaviour of the airflow over circular cylinders under imposed motion is the case studied in the present report. In order to do that a CFD code based on a 2D fluid domain has been built and validated against experimental data. Scale Adaptive SST Transition turbulence model resulted in the best option in terms of accuracy of the results and efficiency of the computational cost of the numerical simulations.

The different combinations (amplitude & frequency) of the imposed sinusoidal motion can be split into two big groups: unlocked cases (vortex shedding frequency follows the Strouhal law) and locked cases (vortex shedding frequency equals the imposed frequency of the motion). The second can also be subdivided in two: imposed motions that result in an energy transmission from the fluid to the structure, and the ones causing the energy to move in opposite direction.

The time signal of lift coefficient, which oscillates at a main frequency close to the shedding frequency, presents two differentiated behaviours. Amongst unlocked cases, it has two predominant components; at the oscillating frequency and at the Strouhal frequency, being the second one the greatest. However, switching to closer values of imposed motion to the shedding frequency that respects the Strouhal law, the amplitude of the first component increases until it overcomes the second one resulting in the synchronization of both frequencies. Amongst the locked cases, the lift coefficient has only one predominant component at the shedding frequency which equates the oscillating.

The time-varying pressure coefficient is analyzed over the cylinder for different imposed motions. The circular section can be divided in two. In the front part of it, the main frequency of the time signal equates the imposed motion. In the rare of the cylinder, however, it is composed basically by the frequency of the vortex shedding process and its multiple higher harmonics. Between both, a transition region exists for the unlocked cases.

Comparison against results extracted from the mid-span section of a 3D cylinder demonstrates that both computational simulations present similar overall trends of the aerodynamic parameters as a function of the imposed motion. However, deviations are found in the numerical values even if the results from both computations (3D & 2D) show similar order of magnitude.

Acknowledgements

The development of the present research project and submission of the report finishes the two year-long MSc. THRUST joint degree. This programme gave me an international experience at KTH University (Sweden) and Université de Liège (Belgium) during the studies and the development of the thesis at Duke University (North Carolina).

First of all, I would like to thank Dr. Robert Kielb for admitting me in Duke Aeroelasticity research group at Pratt School Engineering even if the team was already pretty big the last academic year. The availability to work in the experimental NSV group at Duke, and more specifically in the experimental NSV cylinder team, helped me to develop myself as part of a working group. Furthermore, I appreciate the academic support given by Dr. Dowell, Dr. Virgin and Dr. Hall for the wise and useful advice proposed to the working team for the design of the experimental test rig. Special mention to Ricky Hollenbach, who coordinated the group I was working with.

Secondly, I would like to express my gratitude to Prof. Greg Dimitriadis and Prof. Thomas Andrianne for their help, attention and support in the project. They showed a great interest on it from the beginning and made available all the facilities and material that they had.

I would like to highlight the special understanding of Prof. Greg Dimitriadis, Prof. Thomas Andrianne and Prof. Robert Kielb of the Covid-19 worldwide pandemia and how the situation of the current research project was handled. The closure of Duke University facilities resulted in the inability to make the correspondent measurements of the test rig. The professors presented a professional behaviour all the time trying to set an alternative numerical project of mutual interest.

Special thanks to all the members of my family and my closest friends who supported me emotionally and psychologically during the hard moments. First, both while I was in EEUU and on my way back home during the pandemic situation. Secondly, during the preventive 14 days self-quarantined in my room. Eventually, the following 2 months until the locked-down in Spain was over.

Finally, I would like to thank all my peers of the THRUST programme for the last two years. On the one hand, the ones who came to Liège (Simón, Luca, Harish and Martina) which was great to have them in that intense experience. Also, the new people met there. On the other hand, the ones I shared my experience at Duke with (Yann, Bas, Davide, Sivanand and Anil). It was a really short stay but they made it fun and easygoing.

Contents

Nomenclature	vii
List of Figures	xii
List of Tables	xviii
1 Introduction	1
2 Unsteady Flow Over Circular Cylinders	3
2.1 Numerical Modelling of the Flow Around Static Cylinders	8
2.2 Circular Cylinders undergoing Vortex Induced Vibrations	10
2.3 Flow over Oscillating Circular Cylinder under Imposed Motion	12
3 Experimental Results	18
3.1 Introduction	18
3.2 Wind Tunnel	18
3.3 Test Rig	19
3.4 Measurement Systems	19
3.5 Testing Conditions	20
3.6 General VIV Results	21
3.6.1 Modal Properties of the Cylinder and the Supporting Structure	21
3.6.2 Displacement of the Cylinder	22
3.6.3 Lock-in Region	23
3.7 Cases for CFD Code Validation	24
3.7.1 Case at $U_\infty = 1.4839$ [m/s] ($Re \sim 1 \cdot 10^4$)	24
3.7.2 Case at $U_\infty = 4.2786$ [m/s] ($Re \sim 2.9 \cdot 10^4$)	28
4 CFD Code Validation: 2D Static Cylinder	32
4.1 Introduction	32
4.2 Computational Domain	32
4.3 Numerical Grid and Mesh Independence Study	33
4.3.1 Steady Parameters	33
4.3.2 Time Dependent Parameters	35
4.3.3 Results and Conclusions	36
4.4 Boundary Conditions	37
4.5 Convergence Criteria	38
4.6 Discretization and Solution Schemes	39
4.7 Time Step Size	39
4.8 Running Procedure	40
4.9 Turbulence Model Selection	41
4.10 Conclusions	42
5 CFD Code Validation: 3D Static Cylinder	44
5.1 Introduction	44
5.2 Computational Domain	44
5.3 Grid and Mesh Independence Study	44

5.4	Boundary Conditions	46
5.5	Simulation Procedure & Set-Up	46
5.6	Results and Validation	46
5.6.1	Lift and Drag Coefficients	46
5.6.2	Shedding Frequency & Strouhal Number	48
5.6.3	Time Mean 3D Loading	49
5.7	Conclusions	50
6	CFD Code Validation: 2D Moving Cylinder	51
6.1	Introduction	51
6.2	Computational Domain and Boundary Conditions	51
6.3	Mesh and its Dynamic Properties	52
6.4	Discretization and Solution Schemes	53
6.5	Convergence Criteria	53
6.6	Time Step Size	54
6.7	Turbulence Model Selection	57
6.8	Number of Iterations per Time Step	57
6.9	Running Procedure	58
6.10	Results and Validation	59
6.10.1	Lift and Drag Coefficients	59
6.10.2	Shedding Frequency (f_{vs})	60
6.10.3	Time Mean 2D Loading	61
6.11	Conclusions	62
7	Study of Lock-in Region	64
7.1	Introduction	64
7.2	Analyzed Cases	65
7.3	Analysis at constant Imposed Amplitude ($\frac{ y }{D}$)	66
7.3.1	$c_L(t)$: Frequency Content	66
7.3.2	$c_L(t)$: Amplitude ($ c_L $) and Phase (ϕ_L)	68
7.3.3	Time Mean Pressure Coefficient: \bar{c}_p	70
7.3.4	Wake Mode	73
7.3.5	Energy Transfer	74
7.4	Analysis at constant Imposed Frequency (f_{osc}/f_{vs}^o)	76
7.4.1	$c_L(t)$: Amplitude ($ c_L $), Frequency (f_{vs}) & phase (ϕ_L)	76
7.4.2	Time Mean Pressure Coefficient: \bar{c}_p	78
7.4.3	Wake Mode	81
8	Evolution of the Unsteady Pressure over Oscillating Circular Cylinders	83
8.1	Introduction	83
8.2	Analysis of the time signal of the pressure coefficient	83
8.2.1	Locked Cases	84
8.2.2	Unlocked Cases	87
8.3	Conclusions	89

9	Comparison between 2D & 3D Results	91
9.1	Lock-in Region	91
9.2	Time-varying lift coefficient	92
9.2.1	Main frequencies of the time signals $c_L(t)$ & $C_L(t)$	92
9.2.2	Amplitude of the main frequency: $ c_L $ & $ C_L $	92
9.2.3	Phase difference of the main frequency with respect to $y(t)$: ϕ_L	94
9.3	Unsteady pressure over the cylinder: $c_p(t)$	94
10	Conclusions	97
10.1	Conclusions on the Project	97
10.2	Further Research on the Topic	100
A	Definition of the Aerodynamic Coefficients	101
A.1	Introduction	101
A.2	Time Mean Value of the Pressure Coefficient: \bar{c}_p	101
A.3	ANSYS Fluent: Monitored $C_{L_{mo}}$ and $C_{D_{mo}}$	102
A.4	C_L & C_D from Literature	103
A.5	Experimental $C_{L_{exp}}$ & $C_{D_{exp}}$	104
A.6	ANSYS Fluent: Manually Defined $C_{L_{ma}}$ and $C_{D_{ma}}$	104
B	Basics of SIMPLE and PISO Algorithms	105
B.1	Pressure-Velocity Coupling Algorithm	106
C	Derivation of the Scalar Expression for Vorticity	108
D	Energy Transfer per Cycle	109
	References	111

Nomenclature

Abbreviations

1D	One dimensional
2D	Two dimensional
3D	Three Dimensional
Ave.	Spatial Average
BL	Boundary Layer
CFD	Computational Fluid Dynamics
CPU	Central Processing Unit
DDES	Delayed Detached Eddy Simulation
DES	Detached Eddy Simulation
DNS	Direct Numerical Simulation
DOF	Degree of Freedom
FEA	Finite Element Analysis
FEM	Finite Element Method
FFT	Fast Fourier Transform
IDDES	Improved Delayed Detached Eddy Simulation
LES	Large Eddy Simulation
LS	Laminar Separation
max	Maximum
NSE	Navier Stokes Equations
P	Pair of Vortices
RANS	Reynolds-Averaged Navier-Stokes
RMS	Root Mean Square
RSM	Reynolds Stress Model
S	Single Vortex
SAS	Scale-Adaptive Simultion
SST	Shear Stress Transport

STD Standard Deviation

TS Turbulent Separation

UDF User Defined Function

URANS Unsteady Reynolds-Averaged Navier-Stokes

VIV Vortex Induced Vibrations

Symbols

α	Diffusion Parameter	$[-]$
$\bar{\tau}_{wall}$	Mean value of the wall shear stress time distribution	$[Pa]$
\bar{C}_D	Time mean value of the time signal of the 3D drag coefficient	$[-]$
\bar{c}_D	Time mean value of the time signal of the 2D drag coefficient	$[-]$
\bar{c}_f	Mean value of the skin friction coefficient time distribution	$[-]$
\bar{C}_L	Time mean value of the time signal of the 3D lift coefficient	$[-]$
\bar{c}_L	Time mean value of the time signal of the 2D lift coefficient	$[-]$
\bar{c}_p	Mean value of the pressure coefficient time distribution	$[-]$
\bar{m}_{out}	Spatial average of the time mean mass flow rate at the outlet boundary	$[kg/s]$
\bar{u}	Time mean value of the u component of the wake velocity	$[m/s]$
\bar{u}_{out}	Spatial average of the time mean of streamwise component of velocity at the outlet boundary	$[m/s]$
\bar{v}	Time mean value of v component of the wake velocity	$[m/s]$
\bar{v}_{out}	Spatial average of the time mean velocity at the outlet boundary	$[m/s]$
\bar{w}	Time mean value of w component of the wake velocity	$[m/s]$
Δt	Time step size	$[s]$
\dot{m}_{out}	Spatial average of the steady mass flow rate at the outlet boundary	$[kg/s]$
$\dot{y}(t)$	Time signal of the velocity of the cylinder	$[m/s]$
γ	Diffusion Coefficient	$[-]$
λ	Wavelength	$[m]$
μ	Dynamic Viscosity	$[Pa \cdot s]$
μ_t	Turbulent Dynamic Viscosity	$[Pa \cdot s]$

NOMENCLATURE

ν	Kinematic Viscosity	$[Pa \cdot s]$
ν_t	Turbulent Kinematic Viscosity	$[Pa \cdot s]$
$\Omega, \vec{\Omega}$	Vorticity	$[1/s]$
ϕ_L	Phase difference between the component related to the main frequency of the 2D lift coefficient and the motion of the cylinder	$[^\circ]$
π	Pi number	$[-]$
ρ	Density of air	$[kg/m^3]$
ρ_{ref}	Reference density	$[kg/m^3]$
τ	Wall Shear Stress	$[Pa]$
τ_x	Wall Shear Stress component in x direction	$[Pa]$
τ_y	Wall Shear Stress component in y direction	$[Pa]$
τ_z	Wall Shear Stress component in z direction	$[Pa]$
φ	Angular coordinate over the mid-span section of the cylinder	$[^\circ]$
ζ_n	Damping ratio of the structure	$[-]$
A	Surface area	$[m^2]$
C_D	Steady State 3D drag coefficient	$[-]$
c_D	Steady State 2D drag coefficient	$[-]$
$C_D(t)$	Time signal of the 3D drag coefficient	$[-]$
$c_D(t)$	Time signal of the 2D drag coefficient	$[-]$
c_E	Energy transmission coefficient	$[-]$
C_L	Steady State 3D lift coefficient	$[-]$
c_L	Steady State 2D lift coefficient	$[-]$
$C_L(t)$	Time signal of the 3D lift coefficient	$[-]$
$c_L(t)$	Time signal of the 2D lift coefficient	$[-]$
c_p	Steady State pressure coefficient	$[-]$
$c_p(t)$	Time signal of the pressure coefficient	$[-]$
$c_{D_{exp}}$	Drag coefficient extracted from the midsection of the cylinder in the wind tunnel	$[-]$
$C_{D_{ma}}$	Manually defined 3D Drag coefficient on ANSYS Fluent for comparison with experimental data	$[-]$

$c_{D_{ma}}$	Manually defined 2D Drag coefficient on ANSYS Fluent for comparison with experimental data	[—]
$C_{D_{mo}}$	Monitored 3D Drag coefficient on ANSYS Fluent	[—]
$c_{D_{mo}}$	Monitored 2D Drag coefficient on ANSYS Fluent	[—]
$c_{L_{exp}}$	Lift coefficient extracted from the midsection of the cylinder in the wind tunnel	[—]
$C_{L_{ma}}$	Manually defined 3D Lift coefficient on ANSYS Fluent for comparison with experimental data	[—]
$c_{L_{ma}}$	Manually defined 2D Lift coefficient on ANSYS Fluent for comparison with experimental data	[—]
$C_{L_{mo}}$	Monitored 3D Lift coefficient on ANSYS Fluent	[—]
$c_{L_{mo}}$	Monitored 2D Lift coefficient on ANSYS Fluent	[—]
D	Diameter of the cylinder	[m]
d	Normalized distance to the nearest wall boundary	[—]
$D(t)$	Time signal of the drag force on the cylinder	[N]
E_{cycle}	Energy Transmission within the aeroelastic system in one cycle of motion	[J]
F_D	Force on the cylinder in the direction of the fluid-flow	[N]
F_L	Force on the cylinder in the perpendicular direction of the fluid-flow	[N]
f_s	Sampling Frequency	[Hz]
f_n	Natural Frequency of the Structure	[Hz]
f_{osc}, f_e, f_f, N	Imposed motion frequency of the Cylinder	[Hz]
f_{vs}, n	Vortex Shedding Frequency	[Hz]
f_{vs}^o	Static Vortex Shedding Frequency	[Hz]
i	Index of the spatial discretization over the cylinder	[—]
j	Index of the temporal discretization	[—]
L	Length of the cylinder in span-wise direction (z-coordinate)	[m]
$L(t)$	Time signal of the lift force on the cylinder	[N]
M	Mach number	[—]
n	Index of the spatial discretization with in the fluid volume mesh	[—]
N_z	Number of discrete points on the cylinder in span-wise direction	[—]

NOMENCLATURE

p_{atm}	Atmospheric pressure	$[Pa]$
p_{in}	Static pressure at the inlet boundary	$[Pa]$
p_{ref}	Reference static pressure	$[Pa]$
q_{ref}	Reference dynamic pressure	$[Pa]$
Re	Reynolds number	$[-]$
S	Reference surface	$[m; m^2]$
St, S	Strouhal number	$[-]$
T_e, T	Period of oscillation of the cylinder	$[s]$
Ti	Incoming turbulence level	$[-]$
u	Component of the wake velocity in x direction	$[m/s]$
U_∞, U	Airspeed / Free-stream velocity	$[m/s]$
U_{ref}	Reference airspeed	$[m/s]$
v	Component of the wake velocity in y direction	$[m/s]$
v_{out}	Spatial average of the steady velocity at the outlet boundary	$[m/s]$
w	Component of the wake velocity in z direction	$[m/s]$
W_{cycle}	Work done by the fluid forces on the cylinder in one cycle of its motion	$[J]$
$y(t)$	Time signal of the motion of the cylinder	$[m]$
x	Coordinate in stream-wise direction	$[m]$
y	Coordinate perpendicular to span and stream defined positive as right hand law	$[m]$
z	Coordinate in span-wise direction	$[m]$

List of Figures

1	Sketches of streamlined, bluff bodies & the behaviour of the flow around them. The upper shows an attached flow until the trailing edge. Around the lower, instead, the flow presents separation, vortex formation and possible re attachments	2
2	Sketches presented by several authors in order to visualize the formation of the vortex shedding from circular cylinders. Gerrard [4] (left) illustrated it by means of line patterns. a - fluid within the growing vortex; b - fluid developing a shear layer ; c - fluid entering the region between the rare of the body and the growing vortex. Thomas Andrianne [67] (right)	3
3	Relationship between Strouhal number (St) and Reynolds number (Re) for circular cylinders. Data from Lienhard [5] and Achenbach & Heineke [71]. $St \sim 0.21$ ($1-21/Re$) for $40 < Re < 200$, from Roshko [1]	4
4	Possible wake patterns depending on the Reynolds number of the fluid around a circular cylinder (Re). Extracted from Lienhard in 1966 [5]	5
5	Oscillatory aerodynamic forces over fixed circular cylinders	6
6	C_D vs Re Curve. Results from several authors collected and compared by Nian-Sheng Cheng [57]	7
7	c_p [-] distribution over a circular cylinder. Distribution obtained from the potential flow theory (red). Experimental data at $Re \sim 100000$ and $Re \sim 200000$ (grey lines) [67]	7
8	Maximum amplitude as a function of airspeed for several values of structural damping (ζ). Experimental data extracted from the Wind-Tunnel at Université de Liège. The aeroelastic system is constructed by a rigid circular cylinder supported by 4 lineal springs which can vibrate freely in cross direction to the fluid flow. The structural damping is modified by attaching different elastomers to the vibratory structure [66]	10
9	Oscillation characteristics for a freely vibrating circular cylinder with light damping ($2M\delta_s/\rho D^2 = 0.4$). N , body oscillating frequency ; n , vortex shedding frequency. \bar{Y}/D , normalized maximum amplitude of oscillation measured at a particular value of reduced velocity (U/ND) ; ϕ^o , phase angle between the fluid force and the cylinder displacement. \circ vortex-shedding frequency; $+$ cylinder frequency; \square phase angle ; x oscillation amplitude [47] [18]	11
10	Variation of the phase difference of the lift force with respect to the motion of the cylinder for increasing values of the wavelength ratio ($\lambda/D = U_\infty/f_{osc}D$) for an elastically-mounted cylinder. Extracted from Feng [6]	12
11	Representation of the lock-in region by several authors. (a) lock-in region for imposed motion cylinders on the plane "imposed amplitude-imposed frequency" extracted from [67]. (b) synchronization region on the plane "amplitude-wavelength" being the region marked with a "B" extracted from [21]. Definition of the wavelength: $\lambda = U_\infty T_{osc} = U_\infty / f_{osc}$	13

12	Data recompilation from several authors of the field: ϕ_{lift} and C_L as a function of $f_e/f_o = f_{osc}/f_{vs}^o$ and $f_e/f_t = f_{osc}/f_{vs}$ for $ y /D = 0.5$. $ y $, amplitude of the imposed motion of the cylinder; $f_o = f_{vs}^o$ vortex shedding frequency from a stationary cylinder; $f_e = f_{osc}$, imposed frequency motion of the cylinder; $f_t = f_{vs}$, vortex shedding frequency from a oscillating cylinder (<i>"it is expected to deviate slightly from $f_o = f_{vs}^o$"</i> [45]). "Current" refers to data obtained and presented by J. Carberry, J. Sheridan & D. Rockwell [45]. Extracted from [45]	14
13	Map of vortex synchronization patterns near the fundamental lock-in region from [21]. I and II are the curves where the forces on the body show a sharp "jump" from Bishop and Hassan [3]	15
14	Sketches of the vortex shedding patterns that were found by Williamson and Roshko in [21]. "P", a vortex pair ; "S", single vortex. Each pattern is defined by the number of pairs and single vortices formed per cycle. Dashed line encircles the vortices shed in one complete cycle. Extracted from [21]	16
15	Drawing of the Wind Tunnel Facility at ULiège [72]	18
16	VIV Test Rig [72]	19
17	Sketches of the measurement and reference systems set-up	20
18	Graphical representation of the Half Power Method extracted from [65]. Figure is presented in order to define the damping ratio, ζ_n . Numerical data presented is independent of the current project	21
19	FFT of the time displacement of the cylinder at wind-off test	22
20	Evolution of the non dimensional standar deviaton of the amplitude (left) and maximum amplitude (right) of the motion of the cylinder for increasing values of windspeed	23
21	f_{vs} , \circ , & f_{vs} , Δ , as a function of the windspeed from experimental data	23
22	Time mean distribution of the pressure coefficient (\bar{c}_p) over the mid-span section of the static cylinder at $Re \sim 1 \cdot 10^4$. Plotted over the geometry of the circular section	24
23	Time mean loading of the cylinder at $Re \sim 1 \cdot 10^4$. \bar{c}_p as a function of the angle φ (left). Where, φ is the angle defined in Figure 17a positive in the increasing direction of the numbering of the pressure taps. \bar{c}_p as a function of the streamwise coordinate x (right). This coordinate starts at the center of the circular section and it is positive downstream (see Figure 17a).	25
24	2D lift and drag (left) coefficients at mid-span section of the cylinder obtained from the experimental data at $U_\infty = 1.4839$ [m/s] ($Re \sim 1 \cdot 10^4$). Time distribution (left) ; FFT analysis of $c_{L_{exp}}$ (right)	26
25	Time distribution of the wake velocity recorded by the Cobra Probe at $U_\infty = 1.4839$ [m/s] ($Re \sim 1 \cdot 10^4$). Streamwise component (u), spanwise component(w), orthogonal component to the others (v). See Figure 17b	26
26	FFT of the Wake Velocity at $U_\infty = 1.4839$ [m/s] ($Re \sim 1 \cdot 10^4$)	27
27	Time mean distribution of the pressure coefficient (\bar{c}_p) over the mid-span section of the moving cylinder at $U_\infty = 4.2786$ [m/s] ($Re \sim 2.9 \cdot 10^4$). Plotted over the geometry of the circular section	28

28	Time mean loading of the cylinder at $U_\infty = 4.2786$ [m/s] ($Re \sim 2.9 \cdot 10^4$). \bar{c}_p as a function of the angle φ (left). Where, φ is the angle defined in Figure 17a positive in the increasing direction of the numbering of the pressure taps. \bar{c}_p as a function of the streamwise coordinate x (right)	29
29	2D lift (left) and drag (right) coefficients at mid-span section of the cylinder obtained from the experimental data at $U_\infty = 4.2786$ [m/s] ($Re \sim 2.9 \cdot 10^4$) . . .	29
30	Time distribution of the wake velocity recorded by the Cobra Probe at $U_\infty = 4.2786$ [m/s] ($Re \sim 2.9 \cdot 10^4$). Streamwise component (u), spanwise component(w), orthogonal component to the others (v). See Figure 17b	30
31	FFT of the experimental time signals of the lift coefficient (right) and wake velocity (left) at $U_\infty = 4.2786$ [m/s] ($Re \sim 2.9 \cdot 10^4$)	31
32	Geometry of the two dimensional fluid domain used in ANSYS Fluent	33
33	Evolution of c_D (left) and spatial average of c_p on the cylinder (right) for increasing values of number of cells on the grid. RANS Transition SST (red) and RANS $k-\omega$ SST (black) turbulent models have been analyzed at $Re \sim 1 \cdot 10^4$	34
34	Evolution of c_L (left) and u_{out} (right) for increasing values of number of cells on the grid. RANS Transition SST (red) and RANS $k-\omega$ SST (black) turbulent models at $Re \sim 1 \cdot 10^4$	34
35	Validated bidimensional unstructured grid	36
36	2D circular domain and structured grid used in the turbulence model selection process (subsection 4.9)	37
37	Time evolution of $c_{D_{mo}}$ and $c_{L_{mo}}$ until convergence has been reached. These results correspond to URANS $k-\omega$ SST and RSM $k-\varepsilon$ turbulence models used in subsection 4.9	38
38	Time mean distribution of the pressure coefficient over the static cylinder at $U_\infty = 1.4839$ [m/s] ($Re \sim 1 \cdot 10^4$). Comparison between experimental and numerical data. X, URANS models; Δ , SAS models; \bigcirc , Experimental data	42
39	$C_L(t)$ & $C_D(t)$ Time distribution of the 3D static cylinder at $U_\infty = 1.4839$ [m/s] ($Re \sim 1 \cdot 10^4$). URANS Transition SST Turbulence model (left). URANS $k-\omega$ SST turbulence model (right)	47
40	$C_L(t)$ & $C_D(t)$ Time distribution of the 3D static cylinder at $U_\infty = 1.4839$ [m/s] ($Re \sim 1 \cdot 10^4$). SAS Transition SST Turbulence model (left). SAS $k-\omega$ SST turbulence model (right)	47
41	Comparison of \bar{c}_p distribution over the mid-span section of the static cylinder at $U_\infty = 1.4839$ [m/s] ($Re \sim 1 \cdot 10^4$) extracted from 3D simulations. Experimental data is also included	49
42	Time step size convergence study. Evolution of aerodynamic coefficients (\bar{c}_L & \bar{c}_D) on the moving cylinder for decreasing values of the time step, Δt , at $Re \sim 2.9 \cdot 10^4$	55
43	Time step size convergence study. Evolution of the time mean values of velocity (\bar{u}_{out}) and flow rate (\bar{m}_{out}) in the outlet boundary for decreasing values of the time step, Δt , at $Re \sim 2.9 \cdot 10^4$	55
44	Spatial averaged \bar{c}_p over the oscillatory cylinder with $f_{osc} = 7.07$ [Hz] & $ y = 0.038$ [m] as a function of Δt size at $Re \sim 2.9 \cdot 10^4$	56
45	Wake Pattern convergence plotting μ_t/μ contours for the oscillating cylinder with $f_{osc} = 7.07$ [Hz] & $ y = 0.038$ [m] at $Re \sim 2.9 \cdot 10^4$ for $\Delta t = 0.005$ [s] & $\Delta t = 0.01$ [s]	56

46	Wake pattern convergence plotting μ_t/μ for the oscillating cylinder with $f_{osc} = 7.07$ [Hz] & $ y = 0.038$ [m] at $Re \sim 2.9 \cdot 10^4$ for $\Delta t = 0.001$ & $\Delta t = 0.0005$ [s]	56
47	Time distribution of the monitored lift and drag coefficients ($c_{L_{mo}}(t)$ & $c_{L_{mo}}(t)$) in ANSYS Fluent for the moving cylinder at imposed motion frequency of $f_{osc} = 7.07$ [Hz] and amplitude of $ y = 0.038$ [m] at $U_\infty = 4.2786$ [m/s] ($Re \sim 2.9 \cdot 10^4$). Results extracted from CFD codes using k- ω SST turbulence model in both URANS (left) and SAS (right) versions	59
48	Time distribution of the monitored lift and drag coefficients ($c_{L_{mo}}(t)$ & $c_{L_{mo}}(t)$) in ANSYS Fluent for the moving cylinder at imposed motion frequency of $f_{osc} = 7.07$ [Hz] and amplitude of $ y = 0.038$ [m] at $U_\infty = 4.2786$ [m/s] ($Re \sim 2.9 \cdot 10^4$). Results extracted from CFD codes using Transition SST turbulence model in both URANS (left) and SAS (right) versions	59
49	Spatial distribution of \bar{c}_p over the cylinder from URANS (black) and SAS (red) Transition SST (right) and URANS (black) and SAS (red) k- ω SST (left) turbulence models. Imposed motion of $f_{osc} = 7.07$ [Hz] & $ y = 0.038$ [m] and airspeed $U_\infty = 4.8627$ [m/s] ($Re \sim 2.9 \cdot 10^4$)	61
50	Spatial distribution of \bar{c}_p over the 2D oscillating cylinder. Imposed motion of $f_{osc} = 7.07$ [Hz] & $ y = 0.038$ [m] and airspeed $U_\infty = 4.8627$ [m/s] ($Re \sim 2.9 \cdot 10^4$). SAS Transition SST (red) ; SAS k- ω SST (black)	61
51	Classification of the analyzed cases in locked (red-cross) and unlocked (blue circle) conditions. Non-dimensional amplitude vs non-dimensional frequency of the imposed motion of the cylinder. $Re \sim 2.9 \cdot 10^4$	66
52	FFT of $c_L(t)$ for the different cases performed with $ y /D = 0.38$ at $U_\infty = 4.8627$ [m/s] ($Re \sim 2.9 \cdot 10^4$)	67
53	Evolution of the amplitude related to the main frequency of the lift coefficient (left) and phase with respect to the imposed motion of the cylinder (right) as a function of the imposed frequency. Motion with constant amplitude $ y /D = 0.38$ at $Re \sim 2.9 \cdot 10^4$	69
54	Time mean pressure coefficient distribution over the cylinder with constant $ y /D = 0.38$ amplitude and different imposed frequencies at $Re \sim 2.9 \cdot 10^4$. Unlocked cases (left). Cases close to the 'unlocked-locked' transition (right)	70
55	Time mean pressure coefficient distribution over the cylinder with constant $ y /D = 0.38$ amplitude and different imposed frequencies at $Re \sim 2.9 \cdot 10^4$. Comparison between one of the cases of each characteristic groups (right). Locked case (blue), unlocked (yellow), transitional region (orange)	71
56	Time mean value of friction coefficient (\bar{c}_f) over the cylinder with constant $ y /D = 0.38$ amplitude and 3 different imposed frequencies at $Re \sim 2.9 \cdot 10^4$. Unlocked: $f_{osc}/f_{vs}^o = 0.422$ (blue). Transition: $f_{osc}/f_{vs}^o = 0.756$ (orange). Locked: $f_{osc}/f_{vs}^o = 1$ (yellow)	71
57	Spatial average of \bar{c}_p over the cylinder walls as a function of the non-dimensional frequency of the imposed motion with $ y /D = 0.38$ at $Re \sim 2.9 \cdot 10^4$	72
58	Vorticity (Equation 8) patterns in the wake behind the oscillatory cylinder with $ y /D = 0.38$ of 3 locked cases $Re \sim 2.9 \cdot 10^4$. Red color refers to positive vorticity and blue to negative. It is shown a clear 2S vortex shedding mode. [73]	73

59	Vorticity (Equation 8) patterns in the wake behind the oscillatory cylinder with $ y /D = 0.38$ at $Re \sim 2.9 \cdot 10^4$. Red color refers to positive vorticity and blue to negative	74
60	Evolution of the non-dimensional energy coefficient (c_E) as a function of the frequency of the imposed sinusoidal motion on the cylinder, f_{osc} , with a constant amplitude of $ y /D = 0.38$ at $Re \sim 2.9 \cdot 10^4$	75
61	FFT of $c_L(t)$ for 3 different imposed motion amplitudes: $ y /D = 0.05, 0.2, 0.38$ at 3 imposed frequencies $f_{osc}/f_{vs}^o = 0.677$, $f_{osc}/f_{vs}^o = 0.816$ & $f_{osc}/f_{vs}^o = 1$ at $Re \sim 2.9 \cdot 10^4$	76
62	Fast Fourier Transform of the lift coefficient time signal at 3 different imposed motion amplitudes: $ y /D = 0.05, 0.2, 0.38$ at $Re \sim 2.9 \cdot 10^4$. Frequency of the imposed motion $f_{osc}/f_{vs}^o = 0.677$ (left) ; $f_{osc}/f_{vs}^o = 0.816$ (right)	77
63	Fast Fourier Transform of the lift coefficient time signal with 3 different imposed motion amplitudes: $ y /D = 0.05, 0.2, 0.38$ and $f_{osc}/f_{vs}^o = 1$ imposed frequency at $Re \sim 2.9 \cdot 10^4$	77
64	Evolution of $ c_L $ (left) and ϕ_L (right) as a function of the non-dimensional amplitude of the imposed motion at constant imposed frequencies of $f_{osc}/f_{vs}^o = 0.677, 0.816, 1$ at $Re \sim 2.9 \cdot 10^4$	78
65	Time mean pressure coefficient distribution (right) and time friction coefficient (\bar{c}_f) distribution (left) over the cylinder with constant $f_{osc}/f_{vs}^o = 0.677$ frequency and different imposed amplitudes at $Re \sim 2.9 \cdot 10^4$ for locked and unlocked cases	79
66	Time mean pressure coefficient distribution (right) and time mean friction coefficient (\bar{c}_f) distribution (left) over the cylinder with constant $f_{osc}/f_{vs}^o = 0.816$ frequency and different imposed amplitudes at $Re \sim 2.9 \cdot 10^4$ for locked and unlocked cases	80
67	Time mean pressure coefficient distribution (right) and time mean friction coefficient (\bar{c}_f) distribution (left) over the cylinder with constant $f_{osc}/f_{vs}^o = 1$ frequency and different imposed amplitudes at $Re \sim 2.9 \cdot 10^4$ for locked and unlocked cases	80
68	Vorticity (Equation 8) patterns in the wake behind the oscillatory cylinder at $f_{osc}/f_{vs}^o = 0.677$ for three different motion amplitudes: (a) $ y /D = 0.05$; (b) $ y /D = 0.2$; (c) $ y /D = 0.38$. Red color refers to positive vorticity and blue to negative	81
69	Vorticity (Equation 8) patterns in the wake behind the oscillatory cylinder at $f_{osc}/f_{vs}^o = 0.816$ for three different motion amplitudes: (a) $ y /D = 0.05$; (b) $ y /D = 0.2$; (c) $ y /D = 0.38$. Red color refers to positive vorticity and blue to negative	81
70	Vorticity (Equation 8) patterns in the wake behind the oscillatory cylinder at $f_{osc}/f_{vs}^o = 1$ for three different motion amplitudes: (a) $ y /D = 0.05$; (b) $ y /D = 0.2$; (c) $ y /D = 0.38$. Red color refers to positive vorticity and blue to negative	81
71	Definition of θ angular coordinate	83
72	Unsteady components of $c_p(t)$ over the oscillating cylinder with locked vortex shedding at $Re \sim 2.9 \cdot 10^4$. Magnitudes related to 2 frequencies are presented: f_{osc} (blue) & $2 \cdot f_{osc}$ (red). Imposed motions: $f_{osc}/f_{vs}^o = 1$ & $ y /D = 0.38$ (left) ; $f_{osc}/f_{vs}^o = 1$ & $ y /D = 0.2$ (right)	84

73	Unsteady components of $c_p(t)$ over the oscillating cylinder with locked vortex shedding at $Re \sim 2.9 \cdot 10^4$. Magnitudes related to 2 frequencies are presented: f_{osc} (blue) & $2 \cdot f_{osc}$ (red). Imposed motions: $f_{osc}/f_{vs}^o = 0.816$ & $ y /D = 0.38$ (left) ; $f_{osc}/f_{vs}^o = 1.14$ & $ y /D = 0.38$ (right)	85
74	FFT of $c_p(t)$ at $\theta = 50$ [°] for $f_{osc}/f_{vs}^o = 1$ & $ y /D = 0.38$ (left) and $f_{osc}/f_{vs}^o = 0.816$ & $ y /D = 0.38$ (right) imposed motions at $Re \sim 2.9 \cdot 10^4$	86
75	Unsteady components of $c_p(t)$ over the oscillating cylinder with locked vortex shedding at $Re \sim 2.9 \cdot 10^4$. Imposed motion: $f_{osc}/f_{vs}^o = 0.816$ & $ y /D = 0.2$	86
76	Unsteady components of $c_p(t)$ over the oscillating cylinder with unlocked vortex shedding at $Re \sim 2.9 \cdot 10^4$. Imposed motions: $f_{osc}/f_{vs}^o = 0.677$ & $ y /D = 0.2$ (left) ; $f_{osc}/f_{vs}^o = 0.677$ & $ y /D = 0.38$ (right)	87
77	FFT of $c_p(t)$ at $\theta = 0$ [°] for $f_{osc}/f_{vs}^o = 0.677$ & $ y /D = 0.38$ (left) and $f_{osc}/f_{vs}^o = 0.677$ & $ y /D = 0.05$ (right) imposed motions at $Re \sim 2.9 \cdot 10^4$	88
78	Unsteady components of $c_p(t)$ over the oscillating cylinder with unlocked vortex shedding at $Re \sim 2.9 \cdot 10^4$. Imposed motions: $f_{osc}/f_{vs}^o = 0.68$ & $ y /D = 0.05$ (left) ; $f_{osc}/f_{vs}^o = 0.81$ & $ y /D = 0.05$ (right)	89
79	Unsteady components of $c_p(t)$ over the oscillating cylinder with locked vortex shedding at $Re \sim 2.9 \cdot 10^4$. Imposed motion: $f_{osc}/f_{vs}^o = 1$ & $ y /D = 0.05$	89
80	Lock-in region for the cylinder oscillation transverse to the incoming flow at $Re \sim 2.9 \cdot 10^4$. Results from 2D domain (left): \circ , unlocked; $+$, locked. Results from 3D domain at mid-span section (right): \circ , locked; \square , unlocked [68]	91
81	FFT of the lift coefficient for unlocked cases at $Re \sim 2.9 \cdot 10^4$. Results from 2D domain (left): $f_{osc}/f_{vs}^o = 0.4$ & $f_{osc}/f_{vs}^o = 0.38$. Results from 3D domain at mid-span section (right): $ y /D = 0.5$ & $f_{osc}/f_{vs}^o = 0.5$ [68]	92
82	Evolution of the amplitude related to the main frequency of lift coefficient as a function of the imposed frequency (left) and of imposed amplitude (right). Results of 2D cylinder at $Re \sim 2.9 \cdot 10^4$	93
83	Amplitude of the main frequency of $C_p(t)$ over the mid-span section of the 3D cylinder at $Re \sim 2.9 \cdot 10^4$. Comparison of the effect of the imposed amplitude at $f_{osc}/f_{vs}^o = 0.83$ (left). Comparison of the effect of the imposed frequency at $ y /D = 0.38$ (right) [68]	95
84	Amplitude of the main frequency of $c_p(t)$ over the 2D cylinder at $Re \sim 2.9 \cdot 10^4$. Comparison of the effect of the imposed amplitude at $f_{osc}/f_{vs}^o = 1$ (left). Comparison of the effect of the imposed frequency at $ y /D = 0.38$ (right)	95
85	Amplitudes of the predominant frequencies of $C_p(t)$ over the mid-span section of the 3D cylinder at $Re \sim 2.9 \cdot 10^4$. Two unlocked cases are presented: $f_{osc}/f_{vs}^o = 0.5$ & $ y /D = 0.38$ (left); $f_{osc}/f_{vs}^o = 0.5$ & $ y /D = 0.5$ (right) [68]	96
86	Unsteady components of $c_p(t)$ over the 2D oscillating cylinder with unlocked vortex shedding. Imposed motions: $f_{osc}/f_{vs}^o = 0.677$ & $ y /D = 0.2$ (left) ; $f_{osc}/f_{vs}^o = 0.677$ & $ y /D = 0.38$ (right)	96
87	Basic Scheme of SIMPLE Algorithm [70]	106
88	Basic Scheme of PISO Algorithm [69]	107

List of Tables

1	Natural frequency (f_n) and damping ratio (ζ_n) of the structural mode identified in the experimental setting of the circular cylinder at wind-off ($U_\infty = 0$)	22
2	Time mean values of lift and drag coefficients computed from the experimental pressure distribution over the mid-span section at $U_\infty = 1.4839$ [m/s] ($Re \sim 1 \cdot 10^4$). Main frequency of the time distribution of experimental lift coefficient	25
3	Time mean value of each wake velocity component and oscillation frequency of the lift coefficient at $U_\infty = 1.4839$ [m/s] ($Re \sim 1 \cdot 10^4$)	27
4	Shedding frequency and Strouhal number obtained from (a) time distribution of the experimental c_L and (b) time distribution of the fluid velocity in the vortex at $U_\infty = 1.4839$ [m/s] ($Re \sim 1 \cdot 10^4$)	27
5	Time mean values of lift and drag coefficients computed from the experimental pressure distribution over the moving cylinder at mid-span section at $U_\infty = 4.2786$ [m/s] ($Re \sim 2.9 \cdot 10^4$). Main frequency of the time distribution of experimental lift coefficient	30
6	Time mean value of each wake velocity component and oscillation frequency of the lift coefficient at $U_\infty = 4.2786$ [m/s] ($Re \sim 2.9 \cdot 10^4$).	30
7	Steady parameters used in the mesh independence study of 2D static numerical code with RANS $k - \omega$ SST turbulence model at $Re \sim 1 \cdot 10^4$	35
8	Steady parameters used in the mesh independence study of 2D static numerical code with Transition SST Turbulence model at RANS $Re \sim 1 \cdot 10^4$	35
9	Time dependent parameters used in the mesh independence study of 2D static numerical code with SAS $k - \omega$ SST turbulence model at $Re \sim 1 \cdot 10^4$. \bar{c}_L , time mean value of 2D lift coefficient; \bar{c}_D , time mean value of 2D drag coefficient; Ave. \bar{c}_p , spatial average of the time mean pressure coefficient over the cylinder; \bar{u}_{out} , area average of the time mean value of velocity at outlet boundary; \bar{m}_{out} , time mean value of the mass flow rate at outlet boundary	35
10	Time dependent parameters used in the mesh independence study of 2D static numerical code with Transition SAS SST turbulence model at $Re \sim 1 \cdot 10^4$. \bar{c}_L , time mean value of 2D lift coefficient; \bar{c}_D , time mean value of 2D drag coefficient; Ave. \bar{c}_p , spatial average of the time mean pressure coefficient over the cylinder; \bar{u}_{out} , area average of the time mean value of velocity at outlet boundary; \bar{m}_{out} , time mean value of the mass flow rate at outlet boundary	36
11	Time step size Δt convergence analysis for the 2D static cylinder CFD code at $Re \sim 1 \cdot 10^4$	40
12	Strouhal number (St) and shedding frequency (f_{vs}) obtained from 2D unstructured mesh simulations at $Re \sim 1 \cdot 10^4$	41
13	Strouhal number (St) and shedding frequency (f_{vs}) obtained from 2D structured mesh simulations at $Re \sim 1 \cdot 10^4$	42
14	Number of nodes and elements of the 3 different three dimensional meshes analyzed in the convergence study at $Re \sim 1 \cdot 10^4$	45
15	Steady and time dependent parameters used in the mesh independence study of 3D static numerical code with SAS $k - \omega$ SST turbulence model at $Re \sim 1 \cdot 10^4$	45
16	Comparison of the 3D time mean lift and drag coefficients monitored in ANSYS Fluent at $Re \sim 1 \cdot 10^4$	48

17	Vortex shedding frequency (f_{vs}) and Strouhal (St) values extracted from the time evolution of $C_{L_{mo}}$ and $C_{D_{mo}}$ of the numerical 3D simulation at $Re \sim 1 \cdot 10^4$. . .	49
18	Time step convergence analysis for the CFD code of the oscillating cylinder based on the SAS Transition SST turbulence model at $Re \sim 2.9 \cdot 10^4$	54
19	Time step convergence analysis for the CFD code of the oscillating cylinder based on the SAS $k - \omega$ SST turbulence model at $Re \sim 2.9 \cdot 10^4$	54
20	Number of iterations per time step analysis for the CFD code of the moving cylinder under imposed motion of $f_{osc} = 7.07$ [Hz] & $ y = 0.038$ [m] based on the SAS Transition SST turbulence model at $Re \sim 2.9 \cdot 10^4$	57
21	Time mean values of lift and drag coefficients obtained from each turbulence model for the moving cylinder under an imposed motion of $f_{osc} = 7.07$ [Hz] & $ y = 0.038$ [m] at $U_\infty = 4.8627$ [m/s] ($Re \sim 2.9 \cdot 10^4$)	60
22	Vortex Shedding frequency obtained from each turbulence model for the moving cylinder under an imposed motion of $f_{osc} = 7.07$ [Hz] & $ y = 0.038$ [m] at $U_\infty = 4.8627$ [m/s] ($Re \sim 2.9 \cdot 10^4$)	60
23	Properties of the prescribed motion of the analyzed cases	65
24	Predominant frequencies extracted from the FFT of $c_L(t)$ resultant from numerical simulation under imposed motion of $ y /D = 0.38$ amplitude and variable frequency (f_{osc}/f_{vs}^o) at $Re \sim 2.9 \cdot 10^4$. f_{vs1} , frequency of biggest magnitude; f_{vs2} , frequency of second biggest magnitude.	68
25	Amplitude of the main frequency of $C_L(t)$ for different locked motions at $Re \sim 2.9 \cdot 10^4$. Results at mid-span section of the moving 3D cylinder [68]	93
26	Amplitude of the main frequency of $C_L(t)$ for different unlocked motions at $Re \sim 2.9 \cdot 10^4$. Results at mid-span section of the moving 3D cylinder [68]	93
27	Phase difference between main component of $C_L(t)$ and $y(t)$ for different imposed motion at $Re \sim 2.9 \cdot 10^4$. Results at mid-span section of the moving 3D cylinder [68]	94

1 Introduction

In aerodynamics, science which studies the motion of the air and particularly when it interacts with one or more solid objects, the bodies within the flow can be divided in two big groups: aerodynamic bodies and bluff bodies.

On the one hand, the former are basically airfoils or streamlined bodies. The flow around these objects, when working under favourable conditions, follows the contours of the body being attached to it until the trailing edge. It also presents a narrow afterbody wake. However, under unfavorable working conditions (e. g. big angles of attacks), at some point the flow can separate from the body introducing a big amount of turbulence, vorticity and unsteadiness in the flow after separation occurs. This situation will develop time dependent fluid forces over the airfoils which are way more complex than the steady loading produced by attached flows.

On the other hand, bluff bodies, due to their geometrical shape, the separation of the flow over them is inherent. Examples of this category are circular, rectangular and square cylinders, spheres or cones. The vortices arise rolling up the shear layers at sharp corners resulting in wide afterbody wakes. The flow in this region is highly unsteady and consequently the aerodynamic forces over the objects. Moreover, the produced drag is greater than in airfoils under favourable conditions because of the increase in the pressure drag introduced by the flow separation and consequent wake. Due to the inherent instability of the periodic vortex shedding process, oscillatory fluid forces will arise over the circular cylinders. As a response to such excitation, freely supported cylinders can trigger a self-excited oscillatory motion. This aeroelastic behaviour is called Vortex Induced Vibration. However, an imposed sinusoidal motion at a specific frequency and amplitude can excite the natural behaviour of the wake and modify it completely. Consequently, the unsteady loading over the circular cylinder will be modified too.

The unsteady behaviour of the airflow over circular cylinders under forced motion will be the case studied of the present report. The effect of the frequency and amplitude of the imposed motion have on the wake, lift and drag forces and unsteady pressure distribution will be analyzed.

First, a detailed background on the flow around circular cylinders will be presented in section 2. A review of the different researches made in history about the topic will be discussed. Taking the steady aerodynamics over static cylinders as a starting point, the reader will go through, both experimental and numerical works in unsteady aerodynamics. Then, when the basic understanding of the flow around this kind of bluff bodies will be settled, the aeroelastic phenomenon called Vortex Induced Vibration will be presented and discussed. Eventually, several experimental projects on cylinders under forced motion will be scrutinised in order to extract the key concepts needed for a good understanding of the present project.

section 3 presents experimental results extracted from the Wind Tunnel at Université de Liège. This data corresponds to an experiment on a circular cylinder undergoing vortex induced vibration. The unsteady pressure loading at mid-span of the cylinder is available, as well as, the time distribution of the displacement of the structure and the velocity components of the air in the wake.

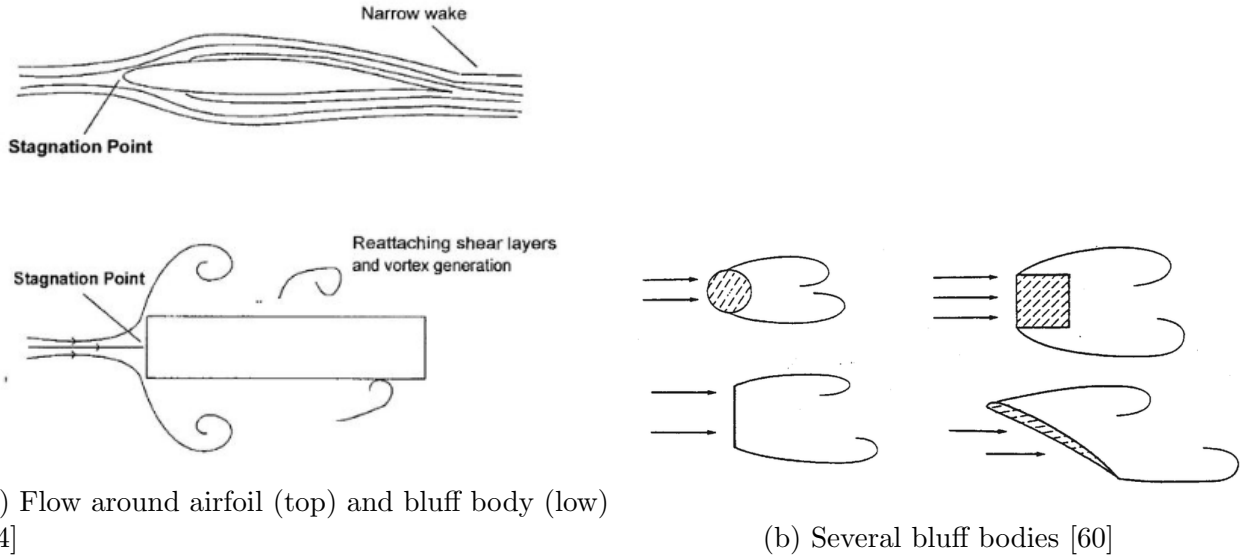


Figure 1: Sketches of streamlined, bluff bodies & the behaviour of the flow around them. The upper shows an attached flow until the trailing edge. Around the lower, instead, the flow presents separation, vortex formation and possible re attachments

The third part of the project consists in building a CFD code with ANSYS Fluent commercial software capable to well-represent and capture the key unsteady aerodynamic parameters of the fluid flow over oscillating cylinders. The code will be built in a sequential manner as the objective is to develop the simplest and most efficient code able to satisfy the requirements. In other words, a balance between the computational cost and accuracy of the results is desired. These simulations will be validated against experimental data analyzed previously. section 4 and section 5 present consequently the validation of a 2D and 3D CFD code of the flow over a static cylinder. Finally, in section 6, a 2D code of the flow around an oscillating cylinder is validated. This CFD code will be the one used for further analysis.

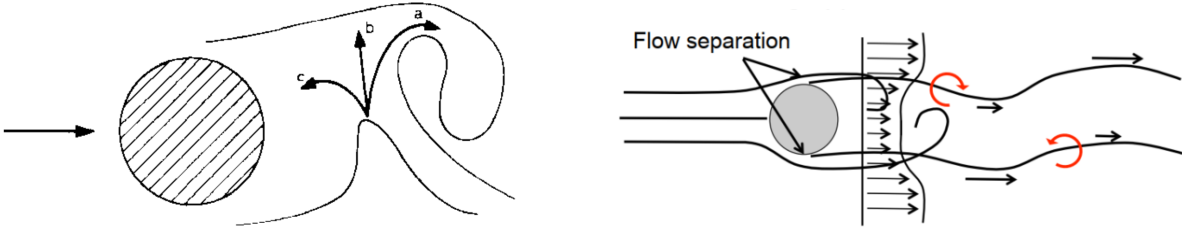
section 7 & section 8 present an extensive discussion of the evolution of several parameters of the fluid flow as a function of the imposed motion on the cylinder. Mainly, the frequency content and pattern of the wake; time varying signal of the lift coefficient; energy transmission between fluid and cylinder; and the mean and time distribution of the unsteady pressure over the circular cylinder will be analyzed. Special attention will be paid to the unlocked-locked transition boundary, as well as, the distinction of two well defined modes within the lock-in region.

section 9 includes a comparison between the results extracted from the two-dimensional analysis carried out in the present report and the three-dimensional developed by Martina Lomele in her Master Thesis Project [68].

Eventually, some conclusions and possible further work will be highlighted in section 10 to close the current report.

2 Unsteady Flow Over Circular Cylinders

The vortex shedding from a fixed circular cylinder is the main responsible of the unsteadiness of the flow and the time dependent aerodynamic loading over the cylinder. Many models have been released along history in order to well represent it. One of the first and most important models is the postulated by Gerrard in 1966 [4]. This author stated that the essential cause of the vortex-street wake is the reciprocal interaction between the two separating shear layers. He explained that a vortex keeps growing (gets the circulation to do so from the shear layer connected to it) until it is strong enough to draw the opposing shear layers in the near wake. Afterwards, when the oppositely signed vorticity approaches with sufficient intensity, it stops the supply of circulation from the shear layer and the vortex is shed. Figure 2a shows Gerrard's vortex formation process. The vortex shedding process is an inviscid mechanism based on shear layer instability. It is a global instability, the whole wake is affected, and robust, vorticity is continuously produced [67].



(a) Vortex-formation model presented by Gerrard [4]. Extracted from the work done by Bearman [17] (b) Sketch showing the rolling up of the shear layers and formation of the vortex shedding within the wake after a bluff body [67]

Figure 2: Sketches presented by several authors in order to visualize the formation of the vortex shedding from circular cylinders. Gerrard [4] (left) illustrated it by means of line patterns. a - fluid within the growing vortex; b - fluid developing a shear layer ; c - fluid entering the region between the rear of the body and the growing vortex. Thomas Andrianne [67] (right)

Furthermore, Abernathy & Kronauer [2], by means of a numerical research project, showed that the key mechanism for vortex shedding is the presence of two shear layers rather than the circular cylinder. The bluff body allows the feedback between the wake and the shedding of circulation at the separation points. Actually, the vorticity contained by shear layers is produced in the boundary layer (BL) due to the no-slip condition on the wall of the cylinder. When the flow separates, the vorticity makes the free-shear layer to roll up (Figure 2b).

Based on the previous works, several authors ([10] [14] [12]) developed different methods for calculating the vortex shedding process from bluff bodies and its rate. This phenomenon happens at a defined frequency called vortex shedding frequency (f_{vs}^o) which has a linear relation with the airspeed through the Strouhal number, St (Equation 1).

$$St = \frac{f_{vs}^o D}{U_\infty} \quad [-] \quad (1)$$

As stated by Bearman [17] and certified by experimental works, vortex shedding process is strongly affected by disturbances such as Reynolds number (Re), incoming turbulence level,

body-surface finish, aspect ratio, blockage ratio, acoustic noise or end-wall effects. Figure 3 presents the evolution of the St as a function of Re for smooth and rough cylinders. Also, two-dimensional bodies in uniform flow are unlikely to shed two dimensional vortices as oblique vortex shedding and the 3D effects of turbulent wakes are commonly present. A wide experimental research about these topics and how to avoid or deal with them can be found in literature. Some examples are [23] [53] [13] [71].

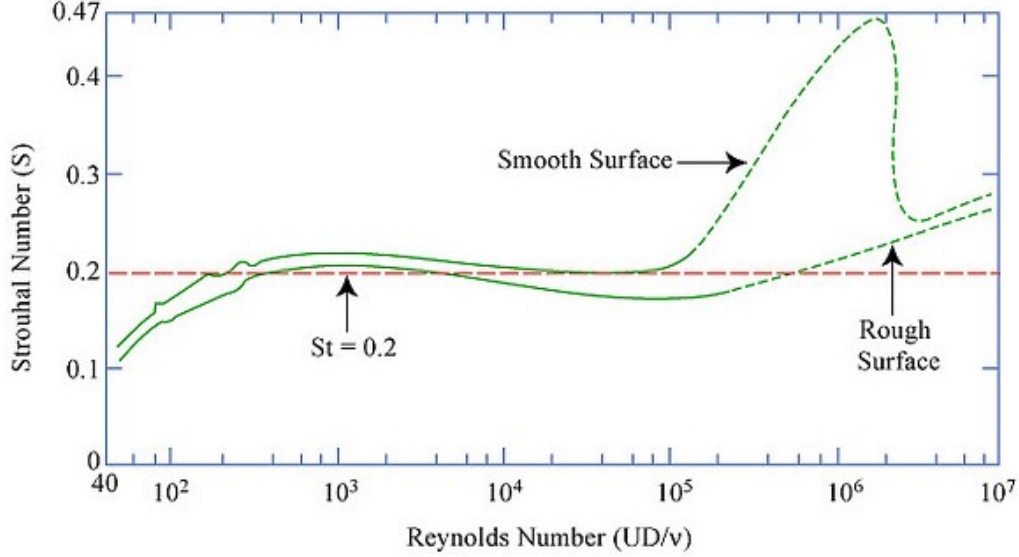


Figure 3: Relationship between Strouhal number (St) and Reynolds number (Re) for circular cylinders. Data from Lienhard [5] and Achenbach & Heineke [71]. $St \sim 0.21 (1-21/Re)$ for $40 < Re < 200$, from Roshko [1]

Figure 4 shows the different wake regimes that can arise from a fixed smooth circular cylinder as a function of the Reynolds number. 6 different wake patterns were identified by J. H. Lienhard in 1966 [5]:

- $Re < 5$: The fluid flow around the static cylinder keeps attached all the time. It is known as creeping flow. The vorticity created along the boundary layer is dissipated near the body [67].
- $5 < Re < 40$: A fixed pair of Föppl vortices take place in the wake. Each of it on opposite side of the symmetry line of the body.
- $40 < Re < 3 \cdot 150$: Von Karman Vortex Street. The shedding vortex process is fully laminar. Also the BL around the body.
- $150 < Re < 10^5$: Transition to turbulent regime happens in the wake. Hence, the flow in the boundary layer will present a laminar separation followed by a fully turbulent vortex street.
- $3 \cdot 10^5 < Re < 3.5 \cdot 10^6$: The BL undergoes transition to turbulent regime. As consequence, the wake is narrowed and disorganized.

- $3.5 \cdot 10^6 < Re$: The wake recovers the vortex shedding process. Both the BL and the vortices within the wake are fully turbulent.

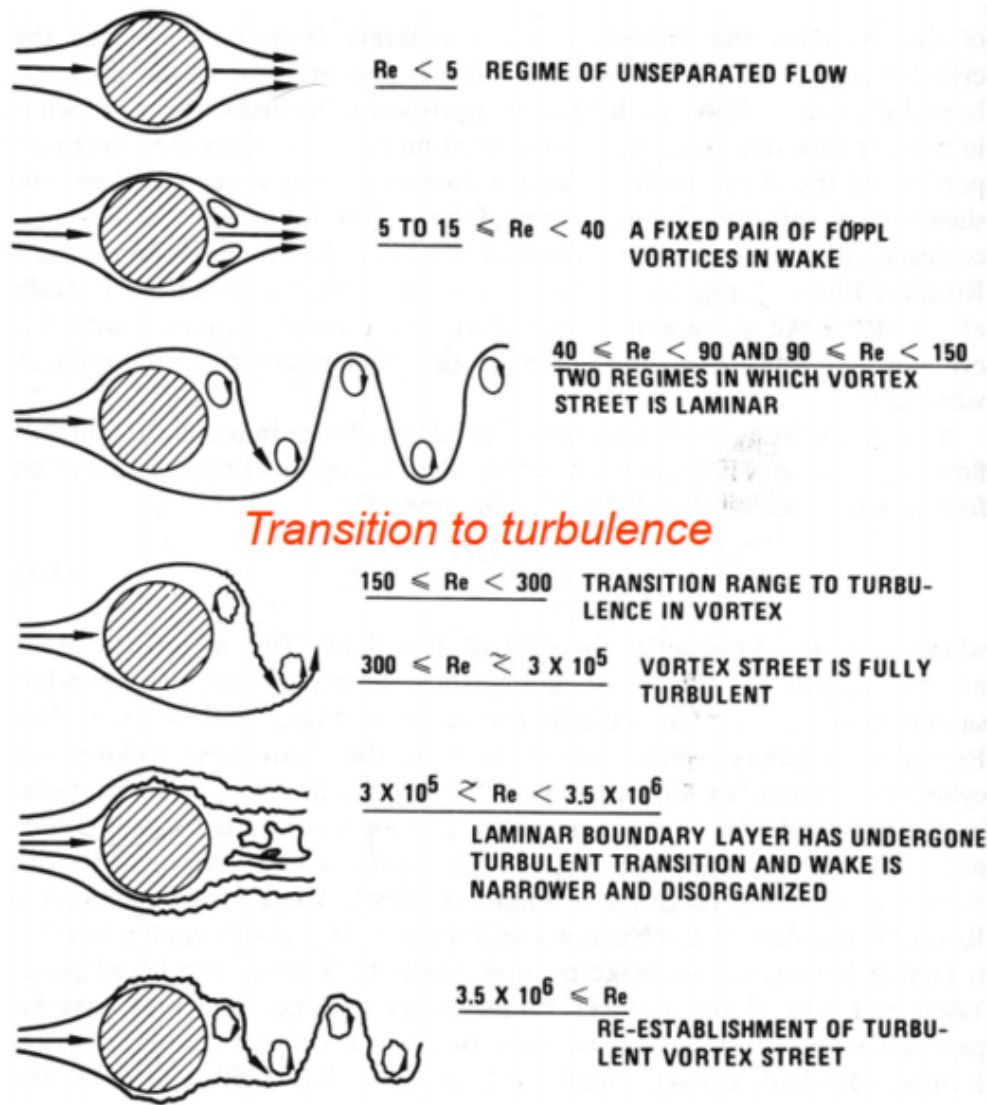


Figure 4: Possible wake patterns depending on the Reynolds number of the fluid around a circular cylinder (Re). Extracted from Lienhard in 1966 [5]

Regarding the aerodynamic loading over the cylinder, extensive experimental research has been developed along the years by several authors([44] [9] [22] [7]) under different working conditions. All of them concluded that there is a great impact of the shed vortices, and consequently of the Reynolds number or surface finish of the cylinder.

The lift ($L(t)$), force on the cylinder in the perpendicular direction to the fluid flow, is an image of the oscillatory vorticity in the wake of the cylinder [67]. The lift fluctuates ideally around $\bar{C}_L = 0$ mean value at a frequency equal to the vortex shedding and presents close to a pure sinusoidal time signal (Figure 5a). The drag ($D(t)$), force on the cylinder in the direction of

the fluid flow, shows rather a periodic time signal oscillating around a time mean value with a frequency equal to two times the shedding frequency. The shape of the drag force, as presented in Figure 5a, is further away from a sinusoidal signal compared to lift force time distribution. Furthermore, the amplitude of $D(t)$ is smaller compare to the amplitude of $L(t)$.

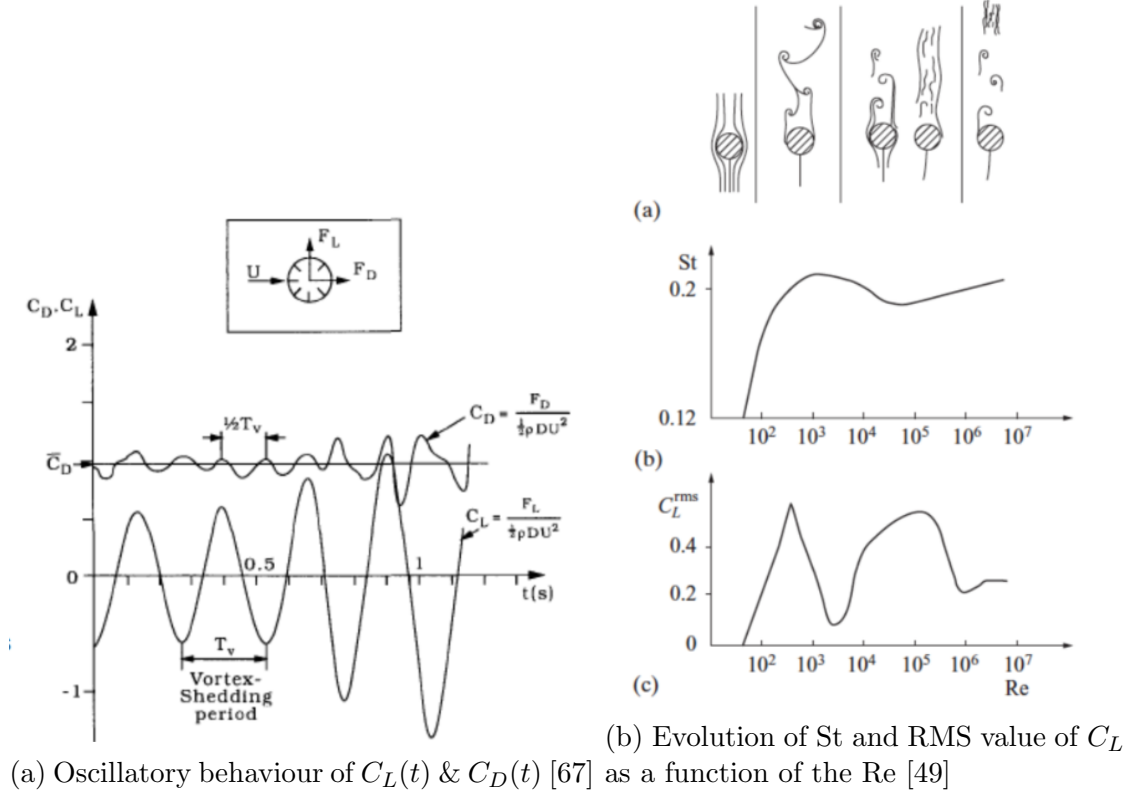


Figure 5: Oscillatory aerodynamic forces over fixed circular cylinders

Both forces are greatly affected by the Reynolds number. On the one hand, the well-known "drag crisis curve for circular cylinders" (Figure 6) shows the evolution of the mean value of C_D as a function of the Reynolds number. This curve was built for the very first time by Wieselsberger in 1922 and validated and rebuilt by several authors in history. Figure 6 collects experimental data acquired by several authors. On the other hand, as mentioned before, the lift force should oscillate around a null mean value. In practice, however, that does only happen at low Reynolds numbers. When moving to higher values of Re , due to the inherent disturbances of turbulent flows, the mean value will lay close to zero. Figure 5b presents the evolution of the RMS value of the lift coefficient as a function of the Reynolds number.

Eventually, Figure 7 compares the time mean pressure coefficient distribution over a circular cylinder at different Re values plotted over the c_p values from the potential flow theory. It can be deduced that the pressure distribution under attached flow conditions is nearly identical regardless the Reynolds number compared to the potential flow distribution. However, great differences are found after the flow separates from the body. Moving towards higher Reynolds numbers the separation of the BL happens further away from the front of the cylinder. Further-

more, more negative values are reached followed by a greater recovery of c_p to less negative values.

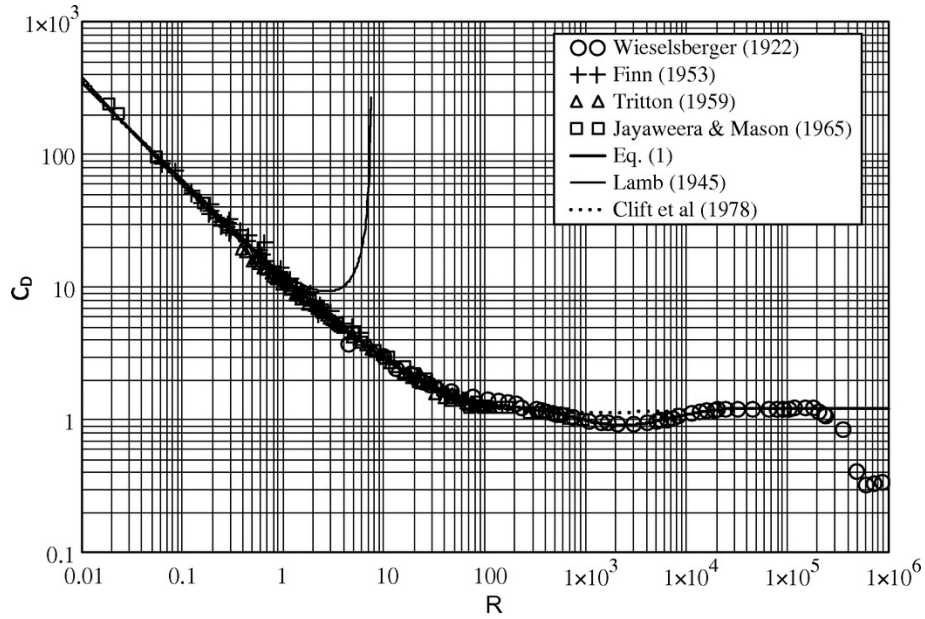


Figure 6: C_D vs Re Curve. Results from several authors collected and compared by Nian-Sheng Cheng [57]

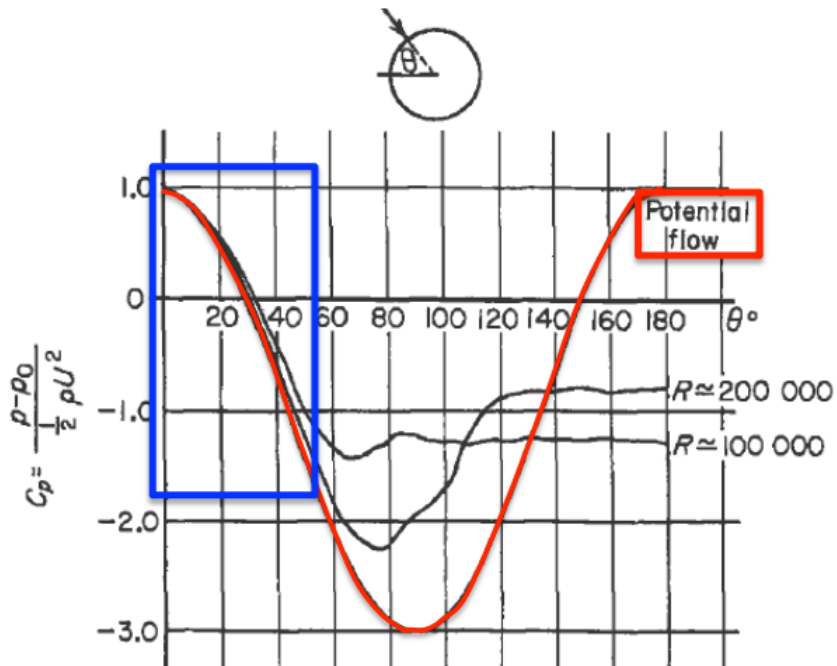


Figure 7: c_p [-] distribution over a circular cylinder. Distribution obtained from the potential flow theory (red). Experimental data at $Re \sim 100000$ and $Re \sim 200000$ (grey lines) [67]

2.1 Numerical Modelling of the Flow Around Static Cylinders

In the previous section a background on the flow over fixed cylinders was given. As described by A. I. Stamou & G. Papadonikolaki, "*The nature of this flow that combines a simple geometry with complicated flow phenomena, such as, flow separation, reattachment and vortex shedding is determined by the Reynolds number*" [59]. Actually, completely different flow regimes (Figure 4) will take place (and consequently will need to be modelled numerically) depending on Re , the surface roughness of the cylinder, free-stream velocity or flow turbulence level. This will set the approach taken by the authors in an attempt to model the physical phenomena over the bluff body.

Over the years, many authors developed their own CFD codes aiming to model flow around cylinders of different geometrical shapes such as square, quadrilateral or circular. Some of them went for structured meshes ([62] [38] [48] [63]), others instead, developed their own codes based on unstructured meshes ([55] [46] [61]). Furthermore, in the last years some adaptive mesh techniques have been applied based on vorticity ([55]). With the last meshing technique an automatic local refinement of the afterbody wake is desired in order to well-resolve the shedding vortex street. Even if the author states that the adaptive mesh technique reduces the total simulation time, he admits that this approach completely relies on the turbulence model chosen as the refinement of the mesh will be based on the solution given by it. Moreover, no enough strong arguments were found amongst the literature research regarding which of the meshing techniques (structured or unstructured) gives better results in terms of accuracy and efficiency.

The fundamental and most challenging aspect of the numerical simulation is the election of the turbulence model as the accuracy of the results will completely depend on its capabilities to solve and represent the physics of the problem. The Reynolds number in the test section will be $Re \sim 10^4$. As previously described, the boundary layer will be laminar followed by a separation and turbulent vortex street. Along the years, several authors built CFD codes in this fluid regime using different turbulence models and even comparing them (URANS-DES [38], URANS-LES [30] [48] [51], URANS-Hybrid [54] models, LES-DNS [46], LES-PIV [64]...).

Amongst other authors, X. Ma G.S. Karmanos & G.E Karniadakis [36] and S. Dong & G.E. Karniadakis [46] proved that Direct Numerical Simulation (DNS) well-resolves the flow over a cylinder at this range of Reynolds number and J. Franke & W. Frank [42], A. G. Kravchenko & P. Moin [35] and J. Fröhlich, W.Rodi, Ph. Kessler, S. Parpais, J.P. Bertoglio, D. Laurence [31] [40] did the same for Large Eddy Simulation (LES) turbulence model. However, these kind of modelling of the fluid flows require great CPU power and time and it is not feasible to run them during a reasonable period of time, needing high-performance computing and long flow-times to get stable results [73]. One of the main reasons for that is the extremely refined meshes of the computational domain. While DNS solves all size of eddies; LES, generally speaking, uses the size of the cell grid as a low-pass filter so that the eddies with a smaller size are modelled and the larger ones are resolved directly. "*The main shortcoming of LES lies in the high resolution requirements for wall boundary layers. Near the wall, even the 'large' eddies become relatively small and require a Reynolds number dependent resolution. This limits LES for wall bounded flows to very low Reynolds numbers ($Re \sim 10^4 - 10^5$) and limited to computational domains*" [73] as specified in ANSYS Fluent Manual [73].

Facing the previous turbulence modelling, Reynolds Averaged Navier-Stokes (RANS) or their unsteady version (URANS) require a computational cost which is orders of magnitudes lower. However, as they are statistic models which deal with averaged values, their resolution ability and accuracy is limited when *"large-scale eddy structures dominate the turbulent transport, when unsteady processes like vortex shedding and unstable behaviour prevail and dynamic loading is of importance"* [30]. In 2016 E. Palkin, R. Mullyadzhanov, M. Hadziabdic and K. Hanjalic published an extensive analysis of the capabilities and limitations of the RANS and URANS turbulence models [63] regarding separated flows and vortex shedding. They concluded that URANS models presented *"relatively poor performance"* [63] for flows at low Reynolds numbers but *"successful in reproducing dynamic features of the flow around cylinders in the subcritical regime with laminar separation"* [63].

Furthermore, it is suggested that *"for high-Reynolds complex flows of industrial relevance, one could relay on the URANS approach provided the RANS model employed is capable of resolving the stress anisotropy, as does a second-order closure"* [63]. These flows imply high computational cost, usually not affordable, if properly resolved by LES or DSN approaches.

Aiming to find a balance between the accuracy and efficiency of the turbulence models, hybrid models have been continuously being developed in the last years. Examples of these models are Detached Eddy Simulation, DES, (and its improved versions DDES, IDDES); or Scale Adaptive Simulation, SAS. These methods are specially of interest in practical problems where the high accuracy that LES or DNS could provide at high computational time and cost is not require, and efficiency with a lower accuracy is desired. However, when using these turbulence models the computational cost is greater than URANS.

On the one hand, *"DES models have been specially designed to address high Reynolds number wall bounded flows, where the cost of a near-wall resolving Large Eddy Simulation would be prohibited"* [73]. The model, also known as LES/RANS hybrid model for being the first developed industrial hybrid model, combines RANS in the boundary layer region around the body and LES in the separated regions where *"large unsteady turbulence scales play a dominant role"* [73]. Anrei Travin, Michael Shur, Michael Strelets & Philippe Spalart [38] developed a validation of DES turbulence model trying to model attached flows with both laminar and turbulent separation of the boundary layer over circular cylinders. It was concluded that the main difference between the results and experimental data was found in the resultant Reynolds stresses and stated that *"the agreement is quite good for drag, shedding frequency, pressure and skin friction"* [38]. Furthermore, a high grid sensitivity was identified and it was pointed out that *"Unsteady Reynolds-averaged simulations are much less accurate than DES for LS cases, but very close for TS cases"* [38]. IDDES, DDES and other improved versions tried to fix these and another inaccuracies that have been found in the turbulence model along the years.

On the other hand, Menter & Egorov developed in 2008 the Shear Stress Transport Scale Adaptive Simulation model (SST-SAS) [26] based on RANS $k - \omega$ SST model presented by the first author in 1994 [25]. SAS models could be seen as an improved version of URANS formulation: *"The URANS simulation produces only the large-scale unsteadiness, whereas the SST-SAS model adjusts to the already resolved scales in a dynamic way and allows the development of a turbulent spectrum in the detached regions"* [73] as described in ANSYS Fluent manual. This model uses

the Von Kármán length-scale in the turbulence scale equation which makes the turbulence model to be capable to adjust the already resolved turbulence structures by a URANS simulation, resulting in a "*LES-like behaviour in unsteady regions of the flow field*" [73]. Anastasios Stamou & Georgia Papadonikolaki built a CFD code of the 3D flow around a static cylinder with SAS turbulence model and they concluded that "*Predicted overall flow parameters and mean flow velocities showed a very satisfactory agreement with experiments and LES, while the agreement of predicted turbulent stresses was satisfactory*" [59].

2.2 Circular Cylinders undergoing Vortex Induced Vibrations

Vortex Induced Vibration (VIV) is an aeroelastic phenomenon which generally takes place around bluff bodies such as, circular, rectangular or square cylinders. It occurs when the oscillatory behaviour of the fluid forces on the body makes it vibrate transversely to the main fluid flow. The oscillatory nature of the fluid forces over the structure is the result of the unsteady asymmetric behaviour of the periodic vortex shedding in the wake of the body and it can lead to a resultant structural failure. Hence, it is a common field of study in civil and marine engineering [47] because issues can be arisen around circular chimneys, electric grid cables, long span bridges, riser or pipelines [41] [39] [29] .

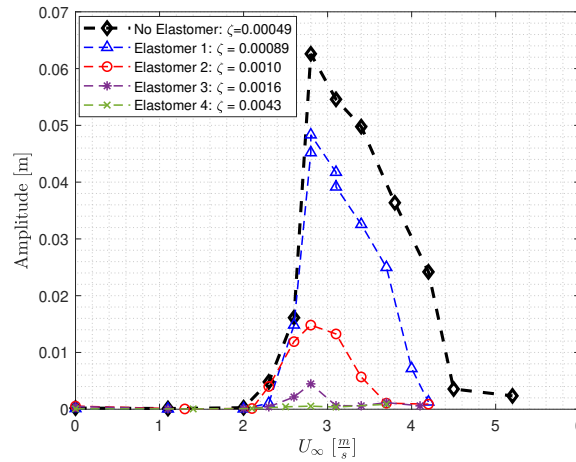


Figure 8: Maximum amplitude as a function of airspeed for several values of structural damping (ζ). Experimental data extracted from the Wind-Tunnel at Université de Liège. The aeroelastic system is constructed by a rigid circular cylinder supported by 4 lineal springs which can vibrate freely in cross direction to the fluid flow. The structural damping is modified by attaching different elastomers to the vibratory structure [66]

In a free (not fixed endings) cylinder at low windspeeds, the vortex shedding respects the Strouhal law ($St = \frac{f_{vs} D}{U_\infty}$) and it stays still as a fixed cylinder. For increasing flow velocities, however, the synchronization (lock-in) of the vortex shedding and the motion frequency can happen ($f_n = f_{osc}$) close to the natural frequency of the structure. At this airspeed called critical velocity, the vortex shedding and the oscillation frequency of the cylinder equate its natural frequency: $f_{osc} = f_{vs} = f_n$. At this point, the oscillatory motion of the cylinder suffers a steep increase on its amplitude. These last two phenomena (increase in amplitude and synchronization of

frequencies) characterize the lock-in region of an aeroelastic system undergoing VIV which stays over a range of windspeeds. Afterwards, when a maximum value of fluid velocity is overcome, the vortex shedding frequency follows back the Strouhal law and the amplitude of the motion tends to zero. The previously described frequency synchronization process and the band of the lock-in region depends on a reduced damping parameter called Scruton number ($Sc = \frac{4\pi m\zeta}{\rho D^2}$) which relates the damping force to the excitation force. As it is presented in Figure 8 [66], the higher it is, the lower the amplitude of the motion and the narrower the range of fluid velocities within the lock-in region. Moreover, high damping could completely erase the appearance of this aeroelastic phenomenon (Green line: Elastomer 4 in Figure 8 [66]).

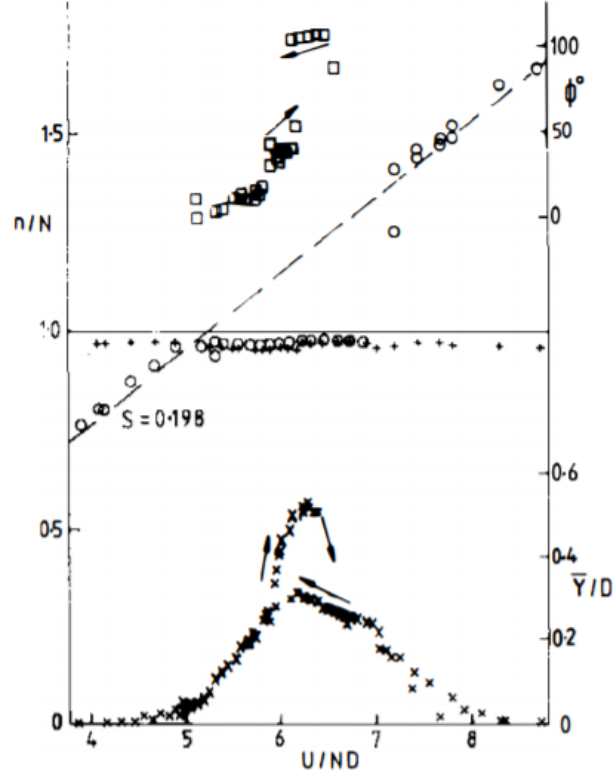


Figure 9: Oscillation characteristics for a freely vibrating circular cylinder with light damping ($2M\delta_s/\rho D^2 = 0.4$). N , body oscillating frequency ; n , vortex shedding frequency. \bar{Y}/D , normalized maximum amplitude of oscillation measured at a particular value of reduced velocity (U/ND) ; ϕ° , phase angle between the fluid force and the cylinder displacement. \circ vortex-shedding frequency; $+$ cylinder frequency; \square phase angle ; x oscillation amplitude [47] [18]

The main properties of VIV and its characteristic lock in region are summarized in Figure 9 which was extracted by Feng [6] for the first time in 1968 and validated and discussed by Bearman [17] in 1984. Eventually, it was also presented by R.D. Gabbai and H. Benaroya [47] in 2005 in an overview of the most important experimental researches in Vortex Induced Vibrations up to date.

Figure 9 shows the evolution of three parameters (normalized vortex shedding frequency, $n/N = f_{vs}/f_{osc}$; phase between the lift force and the structural motion, ϕ ; non-dimensional amplitude, $\bar{Y}/D = |y|/D$) as a function of reduced velocity (U/ND). Furthermore, the dashed line represents the Strouhal law with $St = S = 0.198$. Feng [6] found that at a critical value of the

reduced velocity equal to the inverse of the Strouhal number the lock-in region arises. At this region, the vortex shedding frequency equates the natural frequency of the oscillating structure, the amplitude of the motion suffers an abrupt increase and there is a phase shift of about $\sim 100^\circ$ between the structural motion and the fluid forces over the cylinder in the direction of the motion. Figure 10 shows an enlarge plot of the phase jump at lock in boundary. Bearman [17] relates this change in phase angle with a drastic variation of "the point at which a forming vortex generates its maximum lift force" [17] due to a variation of the reduced velocity. Further analysis have been carried out by Zdravkovich [16], who realized that the timing of the vortex shedding changes at this boundary. While, at lower reduced frequencies the vortex is shed when the cylinder has its maximum amplitude on the opposite side; when the motion is locked, the vortex is shed when the cylinder is in the maximum point in the same direction.

Figure 9 also presents the hysteresis behaviour of the VIV phenomenon discovered by Feng [6]. He measured larger amplitudes of the structure within the lock-in region when increasing the reduced velocity rather than when moving from higher to lower values of U_∞ . Furthermore, this behaviour was also identified in the evolution of the phase (Figure 10). Afterwards, several authors associated this behaviour with different wake structures and the transition between them (motion between upper and lower branches) [47] [21] [11]. The previous statement was confirmed by Khalak & Williamson [33] and Govardhan & Williamson [34] with experimental investigation based on elastically mounted cylinders in the 2000s.

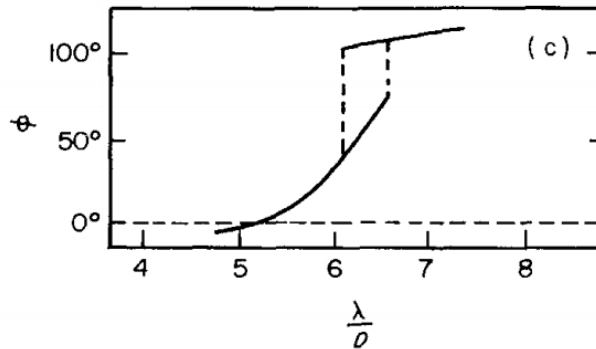


Figure 10: Variation of the phase difference of the lift force with respect to the motion of the cylinder for increasing values of the wavelength ratio ($\lambda/D = U_\infty/f_{osc}D$) for an elastically-mounted cylinder. Extracted from Feng [6]

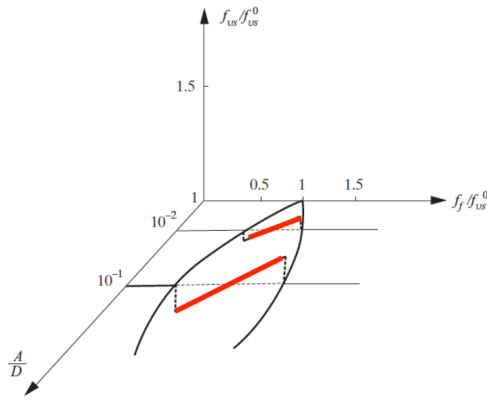
2.3 Flow over Oscillating Circular Cylinder under Imposed Motion

A large number of authors have developed research projects in order to analyze VIV. Oscillations of bluff bodies may be vortex-induced (aeroelastic) or forced by a mechanism able to produce sinusoidal motion by imposing a frequency and/or an amplitude. However, while some of them (e.g Feng [6], T. Sarpkaya [11] or Griffin and Ramberg [19]) decided to carry out experiments on flexible structures able to vibrate freely on a stream; others (Bearman [17], Roshko & Williamson [21], Bishop and Hassan [3] or Ongoren & Rockwell [20]) went for imposing an oscillatory motion

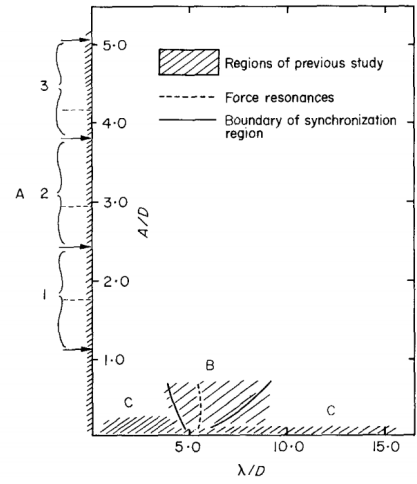
to a bluff body.

Roshko and Williamson considered that "forcing a cylinder to oscillate up to large amplitudes in a freestream..." [21], they could "...investigate under more controlled conditions how a body influences its own wake to cause synchronisation" [21].

Bearman [17] assumed that "for a freely suspended bluff body oscillating at a steady amplitude, if the same body is forced to oscillate at a similar amplitude ratio, reduced velocity, and Reynolds number, then the flow patter will be identical" [17]. The previous statement was done based in experimental data at that time which suggested that "free and forced-vibration flows are the same" [17]. However, further discussion on the topic proved that the relationship between the two cases is "surprisingly complicated" [45] as described by J. Carberry, J. Sheridan and & D. Rockwell [45].



(a) Lock in region [67]



(b) Synchronization region [21]

Figure 11: Representation of the lock-in region by several authors. (a) lock-in region for imposed motion cylinders on the plane "imposed amplitude-imposed frequency" extracted from [67]. (b) synchronization region on the plane "amplitude-wavelength" being the region marked with a "B" extracted from [21]. Definition of the wavelength: $\lambda = U_\infty T_{osc} = U_\infty / f_{osc}$

The imposed motion of the bluff body can take control over the vortex shedding process and modify it significantly with respect to the one around an static or fixed body. Moreover, as it happens in freely oscillating cylinders, a synchronization (or lock-in) region arises. However, significant differences exist between both cases. As presented in Figure 11, the structural motion takes control of the vortex shedding and both happen at the same frequency in a range of imposed frequencies (f_{osc}) in Figure 11a. Figure 11b also presents the lock-in or synchronization region as named by C. H. K. Williamson & A. Roshko in his article [21] (from which Figure 11b was extracted). However, he decided to plot it against the wavelength ratio. The zone marked with a B represents the region where the vortex shedding happens at the frequency of the imposed motion. The lock in region presents close to an inverted triangular shape in the imposed amplitude vs frequency domain. At low amplitudes the synchronization will take place at a narrow range of motion frequencies close to the vortex shedding frequency of the equivalent

static cylinder. Increasing the imposed amplitude, this band gets wider capturing both higher and lower frequencies.

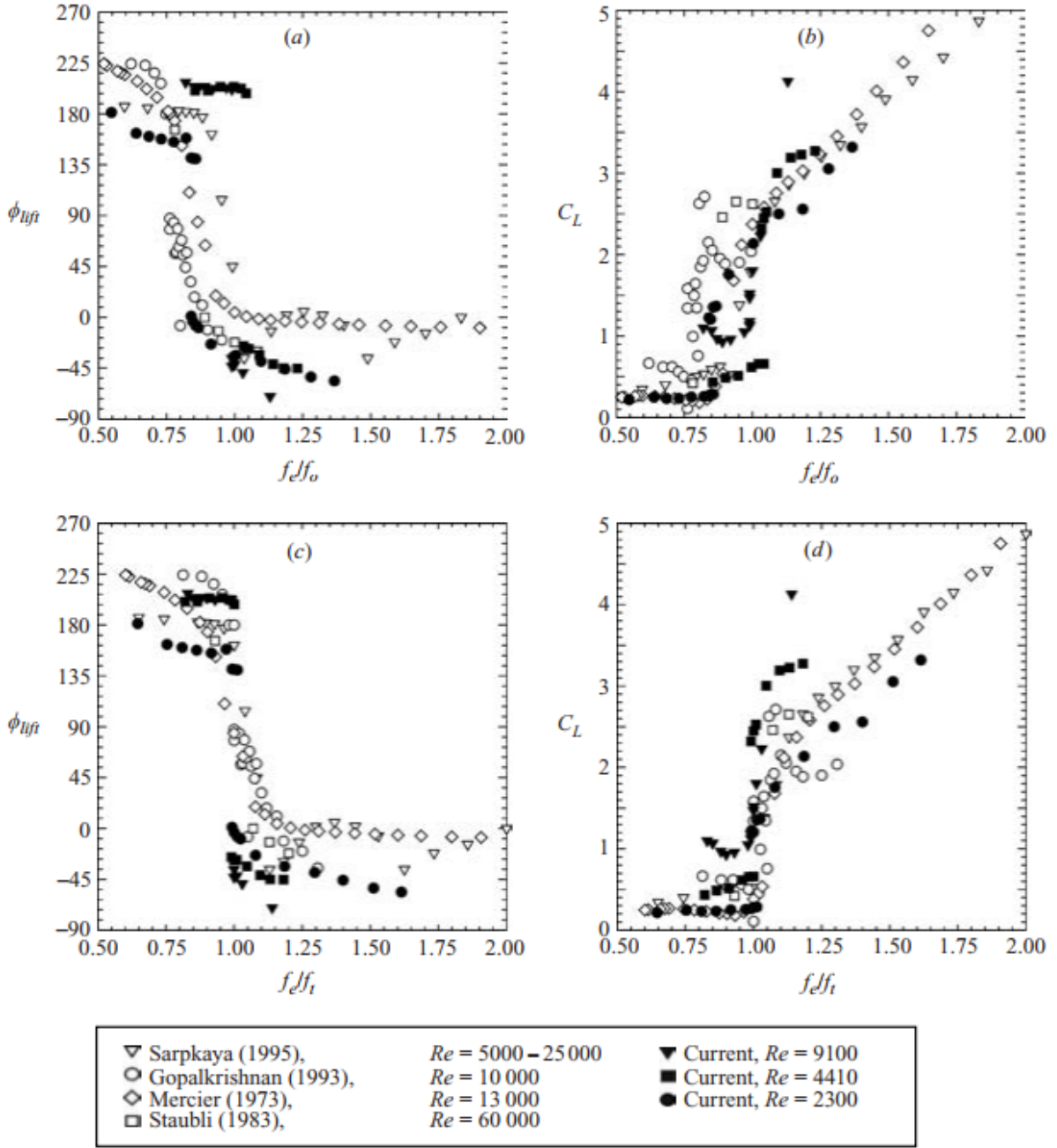


Figure 12: Data recompilation from several authors of the field: ϕ_{lift} and C_L as a function of $f_e/f_o = f_{osc}/f_{vs}^o$ and $f_e/f_t = f_{osc}/f_{vs}$ for $|y|/D = 0.5$. $|y|$, amplitude of the imposed motion of the cylinder; $f_o = f_{vs}^o$ vortex shedding frequency from a stationary cylinder; $f_e = f_{osc}$, imposed frequency motion of the cylinder; $f_t = f_{vs}$, vortex shedding frequency from an oscillating cylinder (*"it is expected to deviate slightly from $f_o = f_{vs}^o$ "* [45]). "Current" refers to data obtained and presented by J. Carberry, J. Sheridan & D. Rockwell [45]. Extracted from [45]

J. Carberry, J. Sheridan and & D. Rockwell mentioned *"As the frequency of the force oscillation*

is changed relative to the natural frequency of the stationary cylinder's wake, there are abrupt changes in both the lift forces on the cylinder and the structure near wake" [45]. This conclusion was taken after comparing the work done by several authors in the topic at different Reynolds numbers such as Sarpkaya [28], Gopalkrishnan [24] or Mercier [8] validating those results with their own research presented in Figure 12. Again, instead of presenting the results as a function of the wavelength ratio as done by several previous authors, they discussed the effect of the ratio between the motion frequency and the natural frequency of the stationary cylinder's wake (f_{osc}/f_{vs}^o). It can be seen clearly that in all the cases "There is a simultaneous jump in the amplitude and phase of the lift force at $f_{osc}/f_{vs}^o \sim 1$...related to changes in the flow structures in the wake" [45].

C. H. K. Williamson & A. Roshko [21] made an extensive experimental analysis of the wake patterns of oscillating circular cylinders in the "wavelength-amplitude" plane. The study reached up to imposed amplitudes of 5 times the diameter and wavelengths of 16 diameters. Figure 13 and Figure 14 presents the vortex shedding patterns captured and identified by the previous authors near the fundamental lock-in region.

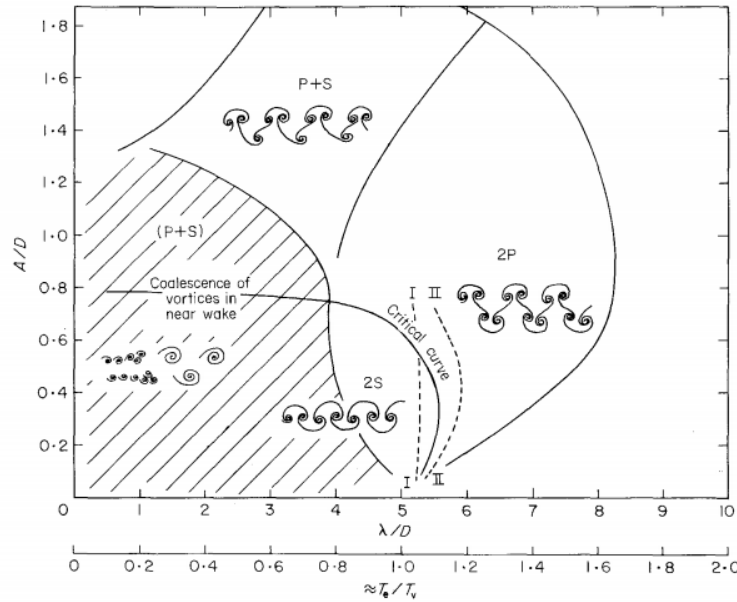


Figure 13: Map of vortex synchronization patterns near the fundamental lock-in region from [21]. I and II are the curves where the forces on the body show a sharp "jump" from Bishop and Hassan [3]

They defined that "The well-known lock-in occurs when the trajectory wavelength is comparable with the distance a non-oscillating cylinder travels through the fluid in one cycle of shedding" [21]. Within this region they also defined two behaviours:

- Below a critical wavelength, two regions of opposite vorticity are shed resulting in a 2S mode.
- Over a critical wavelength, the wake is formed by a system of vortex pairs convecting away

from the wake centerline. In other words, a 2P mode.

- The transition point coincides with the wavelength value at which the fluid forces suffers an abrupt change pointed by Bishop & Hassan [3].

Furthermore, they also pointed out that "over a small range of wavelengths either of the two modes described above may exist, with the chosen mode depending on the flow history" [21]. This last statement refuses the assumption made by Bearman [17] and mentioned before in this section, but instead, gives an possible explanation to the hysteresis behaviour of the motion amplitude undergoing VIV measured by Bishop & Hassan [3].

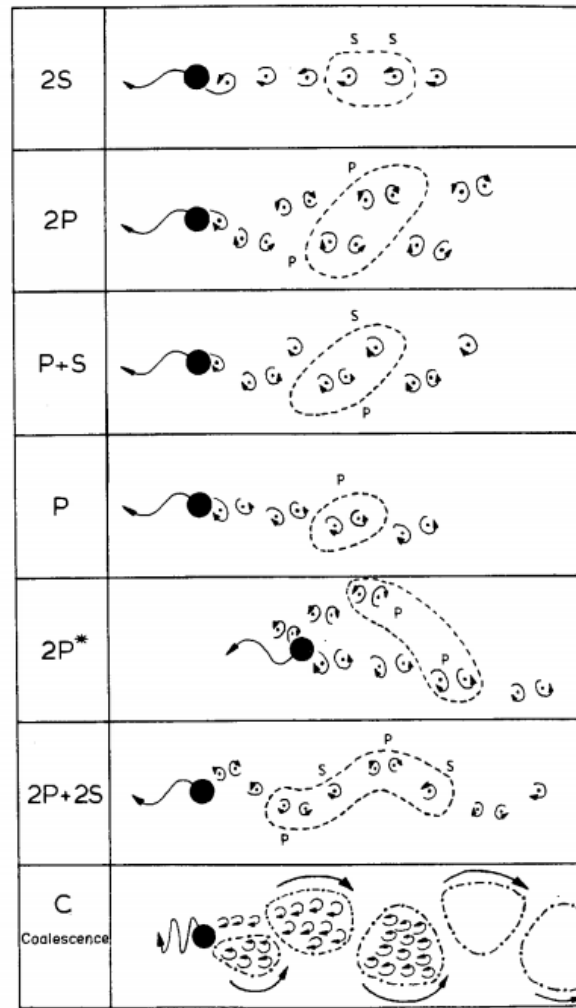


Figure 14: Sketches of the vortex shedding patterns that were found by Williamson and Roshko in [21]. "P", a vortex pair ; "S", single vortex. Each pattern is defined by the number of pairs and single vortices formed per cycle. Dashed line encircles the vortices shed in one complete cycle. Extracted from [21]

Several years later, J. Carberry, J. Sheridan and & D. Rockwell also analyzed the vortex shed-

ding patterns of oscillating cylinders at imposed motion in [45]; this time, however, the effect of the imposed motion frequency was only analyzed at constant amplitude. They concluded that within the lock-in region, two different wake states can be defined: low-frequency and high-frequency. The former, results in a 2P vortex pattern at which the lift force has a low amplitude and a phase of about 180° with the motion of the cylinder. The latter, instead, presents a 2S pattern at which the lift force has a higher amplitude and the phase goes down to negative values. In the middle, an abrupt transition of the values takes place at around $f_{osc}/f_{vs}^o = 0.85$. This behaviour matches close to the one presented by C. H. K. Williamson & A. Roshko [21] and Bishop & Hassan [3]. Moreover, they also defined a transition region over a narrow band of frequencies. When forcing the structure with a frequency within this region, the wake could shed in either 2P (low-frequency state) or 2S (high-frequency state) mode. However, also a self-excited transition from the lower to the high frequency state is possible. "*The self-excited transition was irreversible and transition always occurred from low-frequency to the high-frequency state*" [45] declared the authors who related these states with the upper and lower branches of the hysteresis presented in cylinders undergoing VIV.

The sudden change of the phase of the lift coefficient time signal with respect to its motion has a strong impact in the energy transfer between the fluid and the oscillating structure.

On the one hand, in vortex induced vibration the energy transfer must go from the fluid to the structure; in other words, "*The structure responds to the perturbation from the natural instability of the wake*" [45] as described by J. Carberry, J. Sheridan and & D. Rockwell.

On the other hand, when forcing the structure to move in a specific way, it perturbs the natural instability of the wake, causing the wake to respond. Hence, theoretically the energy transfer could be in either direction. The previous authors realized that due to the abrupt decrease of ϕ_L from $\sim 180^\circ$ before the transition to $\sim -45^\circ$ after it, switches the direction of the energy transfer within the aeroelastic system. While in the low frequency state (corresponds to the lower branch of VIV) the energy transmission goes from the fluid to the structure; in the high frequency state (corresponds to the upper branch of VIV), the energy goes in the opposite direction.

This last fact demonstrates that even if there are great similarities between freely vibratory cylinders and forced ones regarding wake structures and evolution of the forces over the cylinder, "*...the force purely sinusoidal oscillations do not fully represent the almost sinusoidal motion of the freely oscillating cylinder*" [45] as stated by the last authors.

The whole previous analysis (cylinders undergoing VIV or at forced motion) was based on the vibratory motion in cross direction to the incoming fluid flow. However, in-line vibrations are also important specially for systems with low structural damping [11]. Compared to the cross-flow oscillations, lock-in takes place when the in-line motion frequency reaches around twice the Strouhal frequency. Furthermore, the oscillation amplitude of motion of the cylinder and the drag fluctuations are one order of magnitude smaller [11]. In the last years, several authors have carried out experimental projects on this topic and 2 DOF VIV experimental and numerical projects ([56] [58] [50]).

3 Experimental Results

3.1 Introduction

The first step of the project is the validation of the developed CFD codes for the numerical study of the unsteady pressure distribution on the oscillating cylinder. This validation will be carried out based on empirical data extracted from a Vortex Induced Vibration (VIV) experiment in a wind tunnel. The data was obtained by Prof. Thomas Andrianne at Université de Liège Wind Tunnel during the academic year 2019-2020.

It consisted in a circular cylinder vertically supported in a structure that allows it to freely vibrate in cross direction to the incoming air flow. The experiment was performed at different airspeeds. The unsteady pressure over the cylinder and wake velocity components were extracted. Also, the motion (amplitude) of the cylinder was recorded.

First, the VIV data has been analyzed in order to place the lock-in region: maximum amplitude, Strouhal number (St), natural frequency (f_n) of the structure and vortex shedding frequency (f_{vs}) at each airspeed. Then, based on those results, two cases, one outside of the lock-in region and one undergoing VIV, have been chosen and will be compared to numerical simulations in order to validate the latter ones. Eventually, further analysis of the elected cases will be performed. More specific results, such as, the time mean pressure coefficient, \bar{c}_p , distribution over the cylinder, time evolution of $c_L(t)$ and $c_D(t)$, velocity in the wake will be presented and discussed at the end of the chapter.

3.2 Wind Tunnel

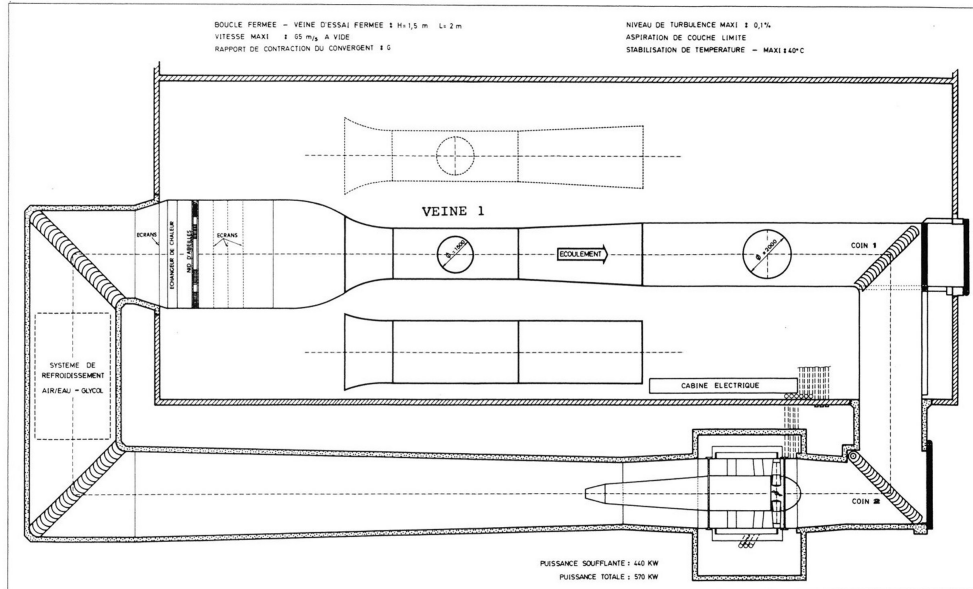


FIGURE 1. - VEINE 1 - BOUCLE POUR ETUDES D'AERONEFS ET DE VEHICULES AUTOMOBILES

Figure 15: Drawing of the Wind Tunnel Facility at ULiège [72]

The wind tunnel owned by Université de Liège consists of a multi-disciplinary subsonic wind tunnel characterized by its modularity which allows to vary between two test-sections (Aeronautic or Wing Engineering Test Section) and two interchangeable nozzles. Figure 15 presents a general drawing of the wind tunnel facility.

The test section used for the experimental activity was the former. It can work up to a maximum windspeed of 65 [m/s] in atmospheric conditions with a low incoming turbulence level ($Ti \sim 0.2\%$). It is equipped with various measurement systems to carry out experiments at low Mach number ($M < 0.15$). The front and top walls of the section are built on perspex panels which equips the facility with high visibility of the tests. Its dimensions are 2 [m] width by 1.5 [m] height.

3.3 Test Rig



Figure 16: VIV Test Rig [72]

The test rig is presented in Figure 16. It is composed by a smooth circular cylinder made out of PVC placed vertically inside the aeronautic test section of the wind tunnel. The cylinder is suspended on 4 linear springs at each end of it. The cylinder can vibrate freely in the transverse direction of the incoming air flow. The resultant natural frequency of the structure (cylinder and support) is $f_n = 7.07$ [Hz]. The cylinder has a diameter $D = 0.1$ [m] and a spanwise length $L = 1.5$ [m], which results in an aspect ratio $\frac{L}{D} = 15$. As verified by a large amount of authors in an extensive literature ([23] [53] [52]...), the value of this ratio has a great impact on the magnitude of the 3D effects and oblique shedding that will appear in the static set-up of the cylinder. This last phenomenon will be also af-

ected by the Reynolds number and the roughness of the cylinder. Hence, it will be mentioned in subsection 3.5 when discussing the testing conditions.

3.4 Measurement Systems

The objective of the experiment is the measurement of the unsteady aerodynamic loading on the cylinder and the evolution of it when switching from unlocked to locked cases. Hence, three main parameters will be of interest for the present report: (a) the amplitude of the motion of the cylinder, (b) the time evolution of the pressure on the cylinder and (c) the velocity of the fluid within the wake region just after the circular cylinder. In order to do so, the following measurement systems have been used:

- **Unsteady Loading:** 36 pressure taps have been uniformly distributed around the mid-span section of the cylinder (Figure 17). These pressure taps are connected to a scanner located outside the test section by plastic tubes. The scanner allows synchronous pressure measurements of all the taps. Moreover, it is also connected to an anemometer which

measures the static pressure of the incoming air and gives to the user the value of c_p (Equation 11) at each pressure tap directly.

- **Amplitude of the Cylinder:** The motion of cylinder is analyzed in terms of the time evolution of its amplitude. It has been recorded by means of laser measurements [72]. This parameter will allow the extraction of f_n from a frequency domain analysis of the motion; as well as, the detection of the lock-in region.
- **Fluid Velocity in the Wake:** A cobra probe located downstream, just behind of the mid-span section of the cylinder will be used for this purpose (Figure 17). It is capable to measure the different components (u, v, w) of velocity. It allows detecting the order of magnitude of the 3D effects present in the wake and vortex shedding of the cylinder. Also, the shedding frequency (f_{vs}) and the Strouhal number (St) will be extracted from this data. Eventually, the lock-in region will be identified based on the results extracted from it.

All the data has been measured synchronously at $f_s = 300$ [Hz]

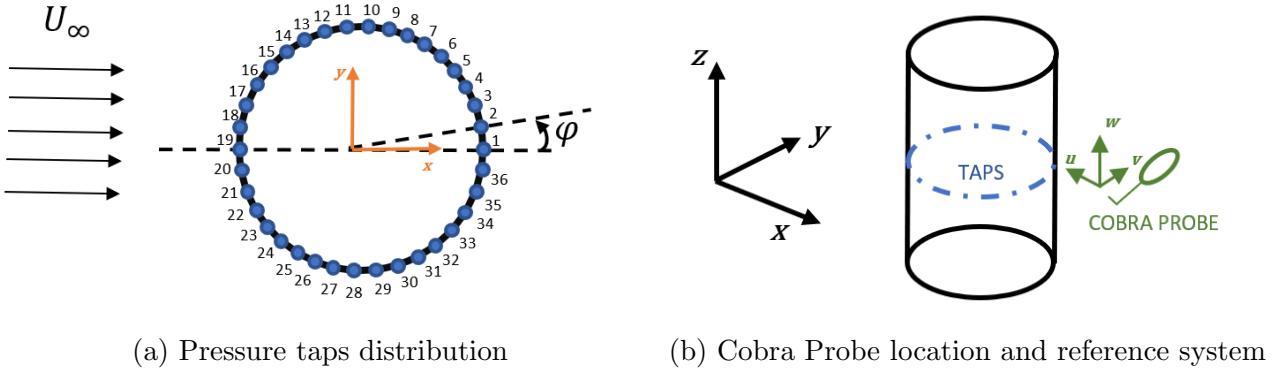


Figure 17: Sketches of the measurement and reference systems set-up

3.5 Testing Conditions

The experiment consists in the recording of the previously presented data at a range of different airspeeds aiming to locate the lock-in region and the point at which the circular cylinder undergoes VIV. Then, the loading will be analyzed.

The experiment has been carried out in the range $[1.5-9.1]$ [m/s] of airspeed at 29 different values; first, in increasing order from 0 [m/s] up to 9.15 [m/s] and afterwards in opposite direction down to 3.1 [m/s]. By proceeding this way, the inherent hysteresis of the VIV will be captured. These values will result in the range of Reynolds number $Re \in [10^4 - 6 \cdot 10^4]$. Under this conditions, the boundary layer around the static cylinder will be laminar; the shedding vortices, however, turbulent. The regime transition will happen in the shear layer, after the laminar separation occurs (Figure 4). This physical phenomenon will be considered in the CFD simulations as it is known from the literature that the behaviour of the boundary layer, separation point and the

near wake region affects the pressure distribution around the cylinder. The drag coefficient will be specially affected by it. Moreover, there will be low incoming turbulence level ($Ti = 0.2\%$).

Regarding the $\frac{L}{D}$ ratio, it is known from the literature research ([23] [15] [27]) that under these operating conditions, $\frac{L}{D} \geq 25$ would give independent conditions at mid span free of oblique vortex shedding. Hence, a velocity component in the spanwise direction as well as 3D vortex shedding are expected in our experimental data, at least for the static cylinder.

As a summary, the principal testing conditions under which the experiment has been performed are listed below.

- Low incoming turbulence conditions: $Ti = 0.2\%$
- Range of Free-stream velocity: $U_\infty \in (1.5 - 9.1)$ [m/s]
- Reynolds number: $Re \in (1 \cdot 10^4 - 6 \cdot 10^4)$

3.6 General VIV Results

3.6.1 Modal Properties of the Cylinder and the Supporting Structure

In order to find the natural frequency (f_n) of the system at wind-off, a test has been performed at $U_\infty = 0$. The frequency at which the structure vibrates will be extracted by means of Fourier Analysis of the time response of the cylinder recorded by the laser. Figure 19 shows that the motion of the cylinder has a base frequency at $f_n \sim 7.07$ [Hz] and higher frequency components which are multiples of it. However, higher harmonics can be neglected in terms of order of magnitude. Furthermore, Half Power method (Figure 18) have been used to obtain the inherent damping ratio, ζ_n (Equation 2), of the system. The modal properties of the system are presented in Table 1.

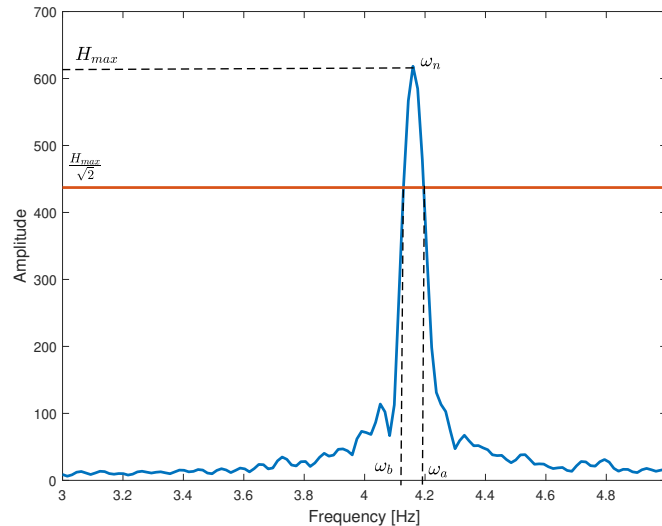


Figure 18: Graphical representation of the Half Power Method extracted from [65]. Figure is presented in order to define the damping ratio, ζ_n . Numerical data presented is independent of the current project

$$\zeta_n = \frac{\Delta\omega}{2\omega_n} = \frac{\Delta f}{2f_n} = \frac{f_a - f_b}{2f_n} \quad (2)$$

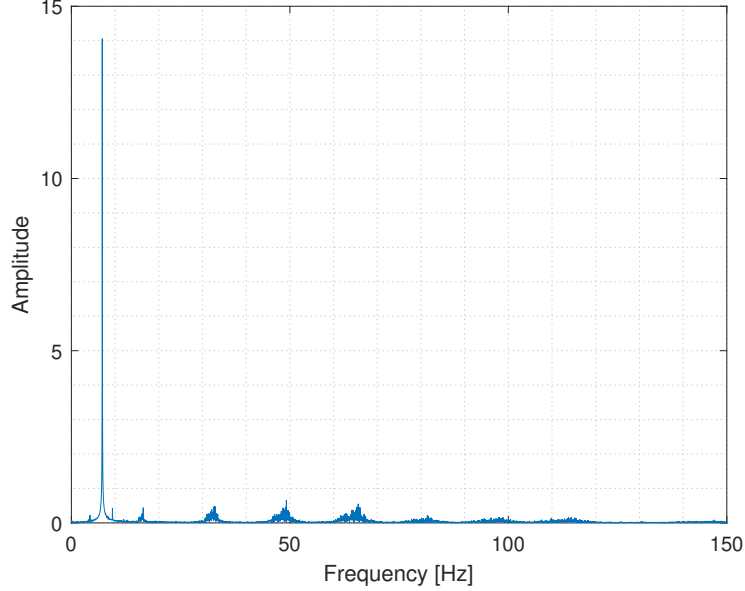


Figure 19: FFT of the time displacement of the cylinder at wind-off test

f_n [Hz]	7.0675
ζ_n [-]	0.0024

Table 1: Natural frequency (f_n) and damping ratio (ζ_n) of the structural mode identified in the experimental setting of the circular cylinder at wind-off ($U_\infty = 0$)

3.6.2 Displacement of the Cylinder

The experiment has been carried out at 29 different airspeeds; first, in increasing order from 0 [m/s] up to 9.15 [m/s] and afterwards in opposite direction down to 3.1 [m/s]. This way, the possible hysteretic behaviour that characterizes VIV aeroelastic phenomenon is captured.

In order to locate the region at which the cylinder undergoes Vortex Induced Vibration (VIV), the maximum amplitude and the standard deviation of its motion have been computed. There is a range of airspeeds where the system suffers from a self-induced and self-sustained vibratory motion. Switching to higher or lower values outside of it, the motion of the cylinder decays to zero, stopping the VIV. Figure 20 shows the cylinder motion for increasing values of windspeed. It can be seen that at $U_\infty \sim 4$ [m/s] the amplitude of the motion of the cylinder increases drastically leading to Vortex Induced Vibration (VIV) phenomenon.

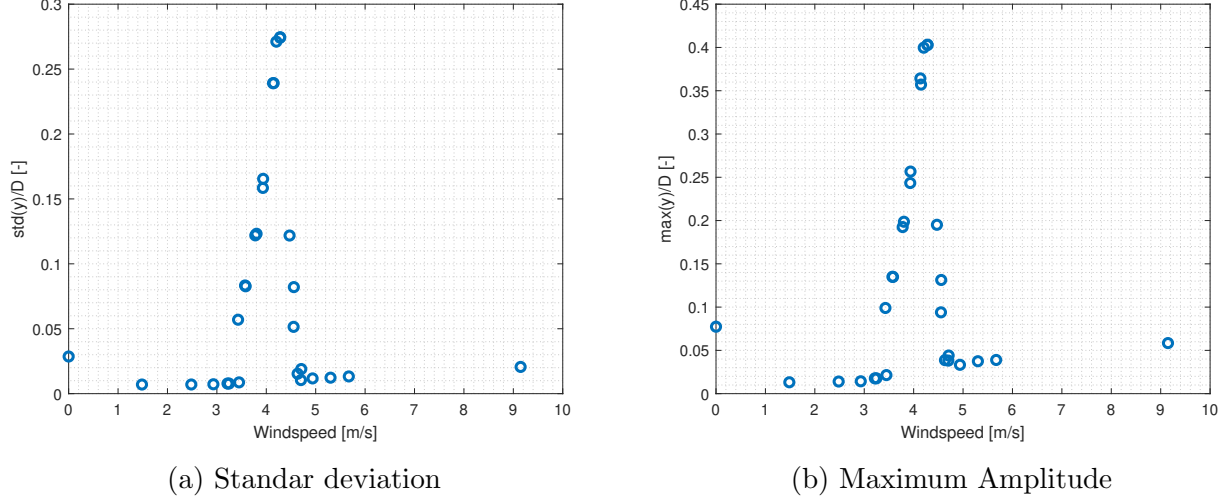


Figure 20: Evolution of the non dimensional standard deviation of the amplitude (left) and maximum amplitude (right) of the motion of the cylinder for increasing values of windspeed

3.6.3 Lock-in Region

The lock-in region is a range of windspeeds at which the shedding frequency of the flow is led by the motion of the structure. In this case, by the displacement of the rigid cylinder vibrating in cross direction to the incoming fluid flow.

The vortex shedding frequency (f_{vs}) will be computed from the time evolution of u component (see Figure 17) of the flow velocity in the wake region just behind the cylinder. Figure 21 presents the shedding frequency at each airspeed. Also, the natural frequency (f_n) of the vibrating cylinder and the Strouhal law are shown. The shedding frequency of the cylinder follows the Strouhal law up to ~ 4 [m/s] of windspeed. At that point, it equates the natural frequency of the structure ($f_n = 7.07$ [Hz]) and it keeps constant until $U_\infty \sim 4.9$ [m/s]. This region is known as the lock-in region and coincides with the drastic increase in the amplitude of the cylinder's motion.

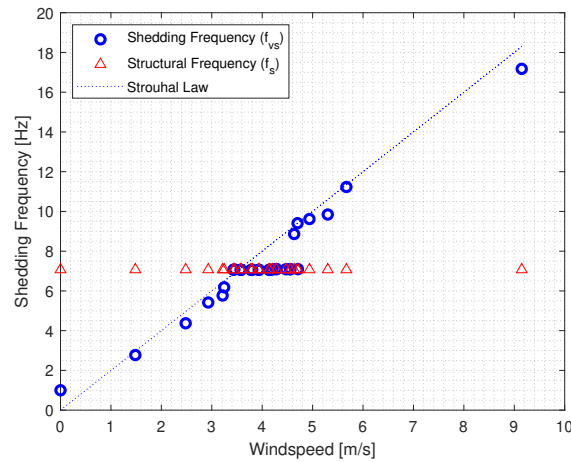


Figure 21: f_{vs} , \circ , & f_s , Δ , as a function of the windspeed from experimental data

3.7 Cases for CFD Code Validation

From the previously ran 29 cases (neglecting wind-off), two have been selected to validate the CFD codes. On the one hand, the case with the smallest amplitude of the cylinder ($U_\infty = 1.4839$ [m/s] & $Re \sim 1 \cdot 10^4$) for the static case with a shedding frequency of $f_{vs} = 2.78$ [Hz]. On the other hand, the cylinder undergoing VIV at $U_\infty = 4.2786$ [m/s] ($Re \sim 2.9 \cdot 10^4$) will be chosen to verify the model of the oscillating or moving cylinder. The aerodynamic parameters will be the reference validation parameters. Hence, the time mean pressure coefficient (\bar{c}_p) over the mid-span section of the cylinder and the time evolution of the drag ($c_{D_{exp}}$) and lift ($c_{L_{exp}}$) coefficients will be extracted from the recorded data. Also, the shedding frequency (f_{vs}).

Moreover, the time evolution of the w component of velocity in the wake extracted from the Cobra Probe will give the order of magnitude of the 3D behaviour of the flow in that region.

Eventually, the Strouhal number (St) will be computed from both the u component of the flow velocity in the wake and from the oscillatory behaviour of $c_{L_{exp}}$.

3.7.1 Case at $U_\infty = 1.4839$ [m/s] ($Re \sim 1 \cdot 10^4$)

- Time Mean Pressure Coefficient (\bar{c}_p)

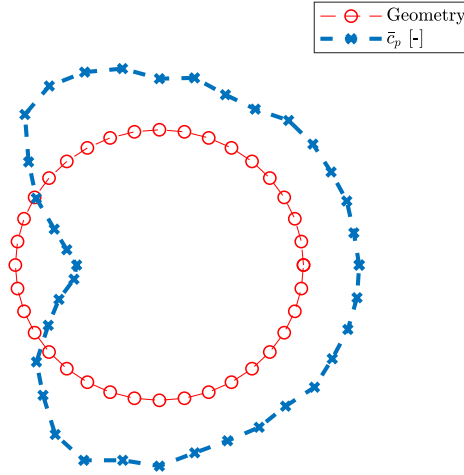


Figure 22: Time mean distribution of the pressure coefficient (\bar{c}_p) over the mid-span section of the static cylinder at $Re \sim 1 \cdot 10^4$. Plotted over the geometry of the circular section

Figure 22 and Figure 23 present the time mean distribution of the 2D pressure loading of the cylinder at the mid-span section at $U_\infty = 1.4839$ [m/s] ($Re \sim 1 \cdot 10^4$). The former shows \bar{c}_p distribution plotted over the circular section that characterizes the geometry of the cylinder. It can be observed that the aerodynamic loading is not symmetric with respect to the "horizontal" symmetry axis of the circle. The geometrical non-uniformity

of the circular section or the surface roughness could result in a non-symmetrical loading. Furthermore, the amplitude of the displacement of the cylinder is not completely null (Figure 20) which can also modify the ideal symmetric \bar{c}_p distribution over the mid-span section of the cylinder. The latter shows \bar{c}_p as a function of the angular coordinate φ (Figure 23a) and as a function of the streamwise coordinate x (Figure 23b). Both verify the non-symmetric distribution of the 2D loading on the cylinder.

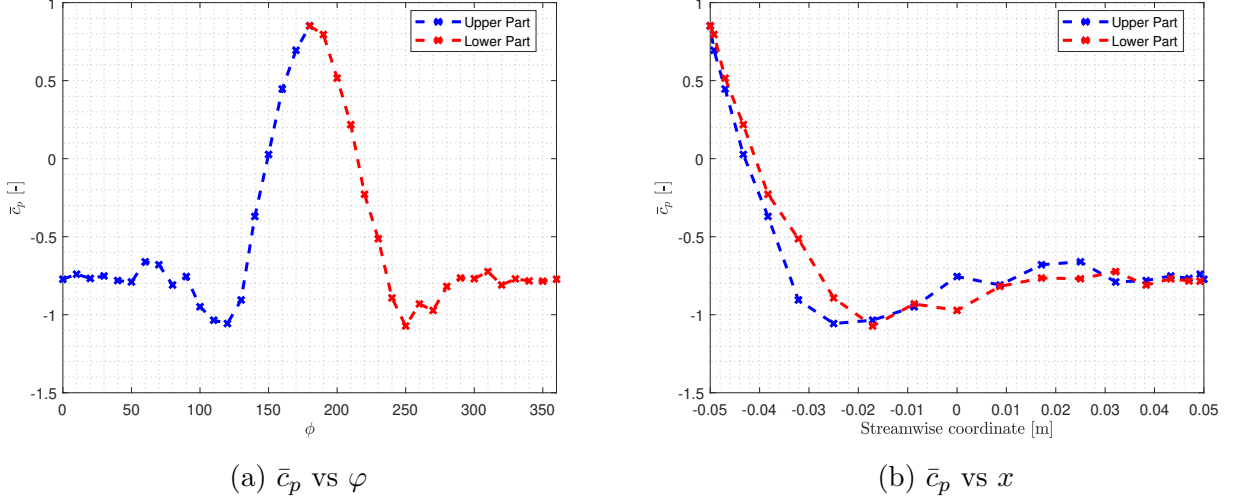


Figure 23: Time mean loading of the cylinder at $Re \sim 1 \cdot 10^4$. \bar{c}_p as a function of the angle φ (left). Where, φ is the angle defined in Figure 17a positive in the increasing direction of the numbering of the pressure taps. \bar{c}_p as a function of the streamwise coordinate x (right). This coordinate starts at the center of the circular section and it is positive downstream (see Figure 17a).

• Time Evolution of Lift Coefficient (c_{Lexp}) and Drag Coefficient (c_{Dexp})

Figure 24a shows the time evolution of the 2D lift and drag coefficient computed directly from experimentally recorded c_p at mid-span section defined in subsection A.5. A FFT of the former is presented in Figure 24b. Theoretically, for a perfect circular geometry and homogeneous flow the steady component of c_{Lexp} should be zero; however, it is not, even if close to it. The mean component of the time distribution (or the component related to 0 [Hz] frequency of the FFT) verifies the previous statement. Moreover, even if some noise is included in the recorded data (possibly, due to the low velocity of the incoming wind and the non-zero vibration of the structure), a main oscillating frequency (and its higher multiple frequencies) can be identified from the Fourier analysis. Table 2 captures the parameters that characterizes the behaviour of these aerodynamic parameters.

\bar{c}_{Lexp} [-]	\bar{c}_{Dexp} [-]	$f_{c_{Lexp}}$ [Hz]
-0.0264	0.7212	2.8

Table 2: Time mean values of lift and drag coefficients computed from the experimental pressure distribution over the mid-span section at $U_\infty = 1.4839$ [m/s] ($Re \sim 1 \cdot 10^4$). Main frequency of the time distribution of experimental lift coefficient

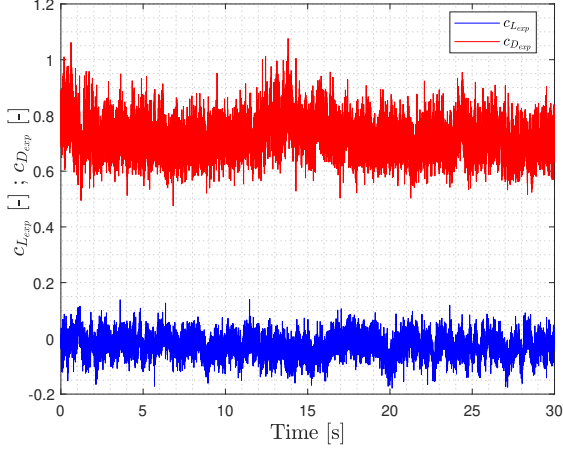
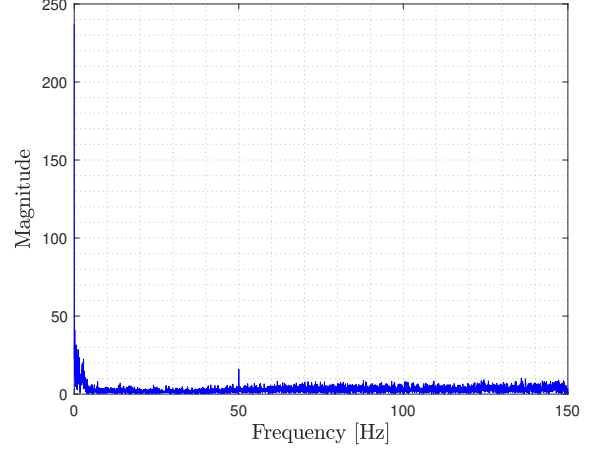

(a) $c_{L_{exp}}(t)$ & $c_{D_{exp}}(t)$ vs time

(b) FFT of $c_{L_{exp}}(t)$

Figure 24: 2D lift and drag (left) coefficients at mid-span section of the cylinder obtained from the experimental data at $U_{\infty} = 1.4839$ [m/s] ($Re \sim 1 \cdot 10^4$). Time distribution (left) ; FFT analysis of $c_{L_{exp}}$ (right)

• Wake Velocity

On the one hand, Figure 25 shows the time distribution of the velocity components in the wake recorded by the Cobra Probe. The streamwise component (u) is one order of magnitude higher than the others (v and w). However, even if close to zero, there is a small component of velocity in span-wise direction, which will force us to perform 3D numerical calculations to well-capture the experimental unsteady loading on the mid-span section of the cylinder. It will be discussed in section 4.

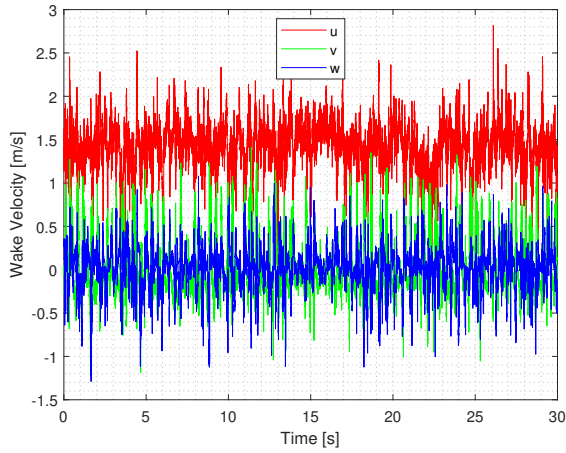
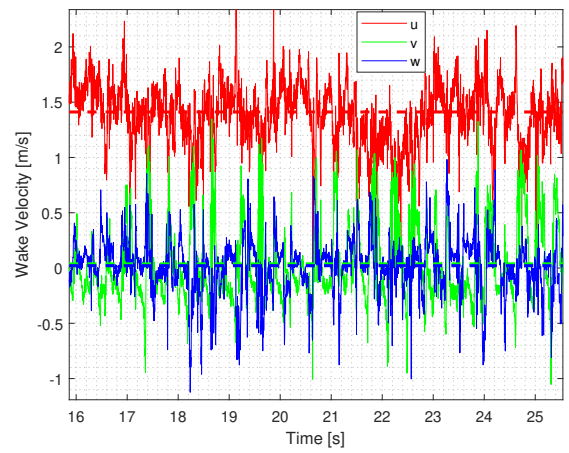

(a) Wake velocity vs time ($t \in [0 - 30]$ s)

(b) Wake velocity vs time ($t \in [16 - 25]$ s)

Figure 25: Time distribution of the wake velocity recorded by the Cobra Probe at $U_{\infty} = 1.4839$ [m/s] ($Re \sim 1 \cdot 10^4$). Streamwise component (u), spanwise component (w), orthogonal component to the others (v). See Figure 17b

On the other hand, the FFT analysis of the wake velocity (Figure 26) reveals a vortex shedding frequency of $f_{vs} = 2.78$ [Hz].

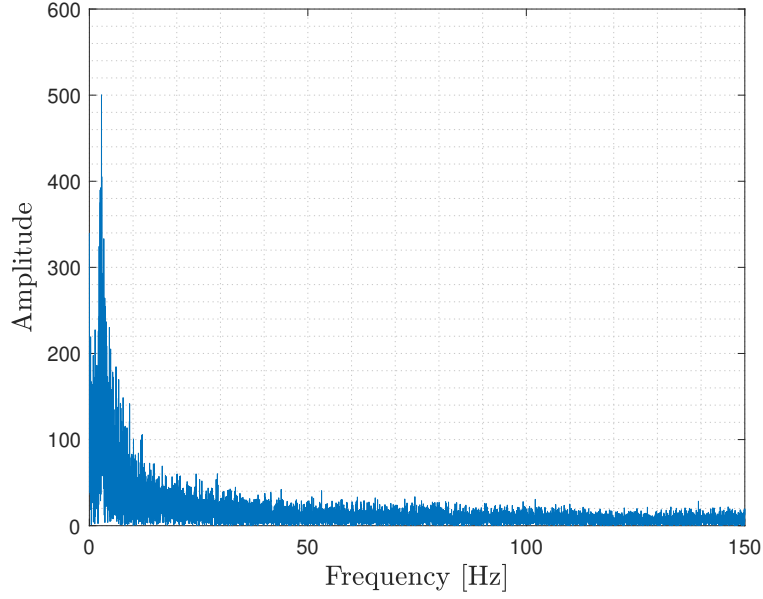


Figure 26: FFT of the Wake Velocity at $U_\infty = 1.4839$ [m/s] ($Re \sim 1 \cdot 10^4$)

\bar{u} [m/s]	\bar{v} [m/s]	\bar{w} [m/s]	f_{vs} [Hz]
1.4116	0.0378	0.0212	2.78

Table 3: Time mean value of each wake velocity component and oscillation frequency of the lift coefficient at $U_\infty = 1.4839$ [m/s] ($Re \sim 1 \cdot 10^4$)

• Strouhal Number (St)

As many authors have made reference to it ([44] [22] [9] [7]) the lift coefficients oscillates at the vortex shedding frequency (or really close to it). Table 4 collects both frequencies and the Strouhal numbers related to them. Both values are close to each other and the corresponding St matches the generally used value for circular cylinders ($St = 0.2$) and experimental results with oblique shedding ($St = 0.18$) [53] [52].

from:	$c_{Lexp}(t)$	$vel_u(t)$
f_{vs} [Hz]	2.78	2.8
St [-]	0.1887	0.1869

Table 4: Shedding frequency and Strouhal number obtained from (a) time distribution of the experimental c_L and (b) time distribution of the fluid velocity in the vortex at $U_\infty = 1.4839$ [m/s] ($Re \sim 1 \cdot 10^4$)

3.7.2 Case at $U_\infty = 4.2786$ [m/s] ($Re \sim 2.9 \cdot 10^4$)

- Time Mean Pressure Coefficient (\bar{c}_p)

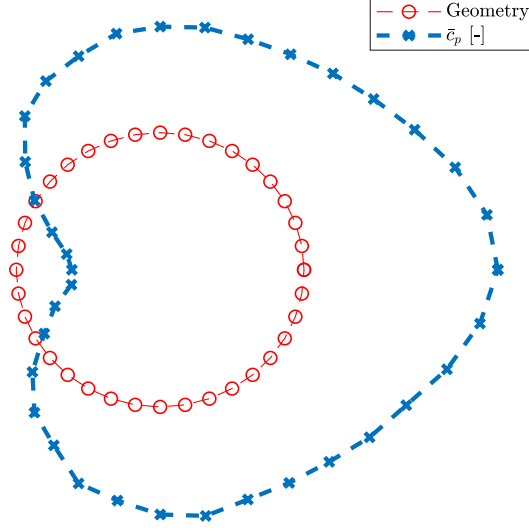


Figure 27: Time mean distribution of the pressure coefficient (\bar{c}_p) over the mid-span section of the moving cylinder at $U_\infty = 4.2786$ [m/s] ($Re \sim 2.9 \cdot 10^4$). Plotted over the geometry of the circular section

Figure 27 and Figure 28 present the time mean distribution of the 2D pressure loading of the cylinder at the mid-span section at $U_\infty = 4.2786$ [m/s] ($Re \sim 2.9 \cdot 10^4$). The former shows \bar{c}_p distribution plotted over the circular section that characterizes the geometry of the cylinder. It can be observed that compared to the case at $U_\infty = 1.4839$ [m/s] ($Re \sim 1 \cdot 10^4$) the aerodynamic loading over the cylinder is more symmetric with respect to the upper and lower parts of it. The latter shows \bar{c}_p as a function of the angular coordinate φ (Figure 28a) and as a function of the streamwise coordinate x (Figure 28b). Both verify the close to symmetric distribution of the 2D loading on the cylinder which can be the result of the 1D motion of the cylinder due to VIV. This way the structural motion takes under control the vortex shedding and makes the phenomenon predominantly two dimensional.

Compared to the time mean pressure coefficient distribution over the cylinder at $Re \sim 1 \cdot 10^4$ (Figure 23), the current \bar{c}_p presents a non constant distribution at the rare of the cylinder (see Figure 28). The possible cause of it is the separation of the flow followed by a re-attachment. Hence, the flow possibly separates from the cylinder at $x \sim 0.01$ [m] (or $\varphi \sim 78$ [°] & $\varphi \sim 282$ [°]), it keeps separated along the flattest part of the distribution and reattaches at $x \sim 0.02$ [m] (or $\varphi \sim 55$ [°] & $\varphi \sim 305$ [°]) leading the descend of \bar{c}_p value at the rear.

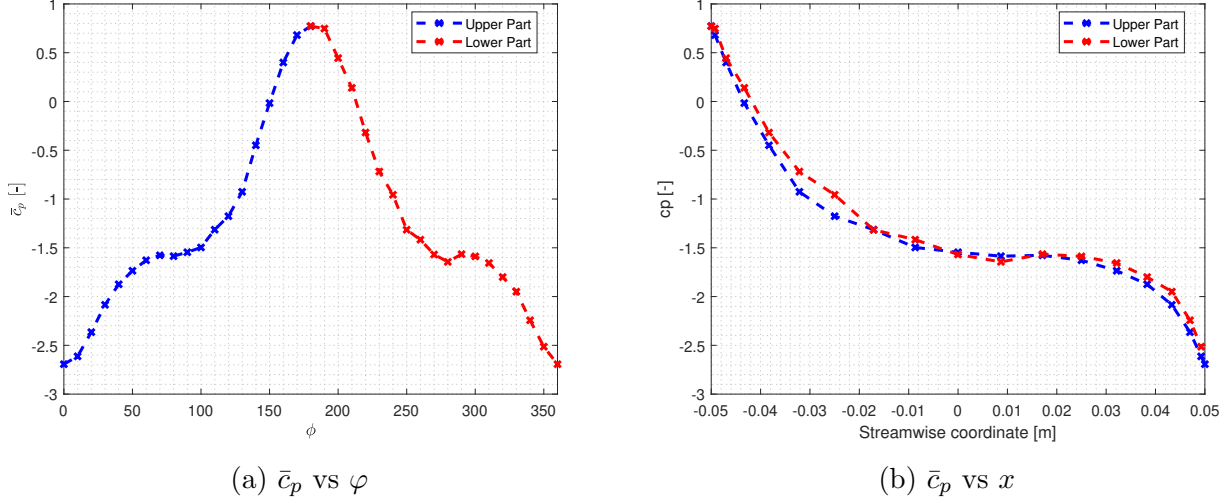


Figure 28: Time mean loading of the cylinder at $U_\infty = 4.2786$ [m/s] ($Re \sim 2.9 \cdot 10^4$). \bar{c}_p as a function of the angle ϕ (left). Where, ϕ is the angle defined in Figure 17a positive in the increasing direction of the numbering of the pressure taps. \bar{c}_p as a function of the streamwise coordinate x (right)

- **Time Evolution of Lift Coefficient ($c_{L_{exp}}$) and Drag Coefficient ($c_{D_{exp}}$)**

Figure 29 shows the time evolution of the 2D lift (Figure 29a) and drag (Figure 29b) coefficients computed directly from experimentally recorded c_p at mid-span section defined in subsection A.5. A FFT of the former is presented in Figure 31b. Compared to Figure 24b the oscillating frequency of $c_{L_{exp}}$ is more defined when the cylinder undergoes VIV, vibrating at its natural frequency and higher harmonics of it. Moreover, the leakage to contiguous frequencies has reduced. Table 5 captures the parameters that characterizes the behaviour of these aerodynamic parameters.

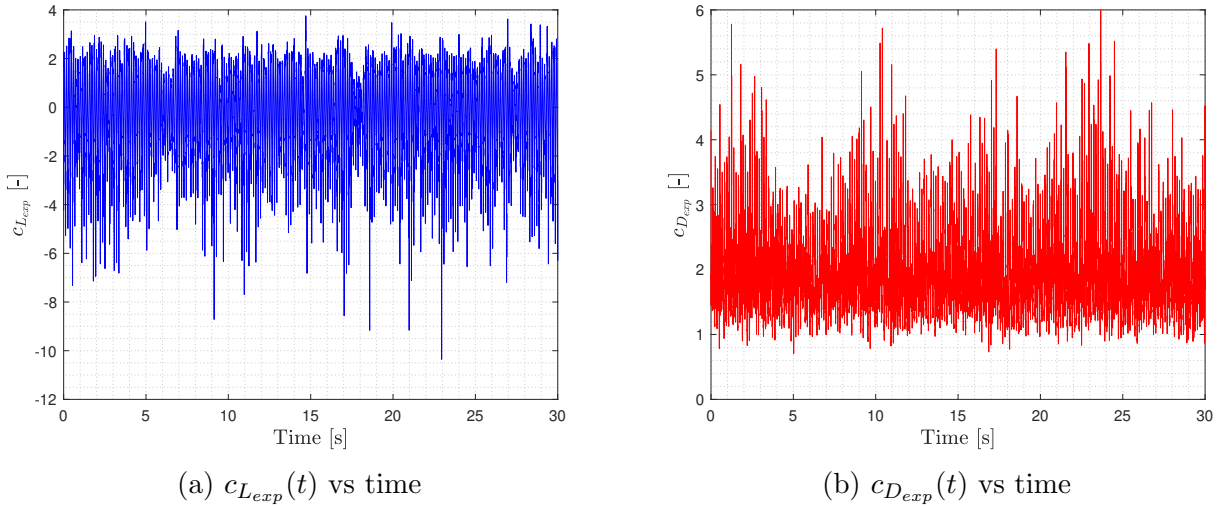


Figure 29: 2D lift (left) and drag (right) coefficients at mid-span section of the cylinder obtained from the experimental data at $U_\infty = 4.2786$ [m/s] ($Re \sim 2.9 \cdot 10^4$)

\bar{c}_{Lexp} [-]	\bar{c}_{Dexp} [-]	f_{cLexp} [Hz]
-0.2391	1.8399	7.07

Table 5: Time mean values of lift and drag coefficients computed from the experimental pressure distribution over the moving cylinder at mid-span section at $U_\infty = 4.2786$ [m/s] ($Re \sim 2.9 \cdot 10^4$). Main frequency of the time distribution of experimental lift coefficient

• Wake Velocity

On the one hand, Figure 30 show the time distribution of the velocity components in the wake recorded by the Cobra Probe. The streamwise component (u) is one order of magnitude greater than the others (v and w). Even more, the v component is close to be null, which can lead to the possibility to neglect 3D numerical simulations due to the dimensional behaviour of the vortex shedding phenomenon in the moving cylinder. However, this must be proven in the numerical simulations subsection 6.10.

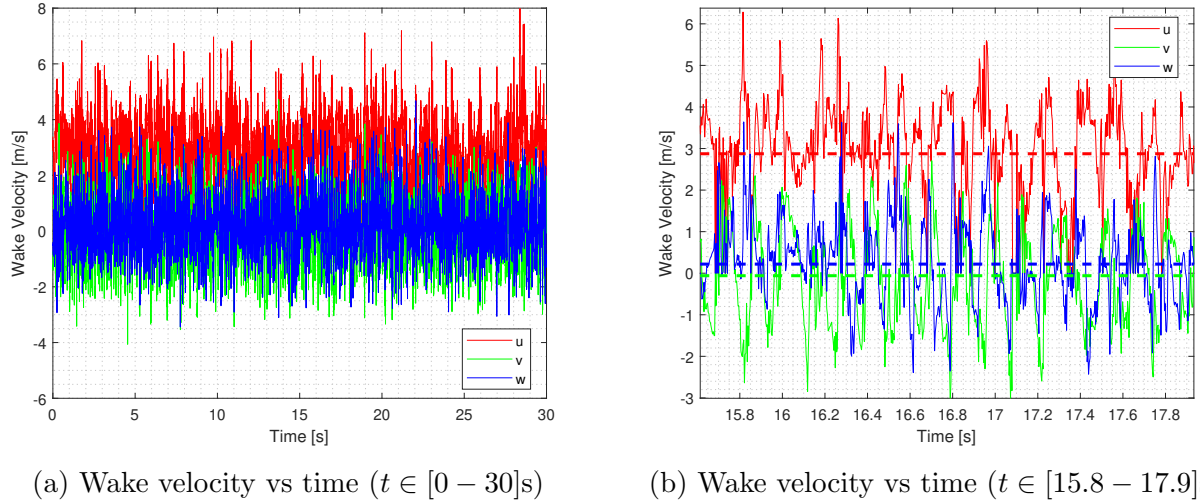
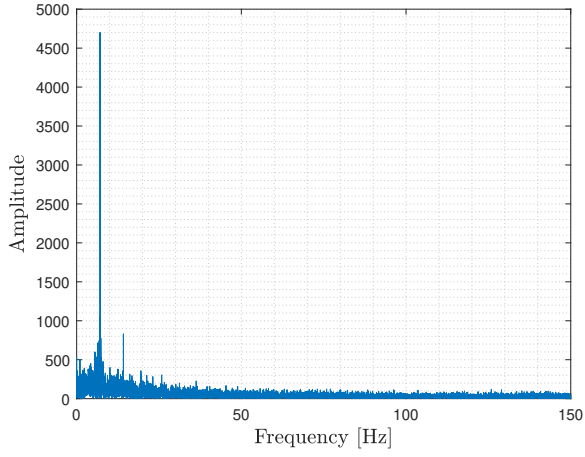


Figure 30: Time distribution of the wake velocity recorded by the Cobra Probe at $U_\infty = 4.2786$ [m/s] ($Re \sim 2.9 \cdot 10^4$). Streamwise component (u), spanwise component (w), orthogonal component to the others (v). See Figure 17b

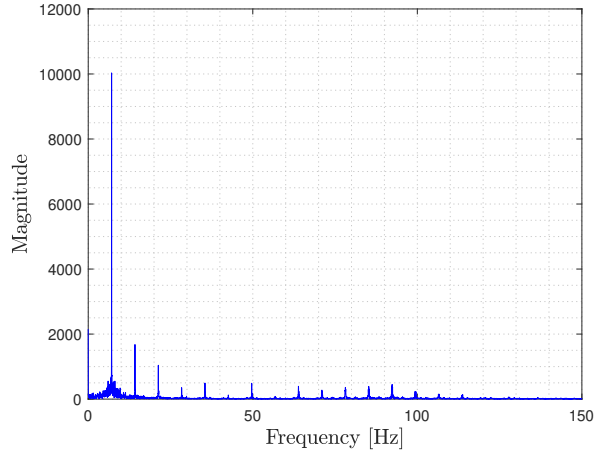
On the other hand, the FFT analysis of the wake velocity (Figure 31a) revealed a vortex shedding frequency of $f_{vs} = 7.07$ [Hz], which is the natural frequency of the cylinder (subsubsection 3.6.1).

\bar{u} [m/s]	\bar{v} [m/s]	\bar{w} [m/s]	f_{vs} [Hz]
2.8741	-0.0603	0.2190	7.07

Table 6: Time mean value of each wake velocity component and oscillation frequency of the lift coefficient at $U_\infty = 4.2786$ [m/s] ($Re \sim 2.9 \cdot 10^4$).



(a) FFT of the Wake Velocity



(b) FFT of c_{Lexp}

Figure 31: FFT of the experimental time signals of the lift coefficient (right) and wake velocity (left) at $U_\infty = 4.2786$ [m/s] ($Re \sim 2.9 \cdot 10^4$)

4 CFD Code Validation: 2D Static Cylinder

4.1 Introduction

Aiming to build an eventual numerical (CFD) model that captures the flow and its structural physics over both static and moving cylinders, a sequential procedure will be followed in the present report. Beginning from the simplest and computationally cheapest model until 2D dynamic models.

In the current section, a 2D numerical model of the static set-up will be developed and validated against the experimental data ($Re \sim 1 \cdot 10^4$) presented in subsubsection 3.7.1. As it will be shown later on, no 2D domain will be able to well-represent the experimental results obtained from the wind-tunnel, but this method allows to select turbulence models, element type and the mid-span sectional domain that will be used in 3D simulations while saving a great amount of computational cost and time. Eventually, the decisions taken in the current section will be considered and applied in 3D static and 2D dynamic numerical domains.

An early 2D simulation allows the user to make a higher mesh refinement of a fluid section at low computational cost than in 3D computations. This will give an idea of the effect of mesh refinement in terms of 2D effects. However, possible 3D effects of the wake and turbulent structures are automatically neglected losing possible information within the wake, as discussed by several authors [37] [32].

4.2 Computational Domain

Figure 32 shows the 2D computational domain used in both static and moving cylinder cases. It has been built based on the work of various authors in literature [59] [55] [48] [45] [43]. It is a rectangular fluid domain which extends up to 7.5D in y direction on both sides of the cylinder. This size coincides with the width of the wind tunnel (subsection 3.2). It also extends 8D upstream of the cylinder. Finally, the outlet is set at a distance of 22D downstream of it in order to well-capture the wake and its time dependent physics. It is essential for modelling the time evolution of the pressure distribution around the cylinder [59] [30] [55]. The wake is defined in a separated region from the main stream that allows a further refinement of it as it can be seen in Figure 32 & Figure 35. The two dimensional section will be also used as the span-wise extruded section of the 3D domain.

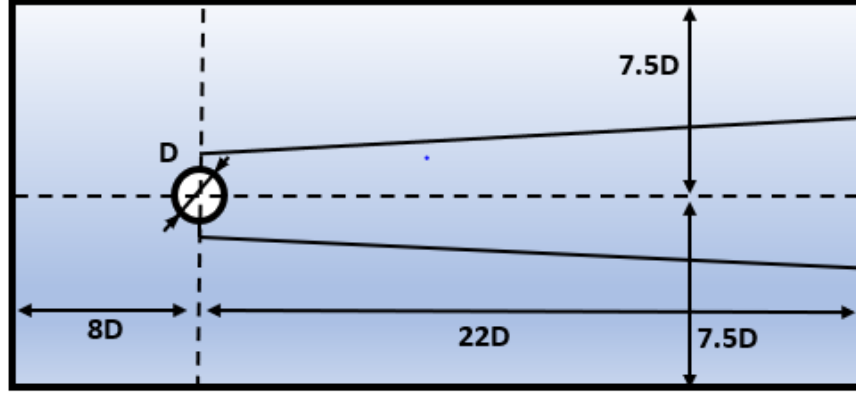


Figure 32: Geometry of the two dimensional fluid domain used in ANSYS Fluent

4.3 Numerical Grid and Mesh Independence Study

Based on the literature research of numerical simulations of flow around circular cylinders ([31] [40] [59] [55] [63] [64]...), it has been decided to go for an unstructured mesh of tetrahedral elements (Figure 35).

However, as it will be explained later on subsection 4.9, structured meshes (Figure 36) have been also tested in the turbulence model selection process. Moreover, each turbulence model has its own mesh requirements, mainly y^+ value and number of elements within the boundary layer, which will modify the final grid. Hence, the final size of the mesh, as well as the refinement level of the wake or the base size of the elements, will vary from one simulation to another. The mesh independence or convergence analysis will be first focused on steady state simulations and then, moved on into transient simulations. This study has been carried out by means of a parametric study in ANSYS Workbench combining ANSYS Design Modeler, ANSYS meshing and ANSYS Fluent commercial softwares.

4.3.1 Steady Parameters

20 computational grids of different refinement level have been compared. The eventual mesh will be selected based on the values of the lift and drag coefficients (c_L & c_D), the spatial averaged pressure coefficient on the cylinder wall ($Ave. c_p$), spatial averaged outlet flow velocity (u_{out}) and spatial averaged outlet mass flow rate (\dot{m}_{out}). The modifications amongst the different meshes have been introduced in:

- Number of discrete points on the cylinder boundary
- First cell height on the cylinder boundary
- Number of cells in the boundary layer
- Base element size on the wake and free-stream regions
- Growth rates in the boundary layer, free-stream and wake regions

Figure 33 & Figure 34 show the results from the parametric study as a function of the number of mesh elements. The study has been conducted for RANS Transition SST and RANS $k-\omega$ SST turbulence models (these two models, in their SAS versions, will result in the most successful ones in subsection 4.9). While c_L and u_{out} suffer barely variation with the refinement level (Figure 34a & Figure 34b), a greater evolution can be identified in c_D and Ave. c_p (Figure 33a & Figure 33b). A stable value of the latter parameters is reached with the numerical grid compounded by 83966 elements. Eventually, Table 7 and Table 8 summarize the conducted convergence study of the steady state parameters and presents the numerical values of those parameters for 5 meshes with different levels of refinement.

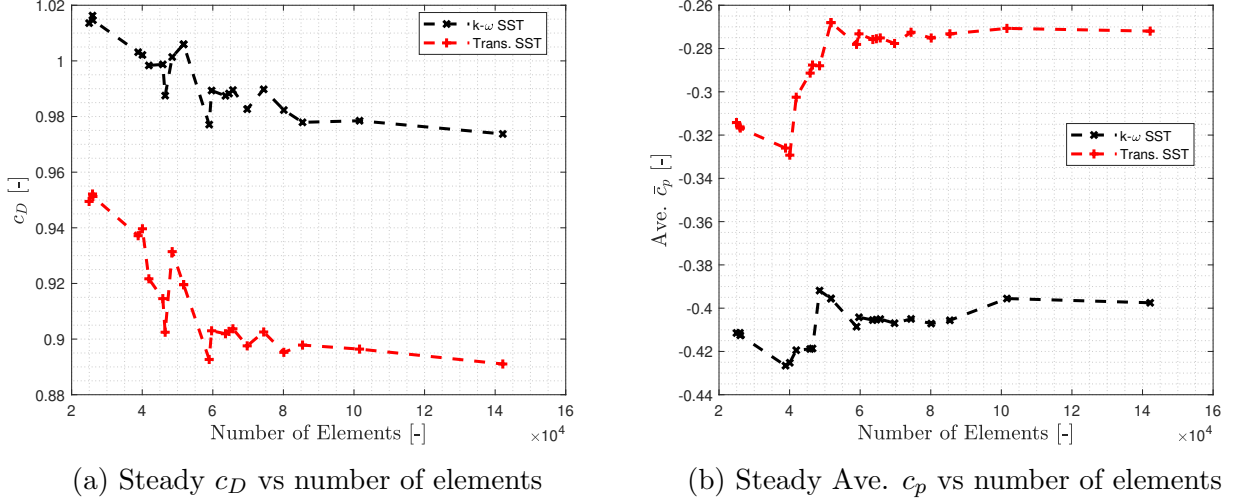


Figure 33: Evolution of c_D (left) and spatial average of c_p on the cylinder (right) for increasing values of number of cells on the grid. RANS Transition SST (red) and RANS $k-\omega$ SST (black) turbulent models have been analyzed at $Re \sim 1 \cdot 10^4$

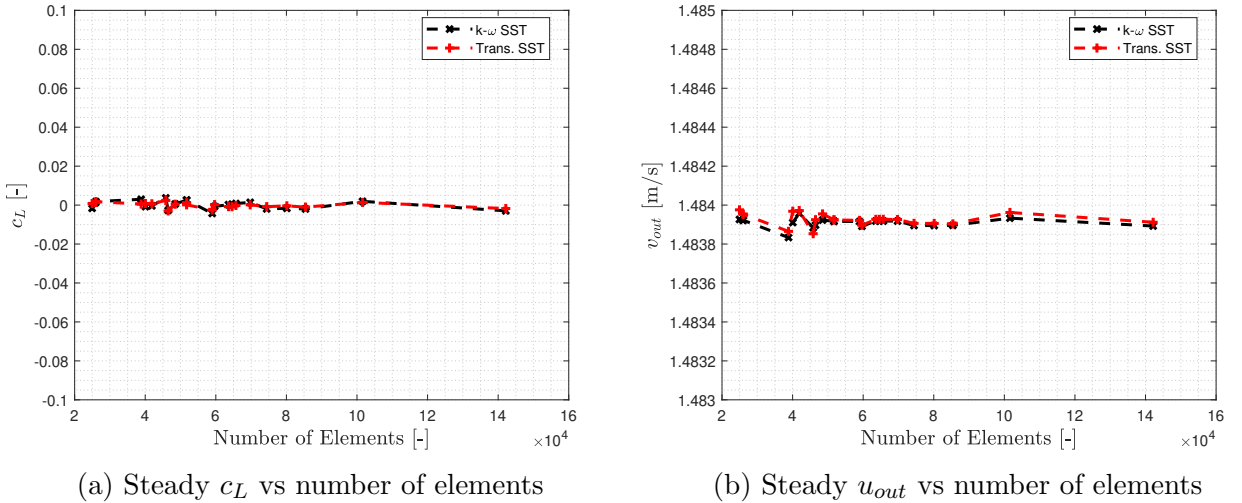


Figure 34: Evolution of c_L (left) and u_{out} (right) for increasing values of number of cells on the grid. RANS Transition SST (red) and RANS $k-\omega$ SST (black) turbulent models at $Re \sim 1 \cdot 10^4$

# Elements [-]	c_L [-]	c_D [-]	Ave. c_p [-]	u_{out} [m/s]	\dot{m}_{out} [kg/s]
26026	0.00213	0.7424	-0.3161	1.2787	8.38605
46497	-0.00271	0.747	-0.2482	1.2787	8.38605
83966	-0.0011	0.0749	-0.2379	1.2786	8.38605
101576	0.001332	0.7507	-0.2368	1.2788	8.38605
142164	-0.0029	0.7443	-0.2343	1.2786	8.38605

Table 7: Steady parameters used in the mesh independence study of 2D static numerical code with RANS $k - \omega$ SST turbulence model at $Re \sim 1 \cdot 10^4$

# Elements [-]	c_L [-]	c_D [-]	Ave. c_p [-]	u_{out} [m/s]	\dot{m}_{out} [kg/s]
26026	0.002603	0.8588	-0.3493	1.2787	8.38605
46497	0.00639	0.8164	-0.3682	1.2786	8.38605
83966	-0.00381	0.822	-0.3561	1.2786	8.38605
101576	0.001332	0.8217	-0.348	1.2787	8.38605
142164	0.0005236	0.8163	-0.3511	1.2786	8.38605

Table 8: Steady parameters used in the mesh independence study of 2D static numerical code with Transition SST Turbulence model at RANS $Re \sim 1 \cdot 10^4$

4.3.2 Time Dependent Parameters

From the previous presented grids, the transient analysis has been applied to the finest ones. Consequently, the coarsest mesh is the one at which the steady convergence has been reached, resulting in a comparison of 3 levels of refinement. The results are presented in Table 9 (SAS $k - \omega$ SST) & Table 10 (SAS Transition SST) which show that the convergence of the time dependent parameters is reached for the same mesh as for the steady state simulations. As mentioned before, these two turbulence models will result in the most successful ones (subsection 4.9). Even if the computational time of each simulation is not reflected in the tables, moving from the coarsest to the finest, it increases by orders of magnitude.

# Elements [-]	\bar{c}_L [-]	\bar{c}_D [-]	Ave. \bar{c}_p [-]	\bar{u}_{out} [m/s]	\bar{m}_{out} [kg/s]
83966	0.0737	1.8233	-0.9393	1.4850	2.91
101576	0.0168	1.783	-0.9178	1.4849	2.91
142164	0.01579	1.7814	-0.9189	1.4849	2.91

Table 9: Time dependent parameters used in the mesh independence study of 2D static numerical code with SAS $k - \omega$ SST turbulence model at $Re \sim 1 \cdot 10^4$. \bar{c}_L , time mean value of 2D lift coefficient; \bar{c}_D , time mean value of 2D drag coefficient; Ave. \bar{c}_p , spatial average of the time mean pressure coefficient over the cylinder; \bar{u}_{out} , area average of the time mean value of velocity at outlet boundary; \bar{m}_{out} , time mean value of the mass flow rate at outlet boundary

# Elements [-]	\bar{c}_L [-]	\bar{c}_D [-]	Ave. \bar{c}_p [-]	\bar{u}_{out} [m/s]	\bar{m}_{out} [kg/s]
83966	0.0768	1.6791	-0.8731	1.4840	2.908
101576	0.0720	1.669	-0.8590	1.4840	2.908
142164	0.012	1.716	-0.8588	1.4839	2.908

Table 10: Time dependent parameters used in the mesh independence study of 2D static numerical code with Transition SAS SST turbulence model at $Re \sim 1 \cdot 10^4$. \bar{c}_L , time mean value of 2D lift coefficient; \bar{c}_D , time mean value of 2D drag coefficient; Ave. \bar{c}_p , spatial average of the time mean pressure coefficient over the cylinder; \bar{u}_{out} , area average of the time mean value of velocity at outlet boundary; \bar{m}_{out} , time mean value of the mass flow rate at outlet boundary

4.3.3 Results and Conclusions

Eventually, the validated mesh is shown in Figure 35. It is composed by 83966 elements and 65691 nodes. The base element size of the main stream region is 0.2 [m]. The wake region, however, has been refined down to a base element size of 0.05 [m] with a growth rate of 1.05. The inflation layer around the cylinder has 20 layers and the height of the first cell is $5 \cdot 10^{-5}$ [m] which results in $y+ < 1$. These parameters are within the range of recommendations done by authors on the literature ([59] [26] [73]) to well-resolve the flow around the cylinder with SAS-SST and SAS Trans. SST turbulence models. These turbulence models will result in the most successful ones in subsection 4.9.

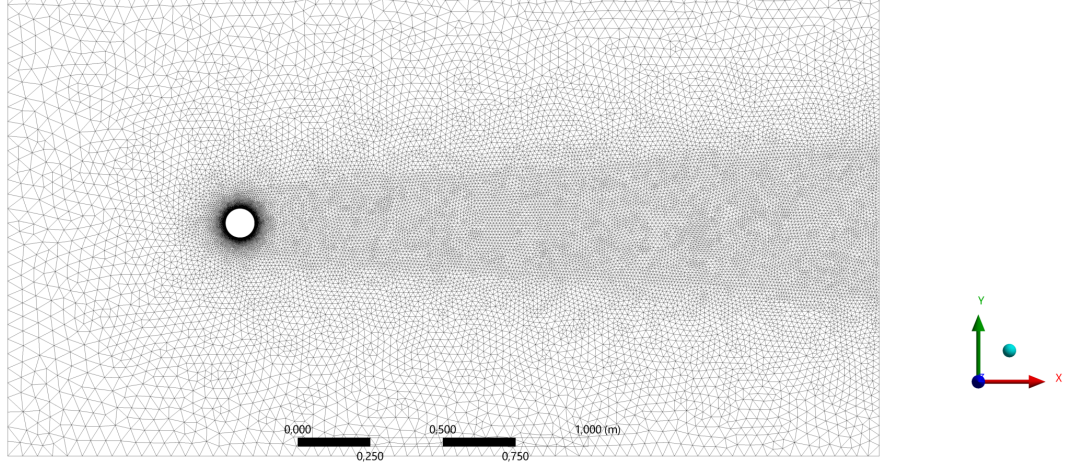
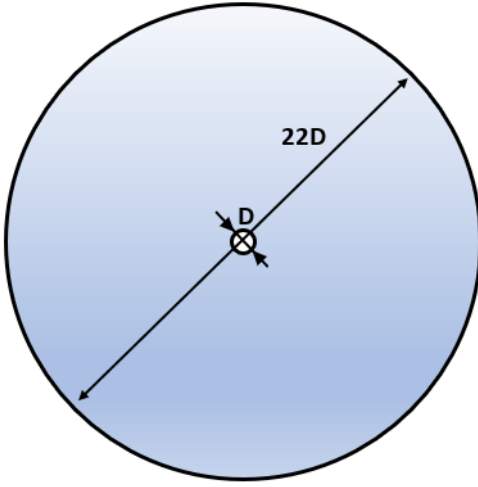


Figure 35: Validated bidimensional unstructured grid

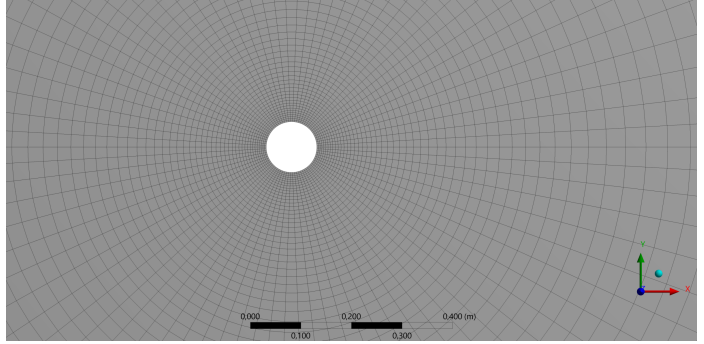
Final mesh information:

- **Number of Nodes:** 65691
- **Number of Elements:** 83966
- **Minimum Face Angle:** 20.20 [°]
- **Maximum Face Angle:** 125.945 [°]
- **First Cell Height in Inflation Layer:** 0.00005 [m]

- **Number of Cells in Inflation Layer:** 20
- **Cell Growth Rate in Inflation Layer:** 1.1
- **Base Element Size in Free-stream region:** 0.2 [m]
- **Cell Growth Rate in Free-stream region:** 1.1
- **Base Element Size in wake region:** 0.05 [m]
- **Cell Growth Rate in wake region:** 1.05



(a) 2D Circular domain



(b) Rectangular section of the 2D structured grid

Figure 36: 2D circular domain and structured grid used in the turbulence model selection process (subsection 4.9)

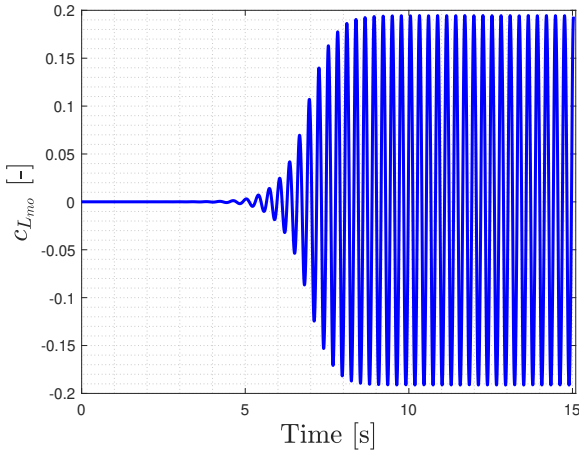
4.4 Boundary Conditions

- **Inlet Boundary:** It has been defined as a velocity inlet boundary. The velocity magnitude equals the experimental one ($u_{inlet} = 1.4839$ [m/s]) and the direction, normal to the boundary. The turbulence intensity is 0.2% (experimental). Eventually, the static pressure is set equal to the atmospheric $p_{inlet} = p_{atm} = 101325$ [Pa]
- **Outlet Boundary:** It has been defined as pressure outlet which has been set equal to the atmospheric $p_{inlet} = p_{atm} = 101325$ [Pa]. The turbulence level of the reverse flow has been set equal to the inlet turbulence (0.2%).
- **Cylinder wall Boundary:** No-slipping wall boundary
- **Upper & Lower Boundaries:** As there is no interest in the resolution of the boundary layer that evolves on the walls of the wind tunnel, 3 different boundary types were tested (symmetry, no-slip wall and slipping wall). As these boundaries are far enough from the cylinder and the aerodynamic blockage that the cylinder introduces in the wind tunnel is really small, no big difference was observed in the loading over the cylinder. The main

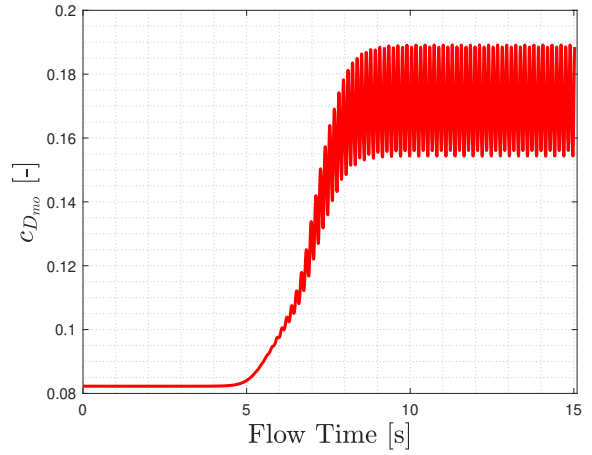
discrepancies were found in the static pressure and velocity close to these boundaries and the convergence of the numerical scheme. Both of them depend on the resolution or not of the boundary layer on the walls of the tunnel which is not of interest of the current report. Eventually, symmetry conditions were applied as the steps taken until convergence and the order of magnitude of the residuals were the lowest.

4.5 Convergence Criteria

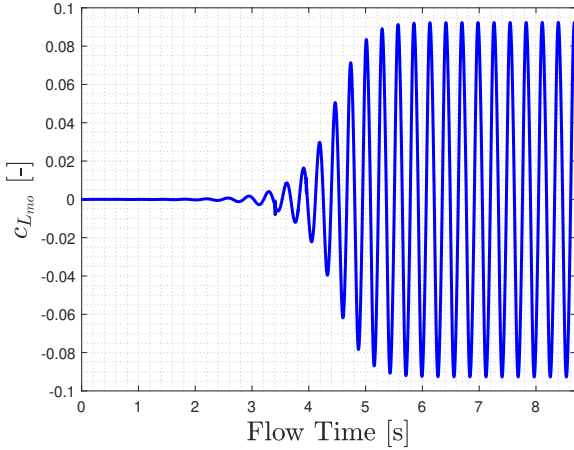
The convergence of the numerical scheme for transient simulations will be mainly based in the time distribution of lift and drag coefficients automatically monitored by ANSYS Fluent (see subsection A.3 for definition) as advised in [73].



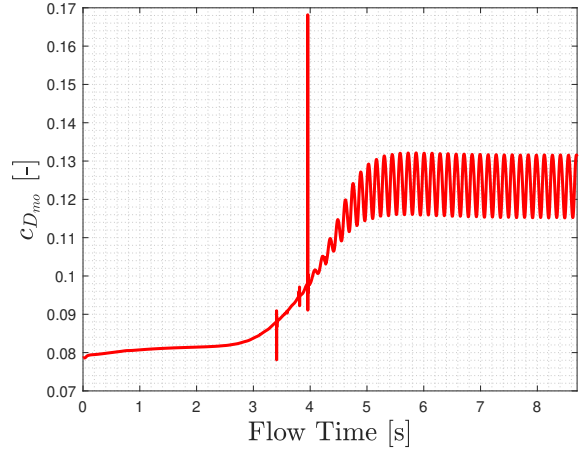
(a) URANS $k - \omega$ SST: $c_{L_{mo}}$



(b) URANS $k - \omega$ SST: $c_{D_{mo}}$



(c) RSM $k - \epsilon$: $c_{L_{mo}}$



(d) RSM $k - \epsilon$: $c_{D_{mo}}$

Figure 37: Time evolution of $c_{D_{mo}}$ and $c_{L_{mo}}$ until convergence has been reached. These results correspond to URANS $k - \omega$ SST and RSM $k - \epsilon$ turbulence models used in subsection 4.9

From different authors in literature ([44] [9] [67] [22] [7]) it is known that the the lift acting on the cylinder oscillates with the main frequency (or close to it) of vortex shedding process. The

drag, instead, at the double of it. Hence, the simulation will have converged when $c_{L_{mo}}$ and $c_{D_{mo}}$ start oscillating with a sinusoidal shape at constant amplitude and defined frequency.

By definition, $c_{L_{mo}}$ and $c_{D_{mo}}$ will converge to a perfect sinusoidal time signal in URANS/RANS turbulence models. In hybrid models (SAS, DES, DDES, IDDES), however, it will contain more than only one frequency content. Further discussion can be found in subsubsection 6.10.1. Figure 37 shows two examples of converged simulations used in subsection 4.9. As it can be seen the convergence of the results is reached at different flow times depending on the numerical code used.

4.6 Discretization and Solution Schemes

Second order implicit temporal discretization is used with a time step of $\Delta t = 0.005$ s (see subsection 4.7) and 20 iterations per time step to ensure the convergence at each time step. In the CFD codes based on URANS turbulence models, Second order Implicit temporal discretization is adopted.

However, due to convergence issues when running SAS turbulence models it has been switched to Wall-Bounded Second Order Implicit scheme. By recommendation of ANSYS Fluent manual [73] the residuals should decrease at least in 2 orders of magnitude in each time step.

For steady state simulations, COUPLE solver has been used for the pressure-velocity coupling while for transient simulations, SIMPLE¹ is set following the trend of several authors in literature. Second Order Upwind spatial discretization has been used for the transport equations introduced by the turbulence models to close the problem (Turbulent Kinetic Energy, Specific Dissipation Rate, Intermittency and momentum Thickness Re...). Furthermore, second order spatial discretization has been applied in the pressure field and least Squares Cell Based discretization for the gradient. Eventually, momentum equation has been spatially discretized by means of central differencing in URANS models and Bounded Central differencing in SAS models.

4.7 Time Step Size

In this section a convergence analysis of the time mean values will be carried out in order to set the optimum time step size of the numerical integration scheme. The optimal Δt will be the one that provides a balance between the computational cost of the simulation and the accuracy of the results (same philosophy that was used in the mesh independence analysis). The results are summarized in Table 11. It can be deduced that the results obtained with $\Delta t = 0.001$ [s] and $\Delta t = 0.005$ [s] are nearly identical and slightly different compared to the ones from $\Delta t = 0.0005$ [s]. However, the increase of the simulation time from the smallest time step to the intermediate one is considerable. Hence, aiming a balance between the accuracy and the computational cost it was decided to set a time step of $\Delta t = 0.005$ [s].

¹A brief introduction to the basics of SIMPLE and PISO algorithms for pressure-velocity coupling solving can be found in Appendix B

Δt [s]	\bar{c}_L [-]	\bar{c}_D [-]	Ave. \bar{c}_p [-]	\bar{u}_{out} [m/s]	\bar{m}_{out} [kg/s]
0.01	0.0053	1.43	-0.3192	1.4839	2.9084
0.005	0.0086	1.66	-0.8378	1.4838	2.9082
0.001	0.0080	1.68	-0.8341	1.4838	2.9080
0.0005	0.0081	1.682	-0.8268	1.4838	2.9080

Table 11: Time step size Δt convergence analysis for the 2D static cylinder CFD code at $Re \sim 1 \cdot 10^4$

As there is no deformation of the mesh, nor dynamic properties of it has been used, no huge differences on the results can be found when setting a small enough time step. This kind of analysis will be of essential importance in the moving cylinder code (subsection 6.3) as the mesh is deformed at each time step and a big enough Δt could result in a sudden divergence of the code.

4.8 Running Procedure

The running procedure, as recommended in ANSYS Fluent tutorial [73] and widely used by authors of the field, is based on sequential steps. Each step will consist in one simulation; being the first one the cheapest and simplest one computationally speaking and in increasing order of complexity. The objective of this approach is to help the CFD code converge and avoid possible divergence or excessive computational time. Steps to follow:

1. **Steady State simulation:** Convergence is verified when the steady aerodynamic coefficients (c_L and c_D) reach a steady value and the residuals lay below 10^{-12} or reach a low steady value. Reynolds Averaged Navier-Stokes (RANS) turbulence models ($k - \omega$ or Transition SST) are used in this first step. The chosen one will be applied to the different simulations in its different versions (URANS & SAS). Also, at this point the $y+$ values are checked.
2. **First Transient simulation:** The initial conditions will be the converged steady solution. At this point, Unsteady Reynolds Averaged Navier-Stokes (URANS) turbulence models are used. The convergence criteria is defined in subsection 4.5.
3. **Second Transient simulation:** Once the transient solution of the URANS turbulence model has converged. It is ran one more time (URANS $k - \omega$ SST or URANS Trans. SST depending on the initial choice) during a number of time steps which makes possible the correct extraction of time dependent parameters and statistics.
4. **Third Transient simulation:** From the converged transient results the turbulence model is modified from URANS to SAS and ran until convergence is reached. Also, by recommendation of ANSYS manual [73], the time scheme is changed from 2^{nd} order implicit to bounded 2^{nd} order implicit.
5. **Forth Transient simulation:** Once the transient solution with SAS turbulence model has converged, it is ran one more time with the same turbulence model (SAS $k - \omega$ SST or SAS Trans. SST) during a number of time steps which makes possible the correct extraction of time dependent parameters and statistics.

4.9 Turbulence Model Selection

The main objective of this section is to select a turbulence model capable of capturing the physical behaviour of the flow in both boundary layer and the near wake region after the separation. Based on an extensive literature research (subsection 2.1), it has been concluded that high fidelity turbulence models as LES should be avoided in terms of grid resolution and computational cost. Furthermore, they are 3D turbulence models by definition and should not be used in 2D computations. Conversely, RANS or URANS turbulence models would be the computationally cheapest option but they fail to well-represent the 3D behaviour of the turbulent wake. Hence, the optimum choice would be an Hybrid LES/RANS model as DES or SAS. Aiming to avoid further refinement of the wake in the 3D domain, which introduces a massive computational cost, it was desired to use SAS rather than DES. Moreover, it has been proven in the literature ([59] [26]) that the former successes modelling the 3D behaviour of the turbulent wake. Eventually, the following turbulence models have been tested:

- URANS $k - \varepsilon$
- URANS $k - \omega$ SST
- URANS Transition SST
- RSM $k - \varepsilon$
- SAS SST $k - \omega$
- SAS Transition SST

	$k - \omega$ SST	Trans. SST	RSM $k - \varepsilon$	SAS SST	SAS Trans. SST	Wind Tunnel
f_{sv}^o [Hz]	3.6374	3.1862	3.5398	3.1705	2.7951	2.7731
St [-]	0.2451	0.2147	0.2385	0.2137	0.1884	0.1869

Table 12: Strouhal number (St) and shedding frequency (f_{vs}) obtained from 2D unstructured mesh simulations at $Re \sim 1 \cdot 10^4$

Aiming to save computational cost and time, the ability of several URANS models have been compared in the 2D domain and their ability to capture the shedding frequency (f_{vs}). The shedding frequency has been extracted from the oscillatory behaviour of the monitored lift coefficient, $c_{L_{mo}}$ (see subsection A.3) in ANSYS Fluent once the results were stabilized. Table 12 shows the results obtained from this study.

Furthermore, as it is presented in Figure 38, independently of the turbulence model, none of them is able to represent \bar{c}_p distribution over the static cylinder after the separation of the boundary layer happens. Aiming to avoid too much information on the plot and keep it understandable, just the closest turbulence models to the experimental data have been represented. This difference is even greater in the near-wake region of the cylinder, where all the turbulence models present a tendency to more negative values whereas the experimental data does not. Hence, several structured meshes (Figure 36a & Figure 36b) have also been tested as an attempt to find the cause of that behaviour. However, as presented in Table 13 that would not be the

problem and the resultant shedding frequencies are further away from the experimental results. Eventually, it has been concluded that it would be due to the fact that 3D effects are not captured by the developed numerical models.

	URANS $k - \varepsilon$	URANS $k - \omega$ SST	URANS Trans. SST	Wind Tunnel
f_{sv} [Hz]	3.9346	3.7037	3.367	2.7731
St [-]	0.2652	0.2496	0.2269	0.1869

Table 13: Strouhal number (St) and shedding frequency (f_{vs}) obtained from 2D structured mesh simulations at $Re \sim 1 \cdot 10^4$

Based on the results presented in Table 12 and Table 13, two turbulence models have been selected in both versions (URANS & SAS) for further analysis. On the one hand, $k - \omega$ SST, as the original SAS was developed with it; and the Transitional SST turbulence model (it gives the closest results to experimental data). Both of them using the unstructured mesh with tetrahedral elements presented in Figure 35.

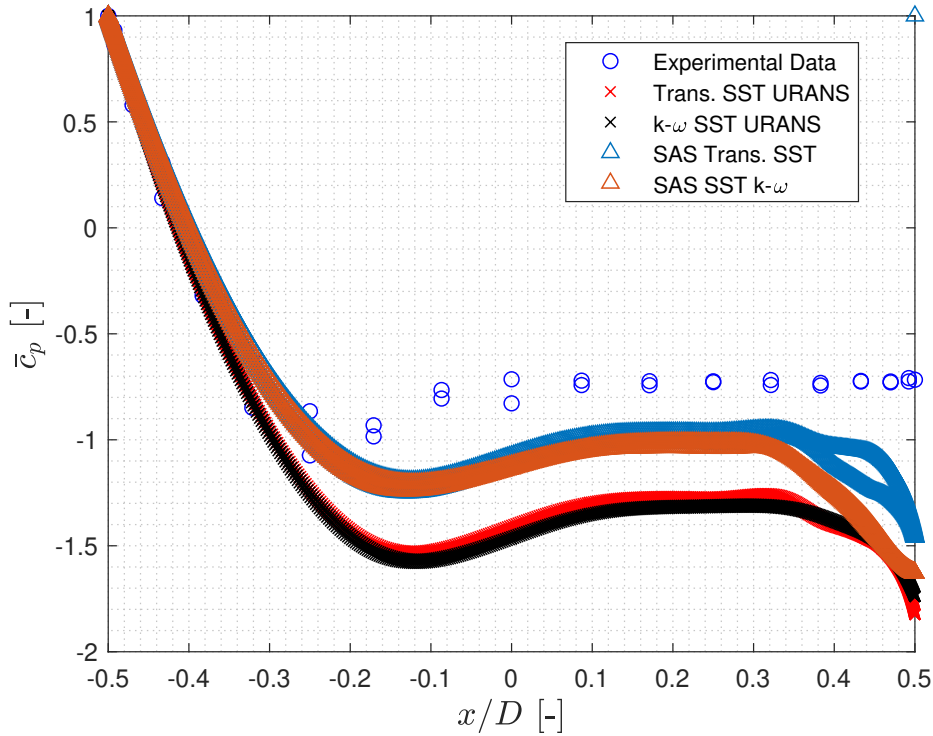


Figure 38: Time mean distribution of the pressure coefficient over the static cylinder at $U_\infty = 1.4839$ [m/s] ($Re \sim 1 \cdot 10^4$). Comparison between experimental and numerical data. X, URANS models; \triangle , SAS models; \bigcirc , Experimental data

4.10 Conclusions

After having done the corresponding mesh independence study and the convergence testing of the parameters related to the numerical schemes, it has been concluded that independently of

the turbulence model implemented in the CFD code, none of them is able to well-represent and capture the inherent unsteadiness of the wake region and vortex shedding process from the bluff body. However, the fluid physics over the region of the cylinder where the flow is attached seem to be captured. Furthermore, the Scale Adaptive turbulence models behave in a conciser way rather than URANS models. This result was expected as E. Palkin and R. Mullyadzhhanov & M. Hadziabdic [63], P.R. Spalart [37] and Ju-Yeol You & Joon Kwon [55] discussed in their previous researches in the field.

Even if the results from the previous CFD codes have not been successful enough in modelling the inherent 3D and unsteady nature of the wake after bluff bodies, the numerical domain and grid will be used as the starting point for the 3D simulations (section 5) and 2D oscillating cylinder (section 6). The validation of the computational codes will be more strict in the following sections as this approach aimed to build a first numerical domain and have a first insight of the capabilities of the different turbulence models implemented on the commercial software.

5 CFD Code Validation: 3D Static Cylinder

5.1 Introduction

Based on the results obtained in section 4 the bidimensional model will be extended into a 3D computational domain. The objective is to capture the main flow physics that the 2D simulations failed to do. Inherently, the extension of the fluid domain ($2D \rightarrow 3D$) will increase the computational cost and simulation time.

First, aiming to keep it as low as possible a new mesh independence study will be performed. The 2D mesh can not be used as reference as it does not converge to correct solutions with a refining process (subsection 4.9).

Secondly, two different turbulence models will be compared and validated against the data obtained from the wind tunnel. These models are $k - \omega$ SST and Transition SST in both forms, SAS and URANS. On the one hand, the former is the original model used in SAS; the latter, however, gave the best results in two dimensional simulations (subsection 4.9).

The , running procedure, convergence criteria, time step size and numerical schemes used in this section will be identical to the ones used in section 4. Also, the validation parameters.

5.2 Computational Domain

Figure 32 will be used as the base 2D section of the fluid domain and it will be extruded in spanwise direction. The modelling of the whole physical test section of the wind tunnel would have increased drastically the computational cost of the simulations due to the span-wise discretization needed to well-capture the 3D effects of the fluid in the wake region. Hence, based on the results presented by various authors who worked in transient computational simulations of flow around 3D static cylinders ([59] [55] [31]) the span-wise length of the three-dimensional domain will be $L = \pi D$. The previous value should be big enough to well-represent the three dimensional flow-physics within a infinite cylinder. The main concern at this point was that, due to the flow conditions under which the experiment was performed in the wind tunnel (end wall effects, non perfect circular section, surface roughness of the cylinder...), the mid-span section is not independent of the boundary conditions at the ends of the cylinder. Hence, this could produce discrepancies between the 2D loading of the cylinder at mid-span section for a infinite (numerical) and finite (experimental) cylinder.

5.3 Grid and Mesh Independence Study

On the one hand, as shown and discussed in Figure 38 and subsection 4.9 even a excessive refinement of the 2D mesh (nor structured or unstructured) does not successfully represent the experimental data extracted at mid-span section of the cylinder. However, in terms of vortex shedding frequency and loading it resulted that the unstructured grids behave better than the structured ones. Hence, based on those results, a new mesh independence study of unstructured 3D meshes of tetrahedral elements has been performed.

On the other hand, the main concern of the mesh was the refinement level in spanwise direction and the ability of the grid to well-capture the 3D effects of the turbulent wake in spanwise-direction (it is thought that the 2D model failed due to the later reason). Several authors ([59] [55] [31]) compared different number of elements in which the span of the cylinder was divided ($N_z = 5$, $N_z = 15$, $N_z = 20$, $N_z = 30$) from which the last two resulted in successful attempts. Eventually, $N_z = 24$ was set due to mesh quality criteria. At this point, 3 numerical grids of different refinement level (coarse, medium and fine) have been compared. The properties of these three meshes are presented in Table 14.

Mesh	# Nodes	# Elements	# Tetrahedrals	# Wedges
Coarse	173345	507417	280617	226800
Medium	293827	845857	445857	4000
Fine	1036360	4409004	3689004	720000

Table 14: Number of nodes and elements of the 3 different three dimensional meshes analyzed in the convergence study at $Re \sim 1 \cdot 10^4$

Following the procedure used in subsection 4.3 for 2D meshes, several parameters obtained from both steady state simulations and transient simulations have been compared and exposed in Table 15. It can be deduced that there is no a big difference between the resultant values of the three grids. Hence, aiming a balance between the efficiency and accuracy of the eventual CFD code the medium mesh has been selected.

# Mesh [-]	c_L [-]	c_D [-]	\bar{c}_L	\bar{c}_D	Ave. c_p [-]	m_{out} [kg/s]	u_{out} [m/s]
Coarse	0.000122	0.7207	-0.0021	1.030	-0.3612	0.8236	1.4840
Medium	0.0035	0.8244	-0.00201	1.025	-0.3489	0.8236	1.4840
Fine	0.0089	0.8465	-0.001905	1.021	-0.3296	0.8235	1.4839

Table 15: Steady and time dependent parameters used in the mesh independence study of 3D static numerical code with SAS $k - \omega$ SST turbulence model at $Re \sim 1 \cdot 10^4$

The main properties of the eventual mesh are listed below:

- **Number of Nodes:** 293827
- **Number of Elements:** 845857
- **First Cell Height in Inflation Layer:** 0.00005 [m]
- **Number of Cells in Inflation Layer:** 20
- **Cell Growth Rate in Inflation Layer:** 1.2
- **Base Element Size in Free-stream region:** 0.2 [m]
- **Cell Growth Rate in Free-stream region:** 1.2
- **Base Element Size in wake region:** 0.1 [m]
- **Cell Growth Rate in wake region:** 1.1

5.4 Boundary Conditions

Regarding inlet, outlet, cylinder wall and upper and lower boundaries, the imposed conditions and values are identical to the ones used in the bidimensional domain (described in subsection 4.4). However, when switching from 2D to 3D domain, two new boundaries arise. These last ones, represent the "physical walls" of the wind tunnel on which the support of the cylinder is set. As mentioned in subsection 5.2, the first try has been to model an infinite cylinder from a non-infinite one. Hence, periodic boundary conditions have been set as done by several authors ([59] [55] [31]). Obviously, this technique will introduce some drawbacks in the model such as the 3D effects that the separation of the boundary layer of the wind tunnel wall due to the presence of the cylinder will be neglected. These phenomena are called end-wall effects (some examples of them are horse-shoe vortices or high angle oblique shedding). In turbomachinery field, they are a concern as they introduce a decrease in total pressure which is translated in losses or loss of efficiency. In contrary, the resolution of them implies the resolution of the boundary layer in this boundaries and consequent refinement of the mesh. Hence, as they are not concern of the current project, and low computational effort is desirable, the decision taken has been going for the modelling of the infinite 3D cylinder.

5.5 Simulation Procedure & Set-Up

Basically, the running procedure is the same as the one used in 2D simulations and explained in subsection 4.8. Regarding the numerical set-up, is also very similar to the one explained in subsection 4.6. The main properties are listed below:

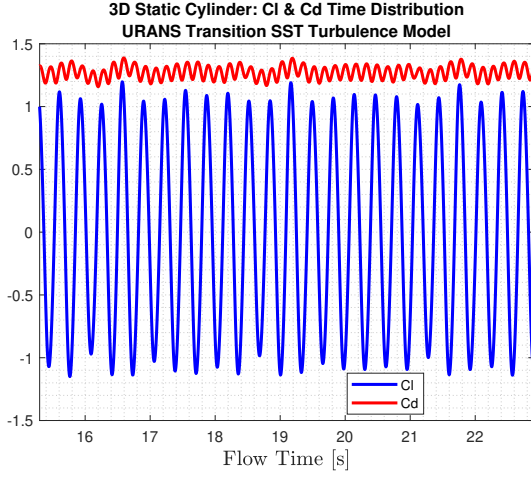
- COUPLE Solver for the pressure-velocity coupling of steady state simulations
- Second Order Implicit temporal discretization with URANS turbulence models in transient simulations
- Wall-Bounded Second Order Implicit temporal discretization with SAS turbulence models
- Second Order Central Differencing for the spatial discretization of the momentum equation (URANS)
- Bounded Second Order Central Differencing for the spatial discretization of the momentum equation (SAS)
- SIMPLE(Appendix B) scheme for velocity-pressure coupling
- Second Order Upwind spatial discretization in the transport equations of Turbulent Kinetic Energy, Specific Dissipation Rate, Intermittency and momentum Thickness Re

5.6 Results and Validation

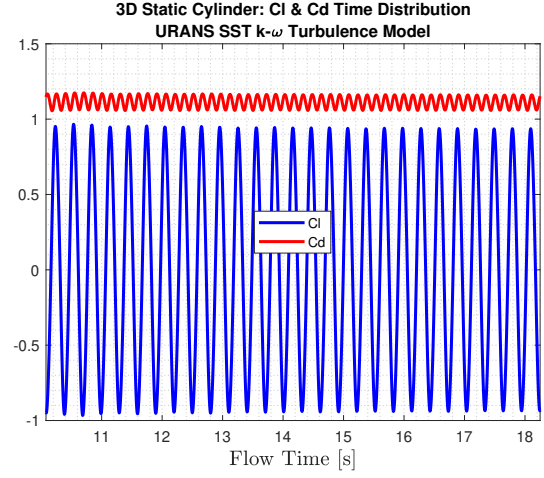
5.6.1 Lift and Drag Coefficients

The monitored 3D aerodynamic coefficients ($C_{L_{mo}}$, $C_{D_{mo}}$) cannot not be compared to the ones obtained from the wind tunnel ($c_{L_{exp}}$, $c_{D_{exp}}$) if one is consistent with their definitions presented

in subsection A.3 and subsection A.5. Two are the reasons:

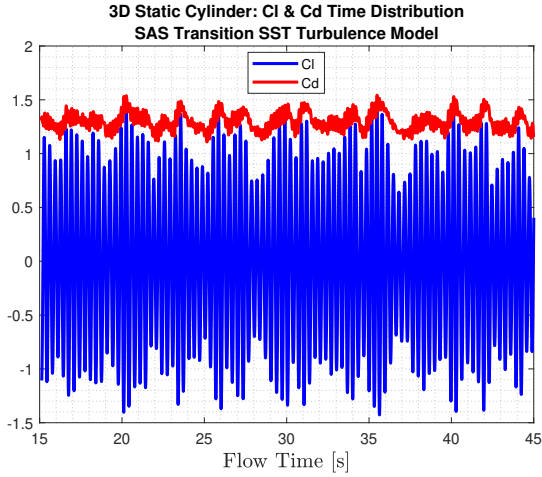


(a) $C_L(t)$ & $C_D(t)$

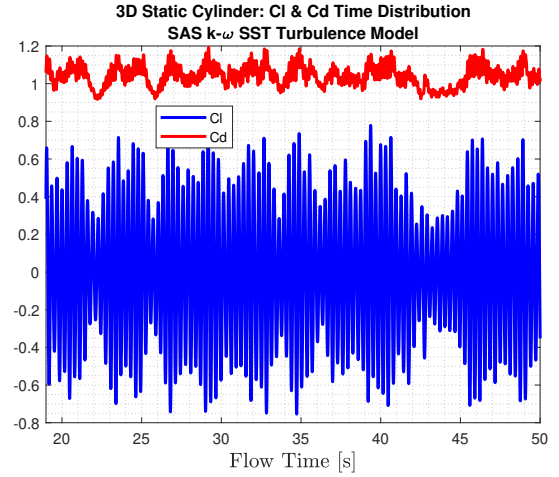


(b) $C_L(t)$ & $C_D(t)$

Figure 39: $C_L(t)$ & $C_D(t)$ Time distribution of the 3D static cylinder at $U_\infty = 1.4839$ [m/s] ($Re \sim 1 \cdot 10^4$). URANS Transition SST Turbulence model (left). URANS $k-\omega$ SST turbulence model (right)



(a) $C_L(t)$ & $C_D(t)$



(b) $C_L(t)$ & $C_D(t)$

Figure 40: $C_L(t)$ & $C_D(t)$ Time distribution of the 3D static cylinder at $U_\infty = 1.4839$ [m/s] ($Re \sim 1 \cdot 10^4$). SAS Transition SST Turbulence model (left). SAS $k-\omega$ SST turbulence model (right)

- We do not have information about the shear stress component from the experimental data
- ANSYS Fluent uses the whole cylinder pressure and shear stress distribution over the cylinder which varies over the span of the cylinder (3D aerodynamic distribution). However, the experimental data consists only of the pressure distribution at mid-span section (2D aerodynamic distribution) and if one wants to extend it to the whole cylinder, homogeneous span distribution will be assumed which it is not as verified by several authors [37] [30] [59].

Instead, $C_{D_{ma}}$ (subsection A.6) will be used which allows to validate the data with the well-known "Drag Crisis Curve for Circular Cylinders" (Figure 6) presented and discussed in section 2.

On the one hand, as discussed in subsection 4.5 the time distribution of the monitored lift and drag coefficients of URANS turbulence models resulted in sinusoidal time distributions with a main frequency. The SAS turbulence models, however, present time signals with a wider frequency content. As discussed by Ju-Yeol You & Oh Joon Kwon in [55] URANS turbulence models are more dissipative than SAS model which results in a 2D regular vortex shedding for the former and 3D irregular for the latter. This behaviour is translated in the $C_L(t)$ and $C_D(t)$ time distributions given by the software and presented in Figure 39 and Figure 40.

On the other hand, the time mean value of the aerodynamic parameters obtained from the different CFD codes are presented in Table 16. The $C_{L_{ma}}$ in all of them has really low values and close to the theoretical (null). The different $C_{D_{ma}}$ values, even of being of the same magnitude, varies more, being the one obtained from SAS $k - \omega$ SST turbulence model really close experimental values presented in the drag-crisis curve (Figure 6).

	URANS $k - \omega$ SST	URANS Trans. SST	SAS $k - \omega$ SST	SAS Trans. SST
$\bar{C}_{L_{ma}}$ [-]	-0.0025	0.0045	-0.0021	0.0043
$\bar{C}_{D_{ma}}$ [-]	1.1137	1.2728	1.0453	1.3016

Table 16: Comparison of the 3D time mean lift and drag coefficients monitored in ANSYS Fluent at $Re \sim 1 \cdot 10^4$

5.6.2 Shedding Frequency & Strouhal Number

Table 17 compares the vortex shedding frequencies and the Strouhal numbers obtained in each numerical simulation performed in the validation of the CFD code for the static 3D cylinder at $Re \sim 1 \cdot 10^4$. It has been extracted from the oscillatory behaviour of $C_{L_{mo}}$ by means of Fast Fourier Transform (FFT) of the time signal.

First, analysing the results, they are slightly higher than expected considering the 2D simulations or wind-tunnel data ($f_{vs} = 2.77$ [Hz]). However, they are closer to the experimental and numerical values presented and widely validated in literature (Figure 3). The generic value of $St = 0.2$ is extended for perfectly circular 3D cylinders. A possible reason for this could be that while the aforementioned results are two-dimensional (affected or not by 3D effects and of geometric imperfections or not) and the last ones take into consideration the whole span of the cylinder and the possible presence of asymmetries and 3D effects due to turbulence, non-symmetric vortex

shedding or geometric defects.

Secondly, the numerical code that results in the closest shedding frequency to the experimental one is the one that has implemented the SAS Transition SST turbulence model on it.

	URANS $k - \omega$ SST	URANS Trans. SST	SAS $k - \omega$ SST	SAS Trans. SST
f_{vs} [Hz]	3.31	3.09	3.12	3.03
St [-]	0.22	0.21	0.21	0.20

Table 17: Vortex shedding frequency (f_{vs}) and Strouhal (St) values extracted from the time evolution of $C_{L_{mo}}$ and $C_{D_{mo}}$ of the numerical 3D simulation at $Re \sim 1 \cdot 10^4$

5.6.3 Time Mean 3D Loading

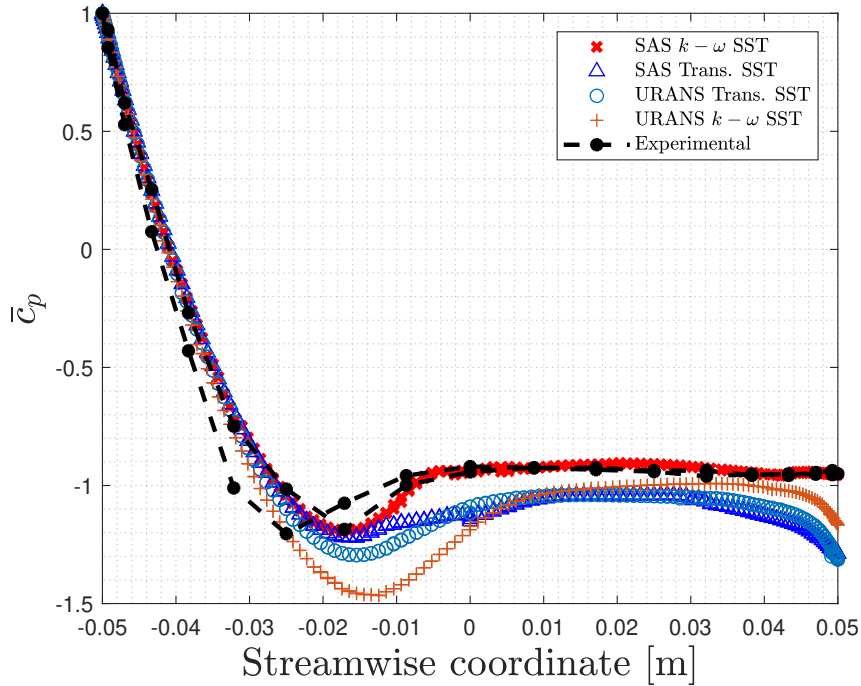


Figure 41: Comparison of \bar{c}_p distribution over the mid-span section of the static cylinder at $U_\infty = 1.4839$ [m/s] ($Re \sim 1 \cdot 10^4$) extracted from 3D simulations. Experimental data is also included

Figure 41 presents the time mean pressure coefficient (\bar{c}_p) at mid-span value obtained from the 4 different CFD codes plotted over the experimental distribution extracted from the wind-tunnel. The only simulation that well-represents the experimental time mean c_p distribution is the SAS $k - \omega$ SST turbulence model. However, the profile obtained numerically is nearly symmetric compared to the experimental data which behaves in a more unsymmetrical way. This was expected mainly due to the fact that the cylinder used in the wind tunnel would not probably be perfectly circular and as shown in Figure 20 the amplitude of the motion is not exactly null. It is also affected by the roughness of the cylinder. It is remarkable that the four turbulence

models result in nearly the same \bar{c}_p distribution along the attached flow conditions and follow the distribution of one half of the experimental cylinder. URANS models present a latter separation point of the flow compared to the SAS models which are closer to the experimental values.

5.7 Conclusions

The eventual validated 3D numerical code will consist of the medium refinement level grid presented in subsection 5.3 which main properties are summarized and listed below:

- **Number of Nodes:** 293827
- **Number of Elements:** 845857
- **First Cell Height in Inflation Layer:** 0.00005 [m]
- **Number of Cells in Inflation Layer:** 20
- **Base Element Size in Free-stream region:** 0.2 [m]
- **Base Element Size in wake region:** 0.1 [m]
- **Number of Elements in span:** 24

and boundary conditions:

- Velocity Inlet
- Pressure Outlet
- Upper and Lower No-slipping Wall
- No-slipping wall on the cylinder
- 2 Symmetry Boundaries to model an infinite 3D cylinder

Regarding the numerical methods, wall-bounded second order implicit temporal discretization has been used for the transient simulation with a time step of 0.005 [s]. Momentum equation has been spatially discretized with bounded second order central differencing and SIMPLE solver has been applied to the velocity-pressure coupling. Finally, a second order upwind scheme has been applied to the spatial discretization of the transport equations of the turbulence models.

Even if the SAS Transition SST turbulence model results in a closer vortex shedding frequency, SAS $k - \omega$ SST model has been defined as the most successful one. The latter, as shown in Figure 41 and Figure 6, showed the closest agreement with the experimental data extracted from the wind tunnel in terms of the mean loading on the cylinder as well as with the widely validated drag crisis curve.

6 CFD Code Validation: 2D Moving Cylinder

6.1 Introduction

As the final step of computational validation, a 2D dynamic model will be developed. The results from the numerical domain will be compared to the data extracted from the run test number 11 which corresponds to the case at which the cylinder undergoes VIV with the largest amplitude. Testing conditions are listed below:

- Windspeed: $U_\infty = 4.2786$ [m/s]
- $Re = 2.91 \cdot 10^4$ [-]
- Natural Frequency: $f_n = 7.07$ [Hz]
- Amplitude: $|y| = 0.038$ [m]

The CFD code used for the static cylinder case will be the starting point for an eventual computational model for the resolution of the flow around an oscillating cylinder. Hence, the base fluid domain, turbulence models and mesh size will be the same. In contrary, the numerical domain will depend on time (imposed motion of the cylinder and the mesh needs to adapt accordingly). Hence, an independent and more exhaustive time integration analysis will be carried out with respect to the previous cases. Special attention needs to be paid to the time step size and the adaptation of the mesh around the moving boundaries.

Eventually, a CFD code will be chosen to be used for further study in section 7.

6.2 Computational Domain and Boundary Conditions

The two dimensional computational domain used to model the moving cylinder is presented in Figure 32 which is the one built in subsection 4.2 for the static cylinder. Regarding boundary conditions, same have been imposed:

- Inlet Velocity Boundary Condition
- Pressure Outlet Boundary Condition
- No-Slipping Wall Boundary Condition at the Cylinder
- Symmetry Boundary Conditions in the upper and lower boundaries

However, two main differences arise at this point; first, the inlet velocity magnitude normal to the boundary is $u_{inlet} = 4.2786$ [m/s] (with same incoming turbulence level $Ti = 0.2\%$) and the cylinder boundary is a moving wall. The objective of the previous modification is to model the oscillatory motion of the cylinder undergoing VIV.

In order to do so, a pure sinusoidal movement transverse to the incoming flow have been imposed to the region of the fluid domain that models the cylinder walls. This motion is characterized by an amplitude of $|y| = 0.038$ [m] and a frequency equal to the natural frequency of the structure

($f_n = 7.07$ [Hz]). The last parameters were extracted from the experimental data and characterize the motion of the cylinder undergoing VIV. It is done by introducing a User Defined Function (UDF) in ANSYS Fluent with the velocity of the center of gravity that it is desired to impose to the moving boundary (Equation 3). The reason of imposing velocity and not displacement is that there is only that option in the software.

$$y(t) = |y| \sin(2\pi \cdot f_n \cdot t) \quad [m] \quad \longrightarrow \quad \dot{y}(t) = 2\pi \cdot f_n \cdot |y| \cos(2\pi \cdot f_n \cdot t) \quad [m/s] \quad (3)$$

6.3 Mesh and its Dynamic Properties

The base mesh applied in the dynamic simulations is identical to the one presented and validated for the static case in subsection 4.3. However, due to the time dependent shape of the domain (motion of the cylinder wall), the mesh needs to adapt to the motion of the cylinder boundary while the other boundaries stay still.

The updating of the volume mesh will be done by the so called "Smoothing Method". The mesh will be adjusted by the motion of the interior nodes but keeping the number of them and their connectivity unmodified. Hence, *"the interior nodes absorb the movement of the boundary"* [73]. The previous adaptation can be done in several ways (Diffusion based, spring based, laplacian or linearly Elastic Solid based smoothing), however, the so call "Diffusion" was selected for its simplicity.

Basically, the mesh motion is governed by the diffusion equation [73]:

$$\nabla \cdot (\gamma \nabla \vec{u}) = 0 \quad ; \quad \gamma = \frac{1}{d^\alpha} \quad (4)$$

where,

- \vec{u} is the mesh displacement velocity
- γ is the diffusion coefficient based on the normalized boundary distance (d)
- $\alpha \geq 0$ is the diffusion parameter which will be the user input parameter
- d is the normalized distance to the nearest wall boundary

The software allows the user to control the diffusion of the boundary motion by means of α . High values of it preserves the mesh quality close to the boundary and the motion will be mainly absorbed by cells away from it. A null value, instead, results in a homogeneous diffusion of the motion through the complete mesh. Eventually, a value of $\alpha = 1$ was set by try and error procedure based on the recommendations done in ANSYS Fluent Manual [73].

The position of the nodes are updated by means of a finite element discretization and Equation 5.

$$\vec{x}_{n+1} = \vec{x}_n + \vec{u} \Delta t \quad (5)$$

where,

- \vec{u} is computed at each node
- Δt is the time step size
- \vec{x}_{n+1} is the new node location
- \vec{x}_n is the old node location

Equation 4 is also solved using finite element discretization.

Moreover, the software gives the possibility to apply remeshing at each time step to avoid possible cell degeneration when the displacement is large compared to the local cell size. This could result in negative cell volume or convergence problems. At each time step the software computes the skewness and size criteria of each element, if any of them falls out of the established criteria ([73]), it updates the mesh locally in order to fix the mesh quality problem. However, the previous procedure makes the CFD code lose second order of accuracy in time integration. The last statement is specially interesting for hybrid turbulence models, as ANSYS Fluent manual [73] recommends to use them with "Second Order Implicit Wall Bounded" time integration due to stability and convergence issues. However, both cases (with and without remeshing) were tested and no significant differences were found in the obtained results.

6.4 Discretization and Solution Schemes

First order implicit temporal discretization is used in URANS turbulence models with a time step of $\Delta t = 0.001$ s (see subsection 6.6) and 30 iterations per time step (see subsection 6.8) to ensure the convergence at each time step. Then, it has been switched to second order implicit scheme for SAS models. By recommendation of ANSYS Fluent manual [73] the residuals should decrease at least in 2 orders of magnitude in each time step. For the steady results COUPLE solver has been used for the pressure-velocity coupling. It is switched to SIMPLE for transient simulations.

Second Order Upwind spatial discretization has been used for the transport equations introduced by the turbulence models to close the problem (Turbulent Kinetic Energy, Specific Dissipation Rate, Intermittency and momentum Thickness Re). Furthermore, second order spatial discretization has been applied in the pressure field and least Squares Cell Based discretization for the gradient. Eventually, the momentum has been spatially discretized by means of central differencing in URANS models and Bounded Central differencing in SAS models.

6.5 Convergence Criteria

In addition to the time distribution of lift and drag coefficients automatically monitored by ANSYS Fluent (as it has been presented in subsection 4.5 for the static case) also the contours of the dynamic turbulent viscosity ratio (μ_t/μ) in the wake will be used. The shape of this last fluid property will show when the shape of the wake is fully developed. This is specially important in the case of the moving cylinder compare to the static one because in the transient simulation the aim is to move from a static set up into a well defined dynamic situation.

Furthermore, the behaviour of $c_L(t)$ and $c_D(t)$ time signals will vary depending on the fact that the cylinder lies within the lock-in region or not. If it does, the shape of the converged time signal

will be close to a pure sinusoidal signal as there is only one predominant shedding frequency. If the imposed motion results in being unlocked or lay near the unlocked-locked boundary, the frequency content will be wider and non sinusoidal shape (see subsection 7.3.1). It is the result of the combination of different frequencies (f_{vs} & f_{osc}).

6.6 Time Step Size

The time step size is a key parameter when dealing with dynamic meshes. Not only due to the fact that a too big time step could result in negative volume cells and consequent fatal error of the simulation. But, it can lead into converged but not correct results. The former error could be a consequence of big displacement of the moving boundary in the defined time step. Hence, the modification introduced in the fluid domain cannot be adapted by the mesh without violating the skewness and cell size criteria (minimum and maximum boundaries). The former errors are automatically found as the software is not able to run. The latter, however, the simulation runs smoothly but it converges to alternative values which are not correct. The only way to identify the correct time step size will be by performing several simulations with decreasing time step size until convergence of the results is found. The optimal size will be the one that provides accurate enough solution with the lowest computational cost (highest time step). In other words, a combination of efficiency and accuracy is desired.

Δt [s]	\bar{c}_L [-]	\bar{c}_D [-]	Ave. \bar{c}_p [-]	\bar{u}_{out} [m/s]	\bar{m}_{out} [kg/s]
0.01	0.0365	0.9072	-0.6664	4.2789	8.3860
0.005	0.0033	1.8199	-0.9835	4.2794	8.3860
0.001	-0.0029	1.624	-0.8465	4.2786	8.3861
0.0005	0.0012	1.604	-0.8327	4.2786	8.3861

Table 18: Time step convergence analysis for the CFD code of the oscillating cylinder based on the SAS Transition SST turbulence model at $Re \sim 2.9 \cdot 10^4$

Δt [s]	\bar{c}_L [-]	\bar{c}_D [-]	Ave. \bar{c}_p [-]	\bar{u}_{out} [m/s]	\bar{m}_{out} [kg/s]
0.01	-0.0026	1.4333	-0.8914	4.3263	8.3861
0.005	-0.06	1.5036	-0.8670	4.2798	8.3861
0.001	-0.0421	1.5701	-0.7874	4.2786	8.3861
0.0005	-0.0537	1.554	-0.7712	4.2786	8.3861

Table 19: Time step convergence analysis for the CFD code of the oscillating cylinder based on the SAS $k - \omega$ SST turbulence model at $Re \sim 2.9 \cdot 10^4$

On the one hand, Table 18 & Table 19 present the time step convergence analysis for SAS Transition SST and SAS $k - \omega$ SST turbulence models consequently (most successful ones in 2D static simulations). As performed in the mesh independence study (subsection 4.3), the time mean values of the lift (\bar{c}_L) and drag (\bar{c}_D) coefficients, spatial averaged pressure coefficient (Ave. \bar{c}_p), and velocity (\bar{u}_{out}) and mass flow rate (\bar{m}_{out}) at the outlet boundary have been analyzed for different time step sizes. In both cases, a good balance between accuracy and cost is obtained at $\Delta t = 0.001$ [s] as an adequate convergence of the values is obtained. A further decrease

of the time step would introduce a large increase of the computational time in each simulation which is not desired as a large amount of simulations will need to be performed during the report.

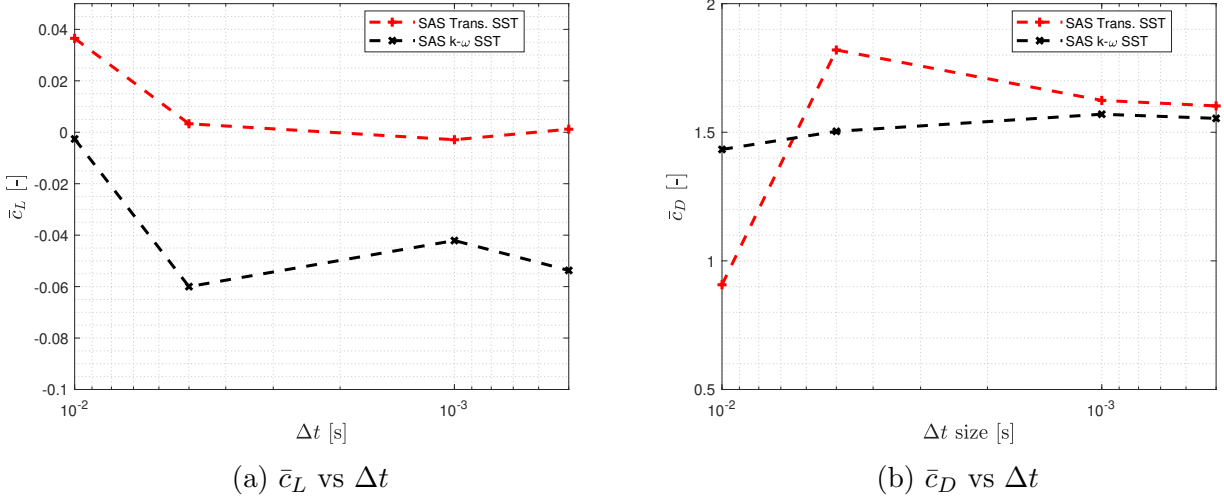


Figure 42: Time step size convergence study. Evolution of aerodynamic coefficients (\bar{c}_L & \bar{c}_D) on the moving cylinder for decreasing values of the time step, Δt , at $Re \sim 2.9 \cdot 10^4$

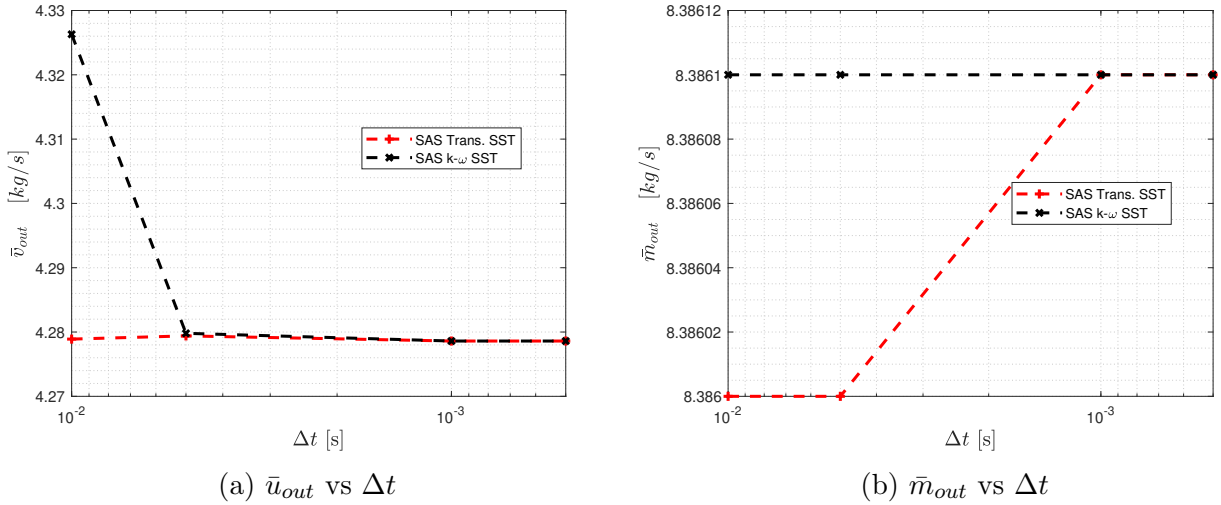


Figure 43: Time step size convergence study. Evolution of the time mean values of velocity (\bar{u}_{out}) and flow rate (\bar{m}_{out}) in the outlet boundary for decreasing values of the time step, Δt , at $Re \sim 2.9 \cdot 10^4$

On the other hand, Figure 45 & Figure 46 presents the ability to represent the wake pattern for decreasing values of the time step (Δt) used in the numerical scheme. The solutions have been obtained with URANS $k - \omega$ SST turbulence model. Whilst the greatest value nearly does not capture any vortex pattern (and being close to the resultant wake from an steady state simulation), the solutions from $\Delta t = 0.001$ [s] and $\Delta t = 0.0005$ [s] give relatively close results with a completely developed vortex shedding pattern of the wake. Hence, eventually, the time

step for numerical integration has been fixed to $\Delta t = 0.001$ [s] reaching a balanced CFD code between the accuracy of the results and the cost of the computational simulation.

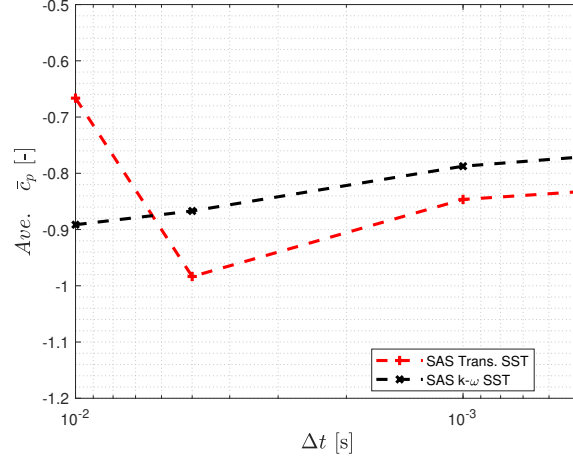


Figure 44: Spatial averaged \bar{c}_p over the oscillatory cylinder with $f_{osc} = 7.07$ [Hz] & $|y| = 0.038$ [m] as a function of Δt size at $Re \sim 2.9 \cdot 10^4$

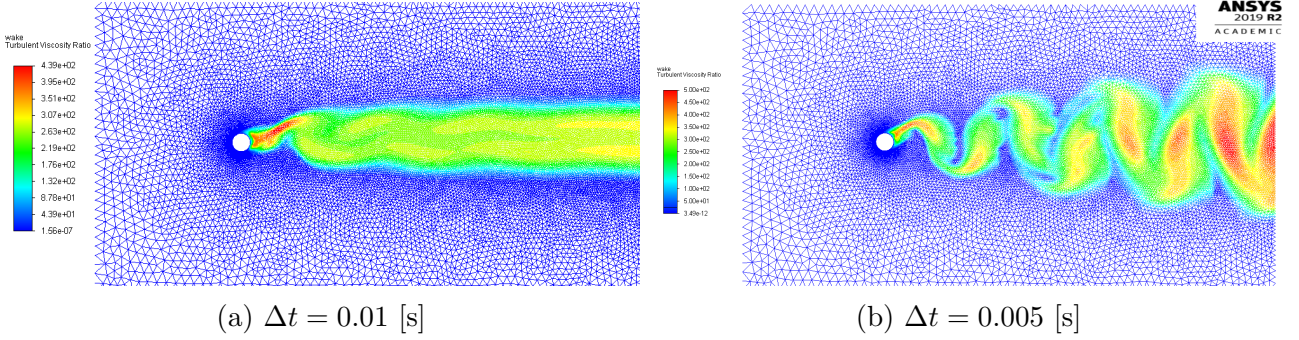


Figure 45: Wake Pattern convergence plotting μ_t/μ contours for the oscillating cylinder with $f_{osc} = 7.07$ [Hz] & $|y| = 0.038$ [m] at $Re \sim 2.9 \cdot 10^4$ for $\Delta t = 0.005$ [s] & $\Delta t = 0.01$ [s]

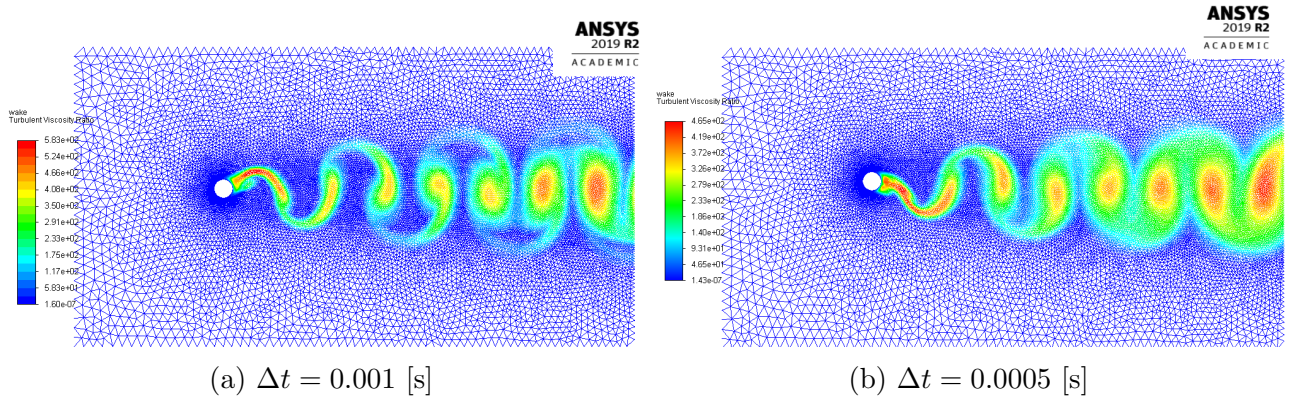


Figure 46: Wake pattern convergence plotting μ_t/μ for the oscillating cylinder with $f_{osc} = 7.07$ [Hz] & $|y| = 0.038$ [m] at $Re \sim 2.9 \cdot 10^4$ for $\Delta t = 0.001$ & $\Delta t = 0.0005$ [s]

6.7 Turbulence Model Selection

Based on the results obtained from the two dimensional static analysis (subsection 4.9) four turbulence models will be coded in the current dynamic simulation:

- URANS $k - \omega$ SST
- URANS Transition SST
- SAS $k - \omega$ SST
- SAS Transition SST

Remind that compared to the static cylinder case, the incoming windspeed has increased up to $U_\infty = 4.2786$ [m/s] ($Re \sim 2.9 \cdot 10^4$) and consequently will be at higher $y+$ values. Exactly, the maximum value is $y+ \sim 1.1$. As mentioned several times previously, a recommendation done by ANSYS Fluent Manual [73] is that for URANS and SAS $k - \omega$ SST turbulence model, it should be around 1, which is not a problem at all. However, URANS and SAS Transitional SST should be used at $y+ \leq 1$. Boundary layer refinement study has been conducted and no significant differences were found in terms of separation point and loading distribution. Eventually, it was decided to use the same mesh for both turbulence models. subsection 6.10 presents the discussion and comparison between the four turbulence models. SAS Transition SST turbulence model will result in the most successful one and will be used for the lock-in analysis on section 7 and section 8.

6.8 Number of Iterations per Time Step

Another numerical key parameter for the convergence of the results is the maximum number of iterations in each time step. As it happens with the time step size a balance between the accuracy of the results and the computational cost is desired. A greater number of iterations allows the CFD code to reach lower residuals down to the minimum (set by the user); however, it will notably increase the computational time of the simulation. Table 20 presents the results of the analysis. A good balance between accuracy and efficiency is acquired with 30 iterations per time step.

#Iterations [-]	\bar{c}_L [-]	\bar{c}_D [-]	Ave. \bar{c}_p [-]	\bar{v}_{out} [m/s]	\bar{m}_{out} [kg/s]
20	-0.0054	1.61	-0.7991	4.2784	8.3856
30	-0.0029	1.624	-0.8465	4.2786	8.3860
50	-0.0032	1.628	-0.8513	4.2786	8.3860

Table 20: Number of iterations per time step analysis for the CFD code of the moving cylinder under imposed motion of $f_{osc} = 7.07$ [Hz] & $|y| = 0.038$ [m] based on the SAS Transition SST turbulence model at $Re \sim 2.9 \cdot 10^4$

6.9 Running Procedure

The running procedure, as recommended in ANSYS Fluent [73] tutorial and done for the static case (subsection 4.8), is performed in sequential steps. Each step will consist in one simulation; being the first one the cheapest and simplest one computationally speaking and in increasing order of complexity. The objective of this approach is to help the CFD code converge and avoid possible divergence or excessive computational time. The process, which has being applied during the whole validation process and the lock-in analysis, is the following one:

1. **Steady State simulation:** Convergence is verified when the steady aerodynamic coefficients (c_L and c_D) reach a steady value and the residuals lay below 10^{-12} or reach a low steady value. Reynolds Averaged Navier-Stokes (RANS) turbulence models ($k - \omega$ SST or Transition SST) are used in this first step. The chosen one will be applied to the different simulations in its different versions (URANS & SAS). Also, at this point the $y+$ values are checked.
2. **First Transient simulation:** The initial conditions will be the converged steady solution. At this point the dynamic mesh is activated and Unsteady Reynolds Averaged Navier-Stokes (URANS) turbulence models are used. As the behaviour of the aerodynamic parameters c_L and c_D will vary from one imposed motion to another; also, the contours of the turbulence viscosity will be used as explained in subsection 6.6.
3. **Second Transient simulation:** Once the transient solution of the URANS turbulence model has converged. It is ran one more time (URANS $k - \omega$ SST or URANS Trans. SST depending on the initial choice) during a number of time steps which makes possible the correct extraction of time dependent parameters and statistics.
4. **Third Transient simulation:** From the converged transient results the turbulence model is modified from URANS to SAS and ran until convergence is reached. Also, by recommendation of the manual, the time scheme is changed from 2^{nd} order implicit to bounded 2^{nd} order implicit.
5. **Forth Transient simulation:** Once the transient solution with SAS turbulence model has converged, it is ran one more time with the same turbulence model (SAS $k - \omega$ SST or SAS Trans. SST) during a number of time steps which makes possible the correct extraction of time dependent parameters and statistics.

6.10 Results and Validation

6.10.1 Lift and Drag Coefficients

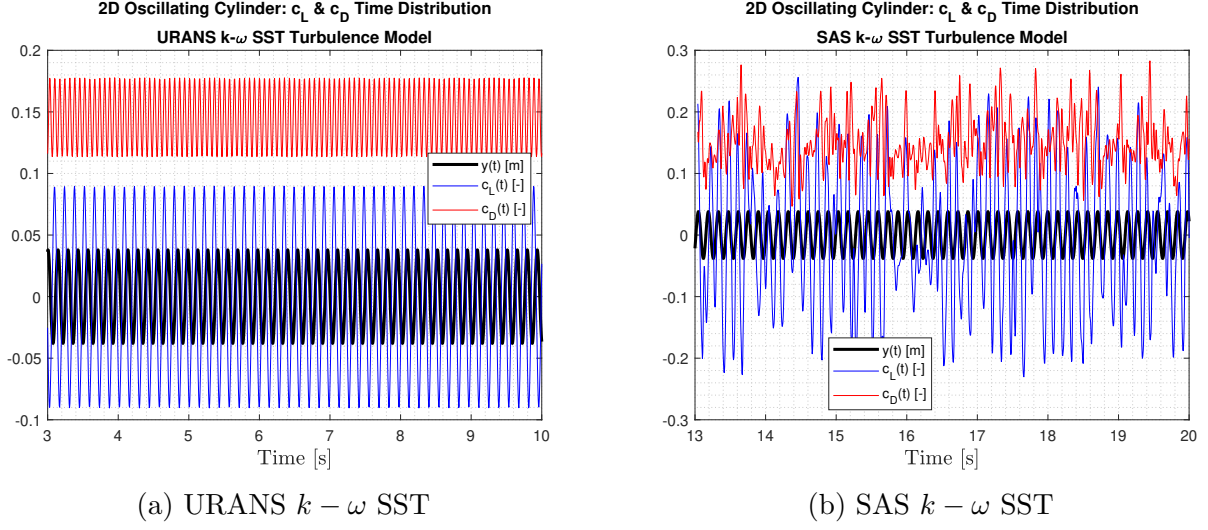


Figure 47: Time distribution of the monitored lift and drag coefficients ($c_{L_{mo}}(t)$ & $c_{L_{mo}}(t)$) in ANSYS Fluent for the moving cylinder at imposed motion frequency of $f_{osc} = 7.07$ [Hz] and amplitude of $|y| = 0.038$ [m] at $U_\infty = 4.2786$ [m/s] ($Re \sim 2.9 \cdot 10^4$). Results extracted from CFD codes using $k-\omega$ SST turbulence model in both URANS (left) and SAS (right) versions

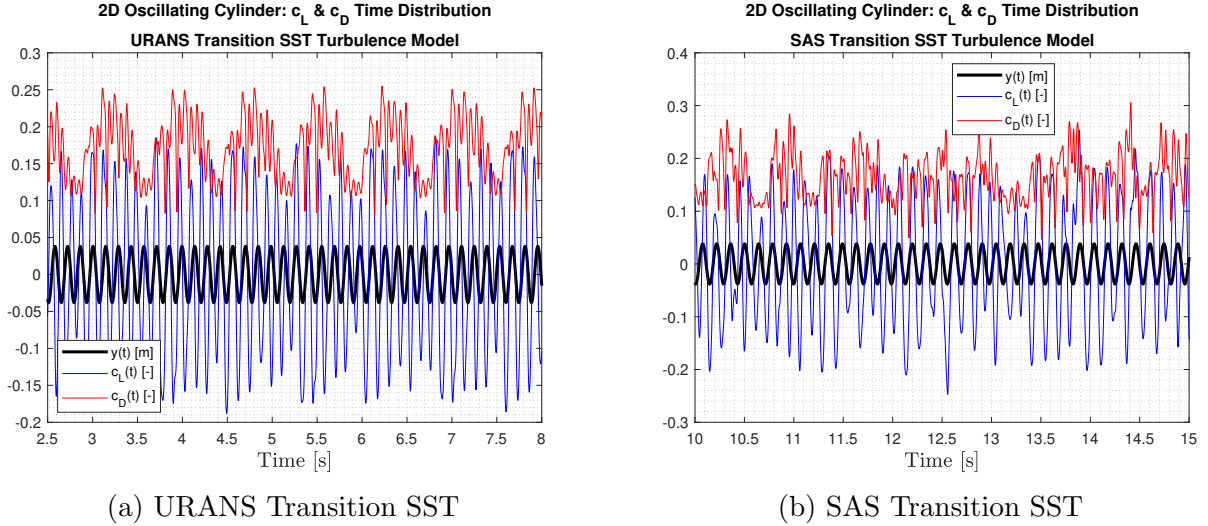


Figure 48: Time distribution of the monitored lift and drag coefficients ($c_{L_{mo}}(t)$ & $c_{L_{mo}}(t)$) in ANSYS Fluent for the moving cylinder at imposed motion frequency of $f_{osc} = 7.07$ [Hz] and amplitude of $|y| = 0.038$ [m] at $U_\infty = 4.2786$ [m/s] ($Re \sim 2.9 \cdot 10^4$). Results extracted from CFD codes using Transition SST turbulence model in both URANS (left) and SAS (right) versions

As it has been discussed in subsection 4.5 and subsubsection 5.6.1, the time evolution of the aerodynamic coefficients directly extracted from the commercial software vary from one turbulence model to another. This difference is even greater for dynamic meshes. On the one hand,

the only perfectly sinusoidal time signal (Figure 47a) is obtained by means of URANS $k - \omega$ SST turbulence model. Moreover, the URANS transition SST (Figure 48a) and SAS transition SST (Figure 48b) turbulence models present a beating phenomenon with a clearly marked pattern and a wider frequency content. On the other hand, in general terms the SAS models present a wider frequency expectrum compared to URANS models (as it happened in subsection 4.5 and subsubsection 5.6.1). As discussed by Ju-Yeol You & Oh Joon Kwon in [55] URANS turbulence models are more dissipative than SAS model which results in a 2D regular vortex shedding for the former and 3D irregular for the latter. This behaviour is translated in the in $c_L(t)$ and $c_D(t)$ time distributions given by the software and presented in Figure 47 and Figure 48.

The beating phenomenon that presents $c_L(t)$ in Figure 48 is the direct consequence of its frequency components. On the one hand, the imposed frequency of motion (f_{osc}) which is the main frequency of the signal and presents the greatest amplitude. On the other hand, the frequency which follows the Strouhal law (f_{vs}).

Regarding the time mean values of the aerodynamic coefficients (Table 21), SAS and URANS $k - \omega$ SST turbulence models result in slightly lower values of \bar{c}_D . However, no big differences can be determined in \bar{c}_L .

	URANS $k - \omega$ SST	URANS Trans. SST	SAS $k - \omega$ SST	SAS Trans. SST
\bar{c}_L [-]	-0.0421	-0.0029	-0.06	0.047
\bar{c}_D [-]	1.5701	1.624	1.546	1.650

Table 21: Time mean values of lift and drag coefficients obtained from each turbulence model for the moving cylinder under an imposed motion of $f_{osc} = 7.07$ [Hz] & $|y| = 0.038$ [m] at $U_\infty = 4.8627$ [m/s] ($Re \sim 2.9 \cdot 10^4$)

6.10.2 Shedding Frequency (f_{vs})

Table 22 presents the vortex shedding frequencies extracted from the $c_L(t)$ time signals. It has been reasoned previously that the time distribution of the lift coefficient over a cylinder fluctuates at the frequency at which the vortex shedding occurs. In overall, by means of a FFT, the main frequency of those signals has been identified and in all of them lays really close to the frequency of the motion of the structure. Hence, as the vortex shedding happens at the same frequency as the imposed sinusoidal motion of the cylinder, the fluid-structure system is within the lock-in region. Consequently, the CFD code is capable, at least in terms of frequency, of capturing the experimental behaviour of the structure in the wind tunnel.

	URANS $k - \omega$ SST	URANS Trans. SST	SAS $k - \omega$ SST	SAS Trans. SST
f_{vs} [Hz]	7.07	7.05	7.07	7.07

Table 22: Vortex Shedding frequency obtained from each turbulence model for the moving cylinder under an imposed motion of $f_{osc} = 7.07$ [Hz] & $|y| = 0.038$ [m] at $U_\infty = 4.8627$ [m/s] ($Re \sim 2.9 \cdot 10^4$)

6.10.3 Time Mean 2D Loading

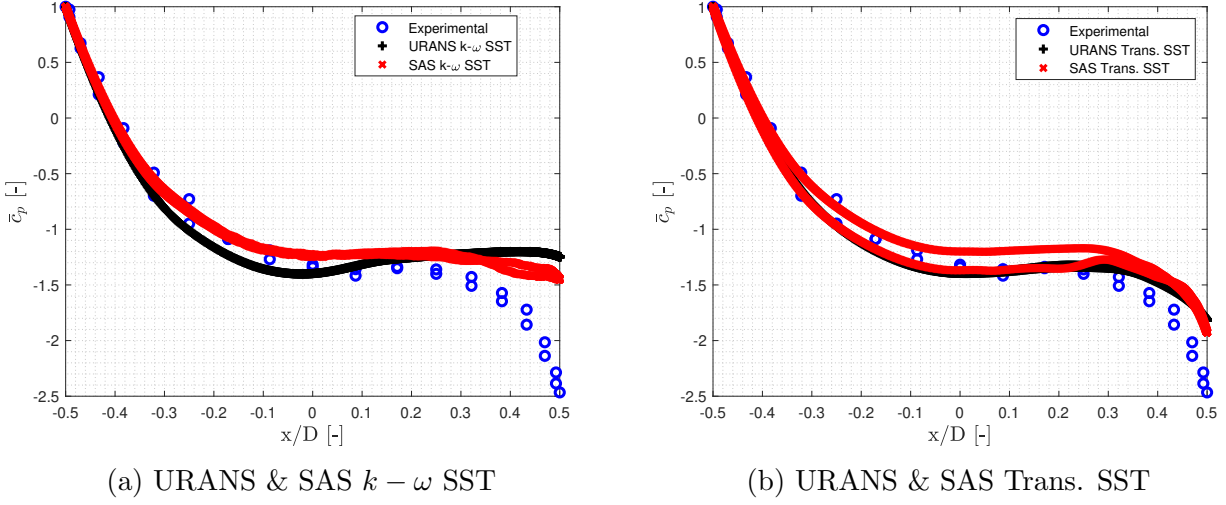


Figure 49: Spatial distribution of \bar{c}_p over the cylinder from URANS (black) and SAS (red) Transition SST (right) and URANS (black) and SAS (red) $k-\omega$ SST (left) turbulence models. Imposed motion of $f_{osc} = 7.07$ [Hz] & $|y| = 0.038$ [m] and airspeed $U_\infty = 4.8627$ [m/s] ($Re \sim 2.9 \cdot 10^4$)

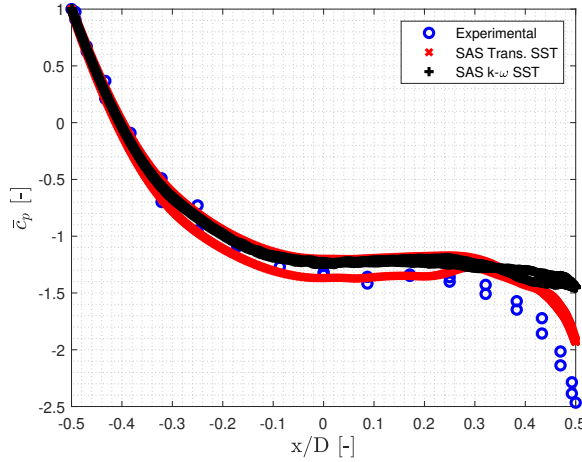


Figure 50: Spatial distribution of \bar{c}_p over the 2D oscillating cylinder. Imposed motion of $f_{osc} = 7.07$ [Hz] & $|y| = 0.038$ [m] and airspeed $U_\infty = 4.8627$ [m/s] ($Re \sim 2.9 \cdot 10^4$). SAS Transition SST (red) ; SAS $k - \omega$ SST (black)

As it was done for the static set up, URANS $k - \omega$ SST, URANS Transition SST, SAS $k - \omega$ SST and SAS Transition SST turbulence models have been compared to the experimental data. On the one hand, Figure 50 shows the time mean c_p distribution on the cylinder as a function of the streamwise coordinate x (see Figure 17) for the tested SAS models. Both turbulence models resolved accurately the attached flow region around the front of the cylinder, but they fail to do it with the near wake flow region. However, SAS Transitional SST turbulence model resulted

in a closer \bar{c}_p distribution with slightly less negative values than the experimental data in the wake region of the cylinder. The reason for that could be that while the experimental data is undergoing VIV, its vibratory motion could not be perfectly sinusoidal in the perpendicular direction of the mean flow, but it could contain components at other frequencies and directions modifying the pressure distribution over the cylinder. Probably, the inherent damping of the structure and the surface roughness of the cylinder could also affect the \bar{c}_p distribution over the cylinder.

6.11 Conclusions

The current section has presented and discussed the numerical validation of the CFD code of a 2D dynamic domain which intends to model the flow around an oscillating circular cylinder. After having done a mesh independence analysis and a convergence study of several parameters related to the numerical schemes used in the code, 4 turbulence models have been validated against the experimental data extracted from the wind tunnel (section 3).

As it happened in the validation of the 2D static cylinder code, the attached flow over the cylinder seems to be well captured by all the turbulence models tested in the current section. Around the rear of the cylinder, however, the best behaviour is presented by SAS Transition SST turbulence model. It presents a good balance between the accuracy of the results and computational time for the resolution of the problem, even if the time mean c_p distribution over the cylinder slightly differs near the end of the cylinder with respect to the experimental data. It could be due to several imperfections of the experimental set-up (inherent damping of the structure, no perfect 1D motion of the cylinder, surface roughness...), the non perfectly 2D behaviour of the vortex shedding at the imposed motion conditions and the fact that a cylinder undergoing VIV does not vibrate in a pure sinusoidal way but close to it.

Even if some discrepancies have arisen in the new CFD code, it has been validated and it will be used for the lock-in analysis in the present project. A list of the main parameters can be found below:

- **Number of Nodes:** 65691
- **Number of Elements:** 83966
- **First Cell Height in Inflation Layer:** 0.00005 [m]
- **Number of Cells in Inflation Layer:** 20
- **Dynamic Mesh Method:** Diffusion Based
- **Pressure-Velocity Coupling Scheme:** SIMPLE
- **Time Step Size:** 0.001 [s]
- **Iterations per Time Step:** 30
- **Turbulence Model:** SAS Transition SST

- **Transient Integration Scheme:** 2^{nd} Order Implicit

and boundary conditions:

- Velocity Inlet
- Pressure Outlet
- Upper and Lower No-slipping Wall
- No-slipping wall on the cylinder

7 Study of Lock-in Region

7.1 Introduction

Once the CFD code for the modelling of the 2D moving cylinder has been validated against the experimental data extracted from the wind tunnel; in this section, an extensive and precise analysis of the physical phenomena taking place under prescribed motion of oscillating cylinders will be performed. In order to do that the following parameters will be analyzed: (a) the unsteady pressure loading, $c_p(t)$; (b) the lift coefficient, $c_L(t)$, on the cylinder; (c) the energy transfer between the cylinder and the fluid flow, c_E ; (d) modes/patterns of the shedding vortex process in the wake. The study will be carried out at a free-stream velocity of $U_\infty = 4.2786$ [m/s] ($Re \sim 2.9 \cdot 10^4$) and incoming turbulence level of 0.2%.

Two different analyses will be performed:

- Constant imposed amplitude at variable frequency
- Constant imposed frequency at variable amplitude

For this purpose, a wide range of frequencies will be examined in order to place precisely the different transition points at three different imposed amplitudes (0.038 [m], 0.02 [m], 0.005 [m]).

The first big and obvious division is: when a oscillating cylinder sheds wake vortices at the mean frequency which corresponds to the Strouhal law (unlocked) and the ones with a mean shedding frequency equal to the frequency of the motion (locked). "Mean frequency" defines the frequency of highest magnitude, but it does not neglect the presence of different frequency content in the vortex shedding. The transition between both situations will depend on both amplitude and frequency of the imposed motion.

Then, it will be reasoned that the lock-in cases can be splitted in two subgroups. On the one hand, a narrow region close to the transition presents a lower amplitude of the main frequency of the lift coefficient, a bigger and positive phase difference between the motion and the component related to the main frequency of the lift coefficient. On the other hand, a wider region at higher imposed frequencies results in a higher amplitude related to the main frequency of the lift coefficient and negative phase-difference. Hence, the energy transfer between the oscillatory structure and fluid flow will switch directions. Furthermore, the spatial averaged value of \bar{c}_p on the cylinder will reach its maximum value at the transition point between these two situations. Eventually, the distribution of the time mean value of the unsteady pressure over on the cylinder will be examined.

Further discussion of the time dependent properties of $c_p(t)$ and an analysis on the frequency domain can be found in a separated section (section 8).

7.2 Analyzed Cases

An eventual total number of 23 different combinations have been performed in order to carry out a precise study of the evolution of the unsteady loading over the moving cylinder, different modes of the wake and energy transfer between the cylinder and the fluid flow. Table 23 summarizes the imposed parameters in each test case and Figure 51 gives a general overview of the transition between the lock-in region and unlocked cases on the "amplitude-frequency" plane.

Cases	f_{osc}/f_{vs}^o [-]	$ y /D$ [-]
1	0.422	0.38
2	0.563	0.38
3	0.633	0.38
4	0.677	0.38
5	0.703	0.38
6	0.71	0.38
7	0.756	0.38
8	0.816	0.38
9	0.844	0.38
10	0.915	0.38
11	1	0.38
12	1.14	0.38
13	1.393	0.38
14	0.527	0.2
15	0.6328	0.2
16	0.716	0.2
17	0.774	0.2
18	0.816	0.2
19	0.915	0.2
20	1	0.2
21	0.677	0.05
22	0.816	0.05
23	1	0.05

Table 23: Properties of the prescribed motion of the analyzed cases

The locked cases define an inverted triangular shaped region (V shape) in which the frequency range gets wider for increasing values of imposed amplitudes (Figure 51). Furthermore, this region is not symmetric with respect to $f_{osc}/f_{vs}^o = 1$. The 'unlocked-locked' transition takes place at f_{osc} values which are closer to f_{vs}^o for the lower range of frequencies, than for the upper range.

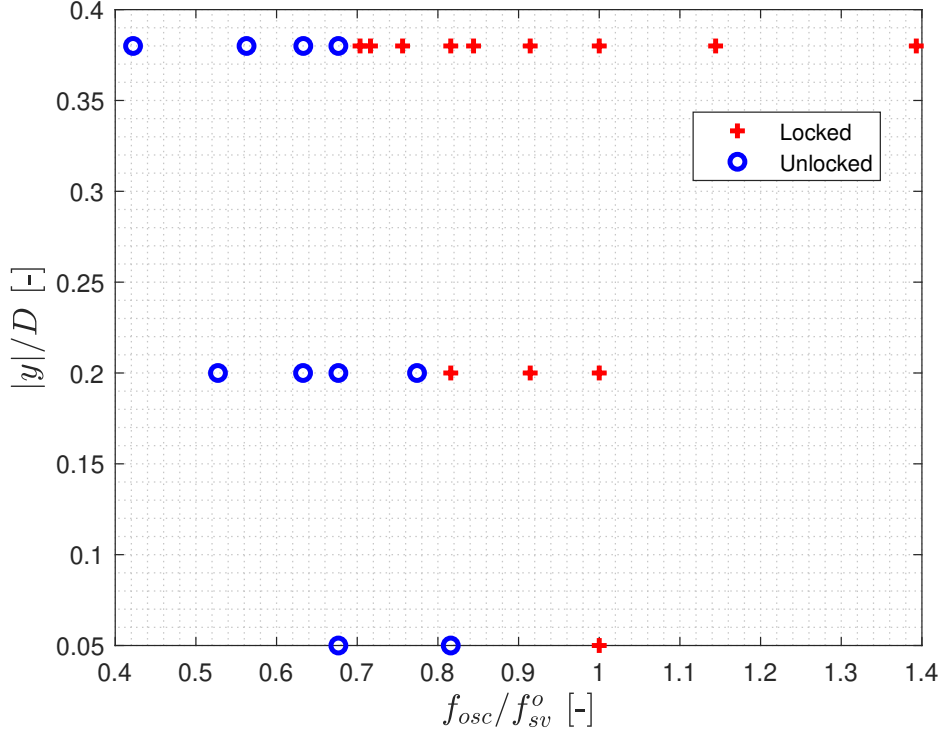


Figure 51: Classification of the analyzed cases in locked (red-cross) and unlocked (blue circle) conditions. Non-dimensional amplitude vs non-dimensional frequency of the imposed motion of the cylinder. $Re \sim 2.9 \cdot 10^4$

7.3 Analysis at constant Imposed Amplitude ($\frac{|y|}{D}$)

Several performed cases with constant imposed amplitudes will be compared at different oscillating frequencies. As presented in Table 23 three different amplitudes have been simulated: $|y|/D = 0.38; 0.2; 0.05$. In this section they will be analyzed independently. The results at $|y|/D = 0.38$ non-dimensional amplitude will be discussed in the present project in order to have a wider range of oscillating frequencies and analyse the effect that this last parameter has on the properties of both fluid and structure.

7.3.1 $c_L(t)$: Frequency Content

Figure 52 presents the FFT of the resultant $c_L(t)$ signals from the different simulated cases at imposed motions with $|y|/D = 0.38$ and variable frequencies. Furthermore, Table 24 contains the summary in terms of predominant frequency content of each $c_L(t)$ signal in order to make easier the identification of the numerical values of Figure 52. All the performed simulations can be divided in two big groups in terms of frequency content extracted from their Fast Fourier Transform Analysis.

On the one hand, at low oscillatory frequencies, the time signal of the lift coefficient over the cylinder is composed by two predominant frequencies. The greatest one, will be defined as the vortex shedding frequency (f_{vs}), which is not the same as the vortex shedding frequency of the

static cylinder (f_{sv}^o) but lays close to it. The next one, however, coincides with the frequency of the imposed motion to the cylinder. As f_{osc} increases, the difference between the amplitude related to the previous frequencies decreases until f_{osc} overcomes f_{vs} and becomes the predominant frequency (see case $f_{osc}/f_{vs}^o = 0.703$ in Table 24). At this point, the oscillatory motion of the cylinder takes control over the vortex shedding process imposing its own frequency. This transition takes places around $f_{osc}/f_{vs}^o \sim 0.7$ in Figure 52 where the main frequencies are not extremely clear as the frequency content at this region is pretty wide. Moreover, generally the frequency content of $c_L(t)$ for unlocked cases is wider and it keeps increasing until the transition unlocked-locked takes place.

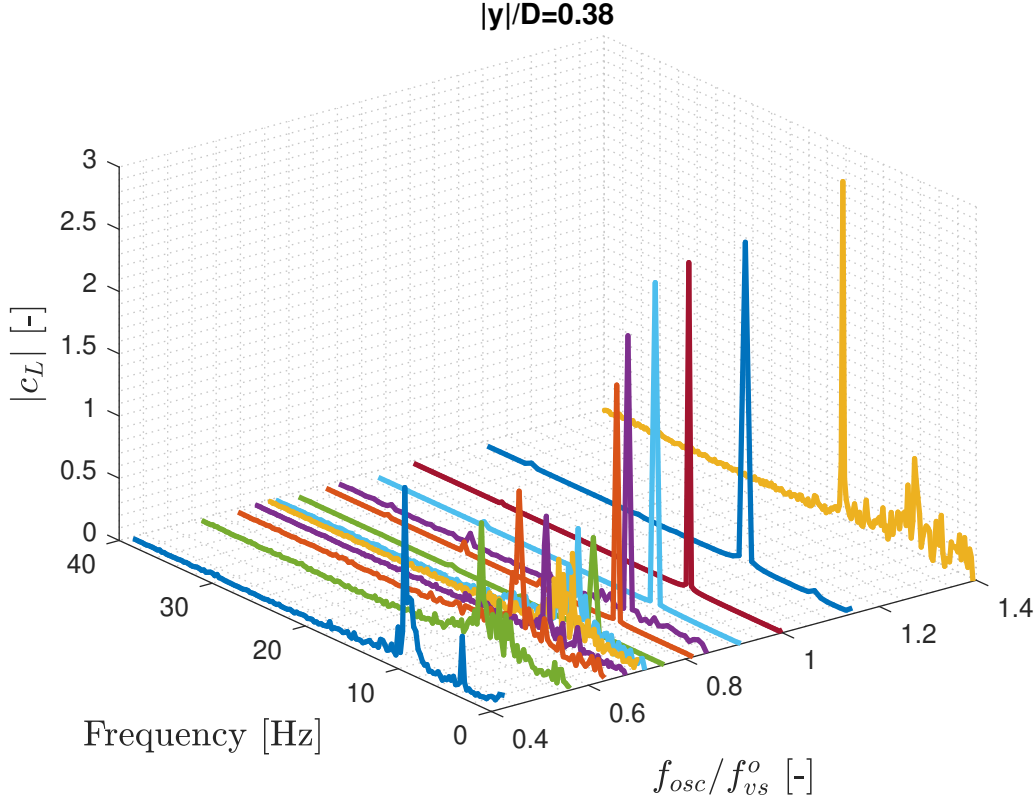


Figure 52: FFT of $c_L(t)$ for the different cases performed with $|y|/D = 0.38$ at $U_\infty = 4.8627$ [m/s] ($Re \sim 2.9 \cdot 10^4$)

$f_{osc}/f_{vs}^o [-]$	Locked-On	$f_{vs1}/f_{vs}^o [-]$	$f_{vs2}/f_{vs}^o [-]$
0.422	NO	1.03	0.422
0.563	NO	0.95	0.563
0.633	NO	0.976	0.633
0.677	NO	1.01	0.678
0.703	YES	0.705	0.968
0.716	YES	0.716	1.01
0.756	YES	0.756	-
0.816	YES	0.816	-
0.844	YES	0.844	-
0.915	YES	0.915	-
1	YES	1	-
1.14	YES	1.14	-
1.393	YES	1.391	-

Table 24: Predominant frequencies extracted from the FFT of $c_L(t)$ resultant from numerical simulation under imposed motion of $|y|/D = 0.38$ amplitude and variable frequency (f_{osc}/f_{vs}^o) at $Re \sim 2.9 \cdot 10^4$. f_{vs1} , frequency of biggest magnitude; f_{vs2} , frequency of second biggest magnitude.

On the other hand, there is a wide range of imposed frequency values at which the f_{vs} coincides with f_{osc} . These time signals present narrower frequency content which is composed, generally, by one predominant frequency ($f_{vs} = f_{osc}$) and its higher harmonics. However, close to the transition point, the frequency content in the time signals is wide. It keeps decreasing until around $f_{osc}/f_{vs}^o = 1$. Hence, all the energy of the signal will be concentrating at a punctual frequencies increasing the resultant amplitude related to the main frequency $|c_L|$. Eventually, at higher imposed frequencies, the frequency content of the signals will widen again until the right 'locked-unlocked' transition.

Table 24 aims to reflect in a easy and simple way how the main frequency of $c_L(t)$ switches from a close value to the vortex shedding frequency of a static cylinder that follows the Strouhal law until it equates the imposed motion frequency as this last one gets closer to $f_{osc}/f_{vs}^o = 1$.

7.3.2 $c_L(t)$: Amplitude ($|c_L|$) and Phase (ϕ_L)

The lift coefficient will be modeled as a sinusoidal time signal of constant amplitude, $|c_L|$, and the phase difference, ϕ_L (Equation 42). Both parameters will be computed from the main component of $c_L(t)$ time signal extracted from the numerical simulations, where $|c_L|$ is the amplitude related to the main frequency of $c_L(t)$ and ϕ_L is the phase difference of the main frequency of $c_L(t)$ with respect to the motion of the cylinder, $y(t)$.

$$c_L(t) = |c_L| \sin(2\pi f_{vs} t + \phi_L) \quad (6)$$

The previous definition (Equation 6) is accurate for the motions with locked vortex shedding as shown in Figure 52 where there is only one predominant frequency at which $f_{vs} = f_{osc}$ and the frequency content of $c_L(t)$ is limited. For those cases which are unlocked or lay close to the 'unlocked-locked' boundary, however, the frequency content of the $c_L(t)$ signal is wider and there can be more than one predominant frequency with similar amplitudes (e.g $f_{osc}/f_{vs}^o = 0.703$).

In these cases, it is obvious that there is a loss of information that can be quite big, for example, for the unlocked cases, a better approach could be the sum of two simple signals at f_{osc} and f_{vs} . Nevertheless, this definition has also been applied as a reference is needed to analyze the evolution of the amplitude related to the main frequency of the lift coefficient, $|c_L|$, with f_{osc} . Regarding ϕ_L , in the case of unlocked cases, where the main frequency of $c_L(t)$ is different to the motion frequency, makes no sense to compare the phase difference between the time signals as it will be different at each reference point, hence, it is not presented in Figure 53b.

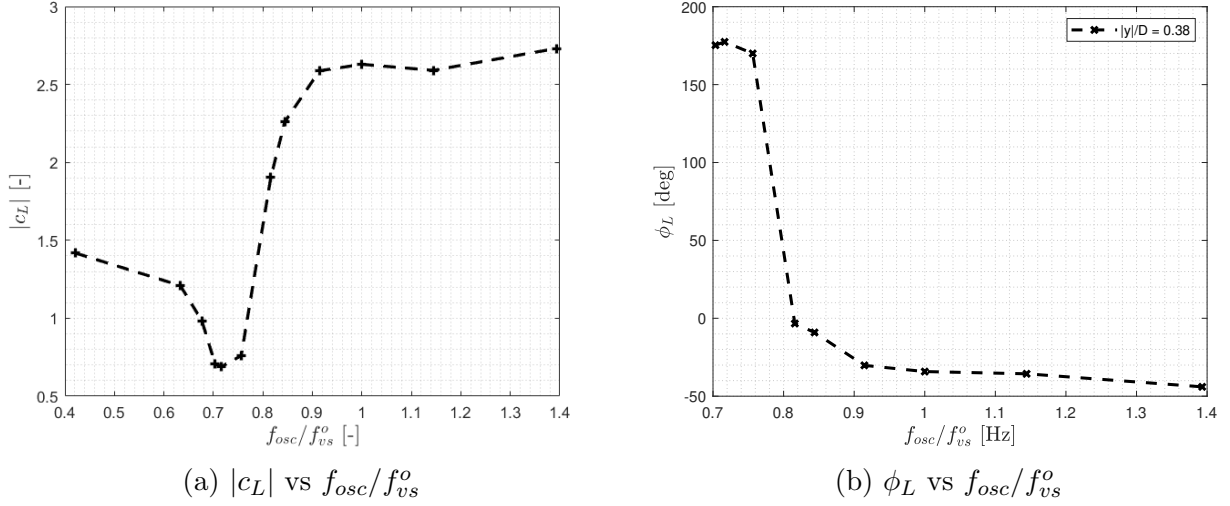


Figure 53: Evolution of the amplitude related to the main frequency of the lift coefficient (left) and phase with respect to the imposed motion of the cylinder (right) as a function of the imposed frequency. Motion with constant amplitude $|y|/D = 0.38$ at $Re \sim 2.9 \cdot 10^4$

In the same way as discussed in subsubsection 7.3.1, three big groups of imposed motions can be defined. First, the value of $|c_L|$ decreases while the imposed frequency increases reaching the minimum value at $f_{osc}/f_{vs}^o \sim 0.7$ which corresponds to the first value of locked cases. At this point the main frequency of $c_L(t)$ switches from f_{vs} to f_{osc} . Then, a small range of frequencies $f_{osc}/f_{vs}^o \in [0.7 - 0.8]$ in which $|c_L|$ presents a low value precedes a steep increase of it. It reaches close to its maximum value at $f_{osc}/f_{vs}^o \sim 1$. Then it keeps increasing in a lower rate (nearly constant) until posterior locked-unlocked transition.

The evolution of $|c_L|$ could be explained looking at the frequency content presented in (Figure 52) of the time signal $c_L(t)$ for different imposed motions. The decrease of $|c_L|$ could be due to the distribution of the energy in a bigger number of frequencies: moving from two predominant frequencies within the unlocked cases, to a noisy signal at transition. Amongst the locked cases, as the structural motion leads the vortex shedding phenomenon, the energy is concentrated at $f_{vs} = f_{osc}$ resulting in a close to a sinusoidal time signal with a drastic increment in amplitude.

The phase difference between the components corresponding to the main frequency of $c_L(t)$ and $y(t)$, ϕ_L is not trivial. Theoretically, if both signals have the same harmonic properties (frequency content), ϕ_L should be constant. However, even if the main frequency of the lift, f_{vs} for the locked cases is equal to the frequency of the motion (f_{osc}), it is not a pure sinusoidal

signal. Hence, ϕ_L will slightly vary depending on the reference point taken. The evolution of the phase between the main component of the lift force and the structural motion with respect to the frequency of the motion of the cylinder (Figure 53b) presents a hill shape with its maximum peak value at around the "unlocked-locked" transition boundary $f_{osc}/f_{vs}^o \sim 0.7$. There is a narrow range of frequencies in which ϕ_L increases up to nearly 180° , but never reaching it. It is remarkable the drastic decay that ϕ_L suffers down to negative values at $f_{osc}/f_{vs}^o \sim 0.8$.

7.3.3 Time Mean Pressure Coefficient: \bar{c}_p

The time mean values of the pressure coefficients have been calculated over 10 oscillation cycles. The different resultant \bar{c}_p distribution over the cylinder can be split in three different groups with common properties: clearly unlocked (Figure 54a) and locked cases (Figure 55a) divided by a transitional period (Figure 54b).

On the one hand, the unlocked cases present the highest \bar{c}_p values at the foremost points of the cylinder. Moreover, they do suffer the deepest decrease of pressure (consequently, the highest acceleration and posterior deceleration of the flow). Due to the adverse pressure gradient (light recovery of \bar{c}_p) the separation of the boundary layer takes place at $x/D \sim 0.1$ (see Figure 56, it coincides with the location at which the magnitude of the time mean friction coefficient $\bar{c}_f = 0$, Equation 7). While the flow keeps detached, a nearly flat distribution of \bar{c}_p can be identified between $x/D \in [0.1, 0.3]$. Eventually, the flow reattaches (see Figure 56) and \bar{c}_p moves to more negative values as reaching the end of the cylinder.

$$\bar{c}_f = \frac{\bar{\tau}_{wall}}{\frac{1}{2} \rho u_{in}^2} [-] \quad (7)$$

where, $\bar{\tau}_{wall}$ is the time mean value of the wall shear stress on the cylinder

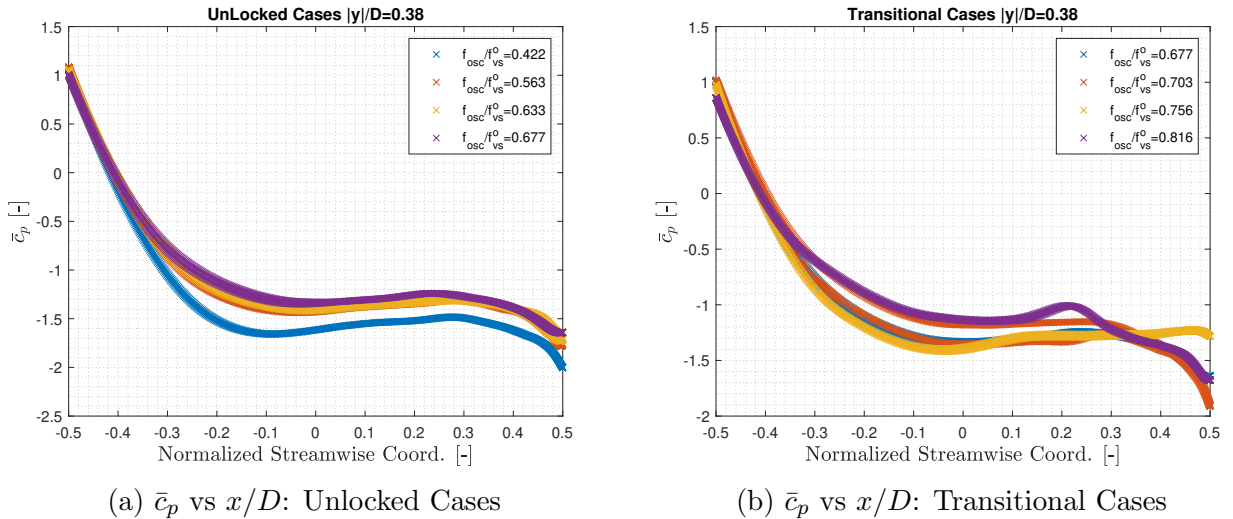


Figure 54: Time mean pressure coefficient distribution over the cylinder with constant $|y|/D = 0.38$ amplitude and different imposed frequencies at $Re \sim 2.9 \cdot 10^4$. Unlocked cases (left). Cases close to the 'unlocked-locked' transition (right)

Increasing f_{osc} , the maximum value of the pressure coefficient, which is located at the front of the cylinder, decreases. However, the rest of the spatial distribution moves towards bigger values with smaller negative slopes (smaller acceleration reaching a smaller maximum velocity of the flow over the cylinder). Also, the separation point moves slightly to higher values of streamwise coordinate but keeping within $x/D \in (0.1 - 0.2)$ values (Figure 56).

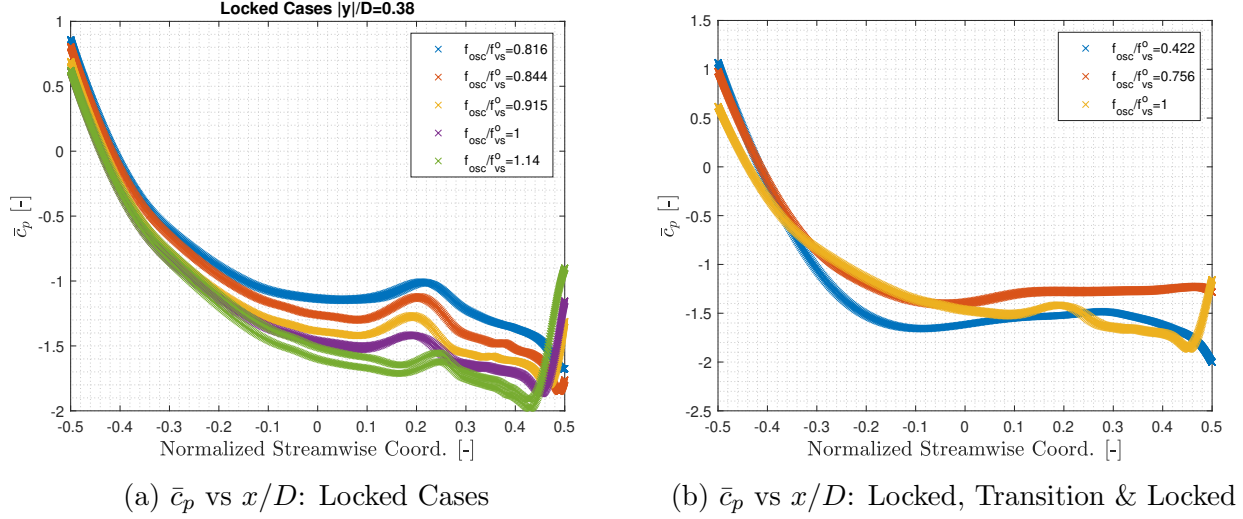


Figure 55: Time mean pressure coefficient distribution over the cylinder with constant $|y|/D = 0.38$ amplitude and different imposed frequencies at $Re \sim 2.9 \cdot 10^4$. Comparison between one of the cases of each characteristic groups (right). Locked case (blue), unlocked (yellow), transitional region (orange)

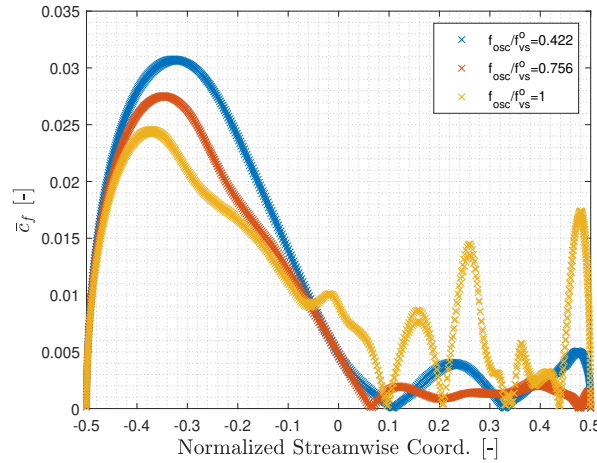


Figure 56: Time mean value of friction coefficient (\bar{c}_f) over the cylinder with constant $|y|/D = 0.38$ amplitude and 3 different imposed frequencies at $Re \sim 2.9 \cdot 10^4$. Unlocked: $f_{osc}/f_{vs}^0 = 0.422$ (blue). Transition: $f_{osc}/f_{vs}^0 = 0.756$ (orange). Locked: $f_{osc}/f_{vs}^0 = 1$ (yellow)

On the other hand, the locked cases present the lowest \bar{c}_p values at the foremost points of the cylinder followed by a smoother decay of it in streamwise direction (lower maximum flow veloc-

ity). At some point around $x/D \in [0.1 - 0.3]$, a peak arises resulting in a local increase of \bar{c}_p . It is a local separation of the flow followed by a rapid reattachment (see Figure 56) that results in a recirculation bubble. As f_{osc} increases, the mean velocity of the separated flow decreases, reaching lower \bar{c}_p values. Eventually, the pressure coefficient suffers a steep increase on its value close to the end of the cylinder (due to a second separation of the flow), reaching higher values and starting at lower x/D values as switching to higher values of f_{osc} . This could be due to the fact that increasing the motion frequency, the flow of the vortex impacts the back part of the cylinder at greater mean velocities in the opposite direction of the main fluid-flow. Furthermore, at higher imposed frequencies of the motion, the whole spatial distribution moves towards more negative values of \bar{c}_p .

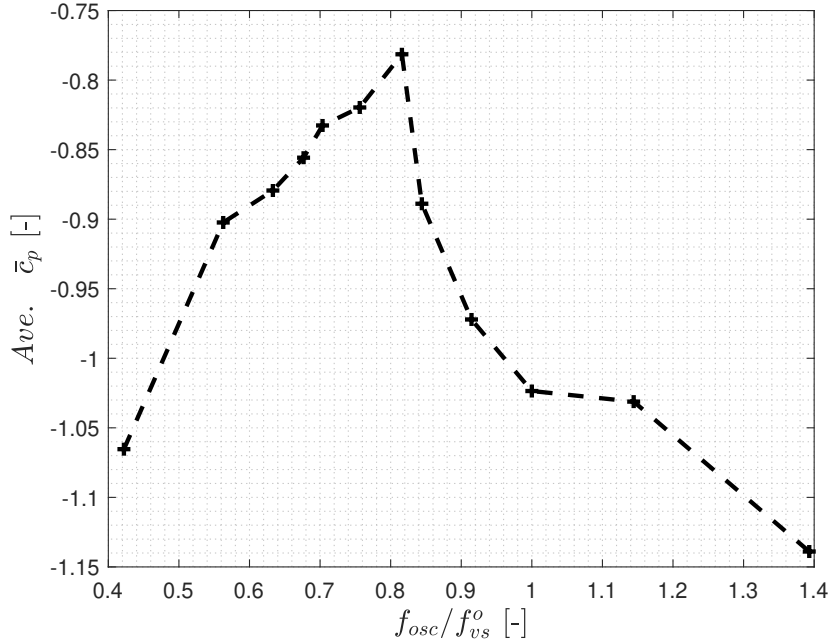


Figure 57: Spatial average of \bar{c}_p over the cylinder walls as a function of the non-dimensional frequency of the imposed motion with $|y|/D = 0.38$ at $Re \sim 2.9 \cdot 10^4$

The values of f_{osc} laying between the previously described groups, results in a transitional behaviour between the previously defined 2 situations. The maximum \bar{c}_p at the foremost point of the cylinder and the characteristic negative slope of \bar{c}_p decrease while the flow is attached to the cylinder. The separation point moves to slightly lower streamwise values, always staying at around $x/D \sim 0.1$ (see Figure 56). It is remarkable, that in this transition the flow around the second half of the cylinder, while at low imposed frequencies the reattachment takes place nearly at the rear of the cylinder, at higher values of f_{osc} , this point moves towards less positive values.

Figure 57 shows the evolution of the spatial averaged \bar{c}_p over the cylinder walls for increasing values of the frequency of the imposed motion (f_{osc}). The time mean pressure coefficient presents a continuous increase on its spatial averaged value moving towards higher f_{osc} value through the unlocked cases up to its maximum at $f_{osc}/f_{vs}^o \sim 0.8$ which coincides with the first completely

locked case (appearance of the re-circulation bubble and flat distribution at the rear), which corresponds to $f_{osc}/f_{vs}^o = 0.816$. It also coincides with the f_{osc} value at which $|c_L|$ presents a steep increase on its value (Figure 53a) and the drastic decrease of ϕ_L (Figure 53b).

7.3.4 Wake Mode

In the present section the wake mode will be characterized by its vortex shedding pattern and classified by means of the vorticity.

The vorticity is a pseudovector field that describes the local spinning motion of the fluid flow, in this case, of the wake behind the cylinder. The sign of this parameter will describe the direction of the turning flow. The definition of vorticity² for a 2D flow:

$$\Omega = \frac{\partial u}{\partial y} - \frac{\partial v}{\partial x} \quad \left[\frac{1}{s} \right] \quad (8)$$

Two patterns can be identified in the studied cases:

- **2S Vortex Shedding:** The locked cases, which present a single predominant shedding frequency (Table 24), shed vortices in 2S mode as shows Figure 58. The length of the vortex attached to the cylinder gets shorter as imposing a higher frequency to the motion of the cylinder.

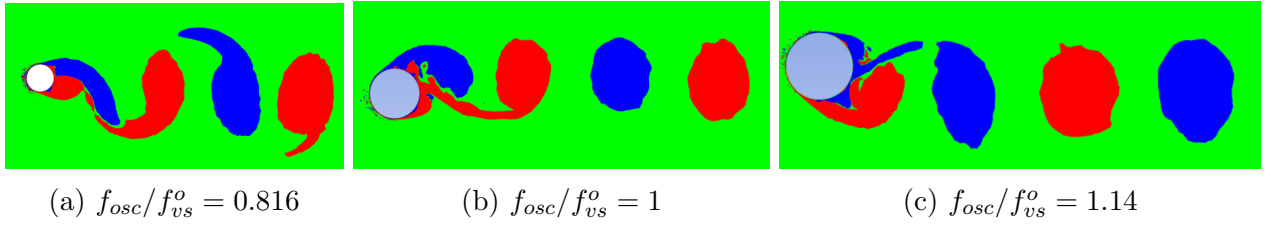


Figure 58: Vorticity (Equation 8) patterns in the wake behind the oscillatory cylinder with $|y|/D = 0.38$ of 3 locked cases $Re \sim 2.9 \cdot 10^4$. Red color refers to positive vorticity and blue to negative. It is shown a clear 2S vortex shedding mode. [73]

- **2P Vortex Shedding:** Contrary to the previous cases, the locked cases laying near the "unlocked-locked" boundary do not have a well defined wake pattern but it could be identified a tendency towards a 2P vortex shedding mode. However, as the frequency content in the wake is wider compare to the "clearly locked cases", the shedding does not happen at a well-defined frequency. Eventually, the unlocked cases do not present any defined shedding pattern.

²The derivation of Equation 8 from the general 3D definition is presented in Appendix C

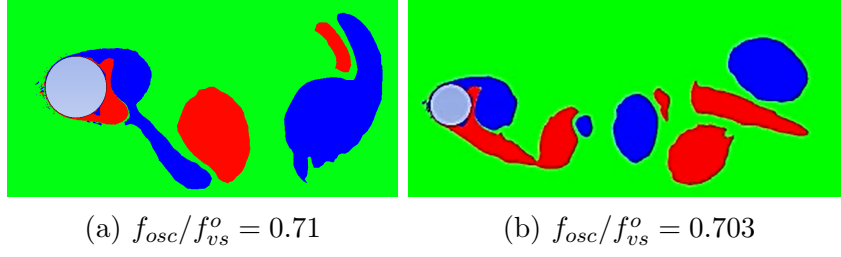


Figure 59: Vorticity (Equation 8) patterns in the wake behind the oscillatory cylinder with $|y|/D = 0.38$ at $Re \sim 2.9 \cdot 10^4$. Red color refers to positive vorticity and blue to negative

7.3.5 Energy Transfer

It is well-known that in aeroelastic systems there can be an energy transfer between the fluid and the structure in either direction, which, actually, sets the stability of the system.

In VIV (Vortex Induced Vibration) the freely vibratory motion of the cylinder starts as a response to the excitation that the natural instability of the wake (vortex shedding) produces on the structure. Therefore, there is an energy transfer from the fluid to the structure which produces the vibratory motion on it. In the present case, instead, the oscillatory motion of the cylinder is imposed and the behaviour of the wake will be the direct response to the perturbation introduced in the natural wake by the cylinder. Hence, the energy transfer could happen in both directions.

The energy transfer per cycle will be defined as the work done by the lift force on the cylinder in one period of the motion (Equation 9):

$$E_{cycle} = W_{cycle} = \int F(t) \cdot dy = \int F(t) \cdot \dot{y}(t) dt = \int_0^T L(t) \cdot \dot{y}(t) dt \quad (9)$$

where,

- $y(t)$: Displacement of the cylinder in cross direction to the incoming fluid flow
- $\dot{y}(t)$: Velocity of the cylinder in cross direction to the incoming fluid flow
- $L(t)$: Lift force acting on the cylinder. In other words, the fluid force acting on the cylinder in the direction of its motion
- $T = \frac{1}{f_{osc}}$: Period of the motion of the cylinder

Equation 9 defines the work done by the fluid on the cylinder per oscillation cycle. Therefore, a positive energy will be translated in work done by the fluid on the structure, hence (unstable system) and a negative, opposite direction (stable system). Note that in aeroelastic systems energy needs to be transfer in the positive direction for VIV to happen.

Eventually, in order to deal with non-dimensional parameters a energy transfer coefficient (c_E) will be defined as done in [45]:

$$c_E = \frac{E_{cycle}}{\frac{1}{2} \rho U_\infty^2 D} \quad (10)$$

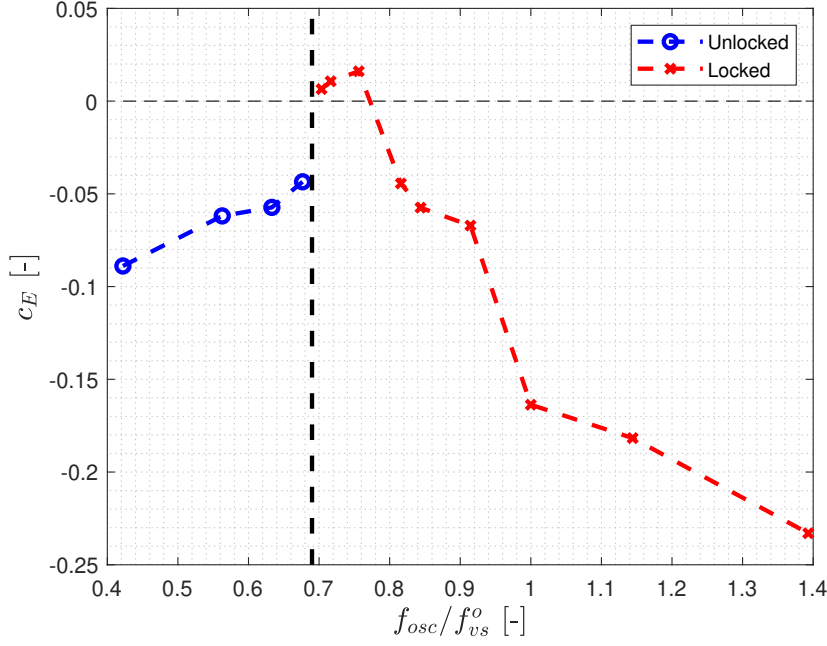


Figure 60: Evolution of the non-dimensional energy coefficient (c_E) as a function of the frequency of the imposed sinusoidal motion on the cylinder, f_{osc} , with a constant amplitude of $|y|/D = 0.38$ at $Re \sim 2.9 \cdot 10^4$

Figure 60 represents the evolution of the energy transfer between the fluid flow and the vibratory structure. It has been computed by direct numerical integration (trapezoidal integration) of the $c_L(t)$ signal extracted from simulations and the imposed motion to the cylinder, $y(t)$. Appendix D shows a simplified alternative procedure to compute the energy transmission for the locked cases, for which the $c_L(t)$ can be modelled as a sinusoidal time signal without introducing great discrepancies in the results. This method results interesting as it directly relates the phase difference between $c_L(t)$ and $y(t)$ to the energy transmission in the case of locked motion and pure sinusoidal signals.

It can be deduced that at constant airspeed ($U_\infty = 4.2786$ [m/s]) and amplitude of the motion ($|y|/D = 0.38$) nearly at the whole range of frequencies within and outside the lock-in region, the cylinder is working on the fluid (negative energy transmission). However, there is a narrow range of frequencies ($f_{osc}/f_{vs}^o \in [0.7 - 0.8]$) where the energy goes in the opposite direction. This region coincides with the start of the lock-in region where it seems there is a 2P vortex shedding mode and a phase difference between the main frequency of the lift and the motion of the cylinder between 0 and 180 degrees. Moreover, the direction of the energy transmission switches again when the spatial average of \bar{c}_p reaches its maximum and the vortex shedding mode changes from 2P to 2S. It is also the point at which the amplitude of the main frequency of the lift coefficient, $|c_L|$ suffers a rapid and violent increase and the phase difference of that component with respect to the motion of the cylinder, ϕ_L , drops down to negative values.

7.4 Analysis at constant Imposed Frequency (f_{osc}/f_{vs}^o)

In this section, the impact of the imposed amplitude has on the fluid-flow will be analyzed. For so, three amplitudes ($|y|/D = 0.38; 0.2; 0.05$) will be compared at three different constant frequencies ($f_{osc}/f_{vs}^o = 0.677, 0.816, 1$). The purpose of comparing these particular configurations is to identify, analyse and discuss what the effect of the variation of the amplitude is when the three cases lay on the unlocked ($f_{osc}/f_{vs}^o = 0.677$) or locked region ($f_{osc}/f_{vs}^o = 1$), as well as, when increasing the amplitude triggers the transition between them ($f_{osc}/f_{vs}^o = 0.816$).

7.4.1 $c_L(t)$: Amplitude ($|c_L|$), Frequency (f_{vs}) & phase (ϕ_L)

Figure 61 presents the FFT of the different compared imposed motions. Hence, three different levels of amplitude will be compared at each imposed frequency. However, as the signals are plotted one over the others at each of the three f_{osc}/f_{vs}^o values, individual plots are presented for a better visualization of the results.

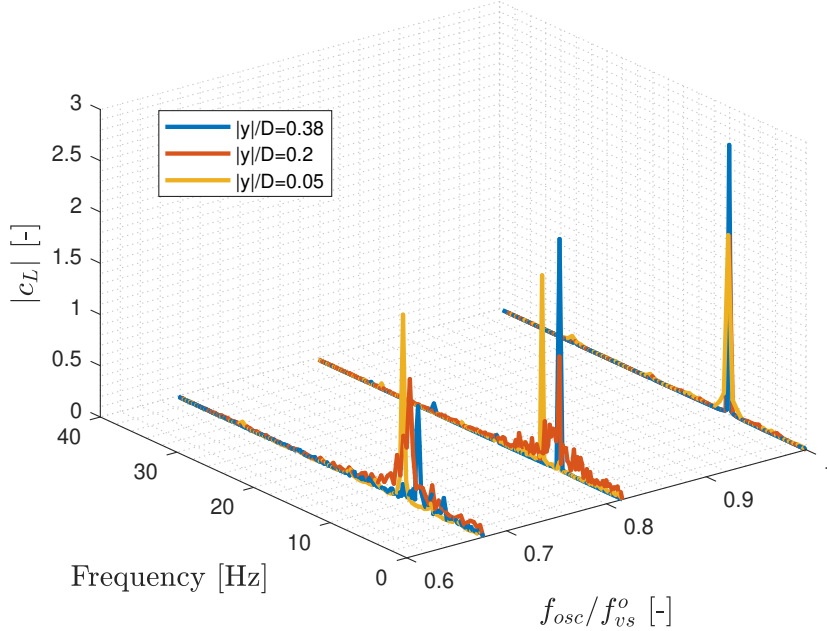


Figure 61: FFT of $c_L(t)$ for 3 different imposed motion amplitudes: $|y|/D = 0.05, 0.2, 0.38$ at 3 imposed frequencies $f_{osc}/f_{vs}^o = 0.677$, $f_{osc}/f_{vs}^o = 0.816$ & $f_{osc}/f_{vs}^o = 1$ at $Re \sim 2.9 \cdot 10^4$

The frequency spectrum of the time signal of $c_L(t)$ at $f_{osc}/f_{vs}^o = 0.677$ (Figure 62a) shows that for the three different imposed motion amplitudes, all of them are unlocked. Furthermore, the lower the amplitude of the imposed motion, the higher the amplitude of the main frequency of the lift coefficient. This behaviour could be explained as one gets away from the triangular shaped lock-in area presented in Figure 51 the energy concentrates rather in a single frequency, the dynamic vortex shedding frequency (f_{vs}). It varies from one case to another and defers from the static (f_{vs}^o) but lays close to it. Hence, the amplitude related to f_{vs} gets bigger compared to the amplitude related to f_{osc} of $c_L(t)$.

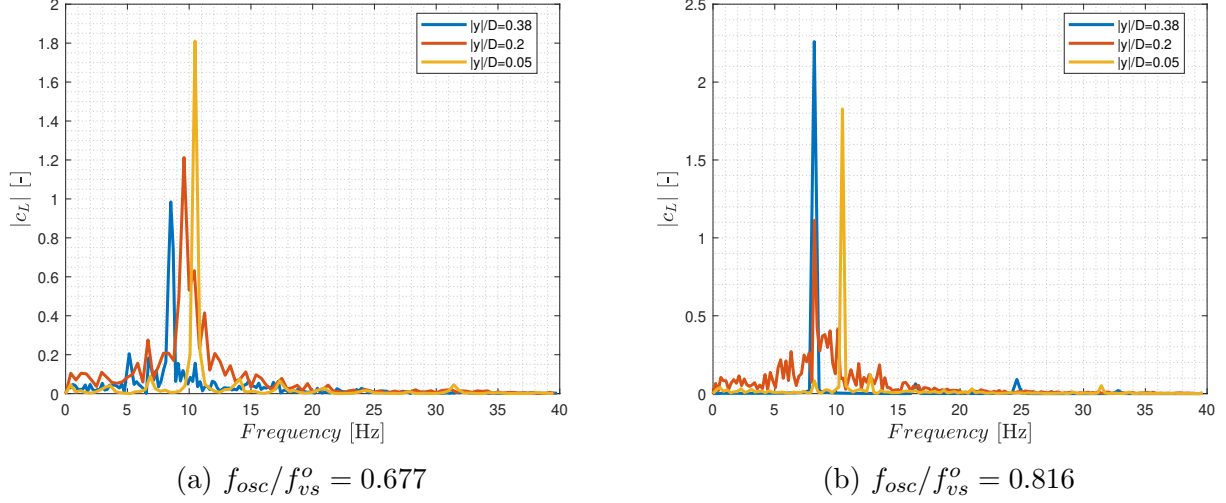


Figure 62: Fast Fourier Transform of the lift coefficient time signal at 3 different imposed motion amplitudes: $|y|/D = 0.05, 0.2, 0.38$ at $Re \sim 2.9 \cdot 10^4$. Frequency of the imposed motion $f_{osc}/f_{vs}^o = 0.677$ (left) ; $f_{osc}/f_{vs}^o = 0.816$ (right)

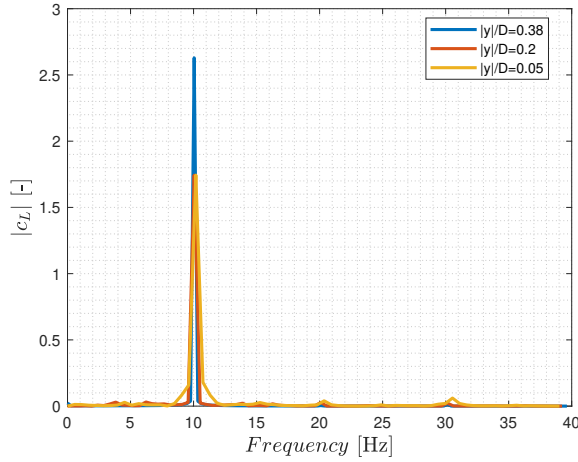


Figure 63: Fast Fourier Transform of the lift coefficient time signal with 3 different imposed motion amplitudes: $|y|/D = 0.05, 0.2, 0.38$ and $f_{osc}/f_{vs}^o = 1$ imposed frequency at $Re \sim 2.9 \cdot 10^4$

In Figure 62b the three remarkable regimes explained in subsection 7.3 are easily identifiable. This time, however, the trigger is the imposed amplitude ($|y|$) instead of the oscillatory frequency (f_{osc}). A motion with an amplitude which is 5% of the diameter of the cylinder (yellow line), lays pretty far away from the lock-in region and consequently the most energy of the system is concentrated at f_{vs} . Increasing the amplitude of the motion up to a 20% (red line), the boundary of unlocked-locked is barely exceed. It results in a $c_L(t)$ time signal with wider frequency content. The predominant vortex shedding frequency is locked with the motion frequency ($f_{vs} = f_{osc}$). Moreover, due to the fact that the energy is spread over a wider range of frequency, $|c_L|$ suffers a decay, resulting in the smallest amplitude of the presented cases. Eventually, moving up to an amplitude of the motion of the 38% of the diameter of the cylinder, the amplitude related to the main frequency, f_{osc} , of the lift coefficient presents a steep increase of its value. Also, higher

multiple harmonics of it can be identified which are negligible in magnitude compare to f_{osc} .

At $f_{osc}/f_{vs}^o = 1$ (Figure 63) all the imposed amplitudes result in locked systems in which $c_L(t)$ time signal describes a nearly perfect sinusoidal signal with $f_{vs} = f_{osc}$ and several negligible higher harmonics. The higher the imposed amplitude, $|y|$, the higher the amplitude of the main frequency of the lift coefficient, $|c_L|$.

In overall, $c_L(t)$ presents the same behaviour in terms of frequency content and amplitude as the one discussed in subsection 7.3 being the trigger for the unlocked-locked transition either the frequency or the amplitude of the imposed motion. The imposed motions can be split in three resultant differentiated groups: (a) Unlocked cases: the main component of $c_L(t)$ is at the vortex shedding frequency that lays close to the static one that respects the Strouhal law. (b) Locked cases: the main component of $c_L(t)$ is at the vortex shedding frequency that equates the imposed motion frequency. (c) Transition regime between the two previous: $c_L(t)$ has those two predominant frequencies of the same order of magnitude but the amplitude of each component depends on how far the imposed motion lays from the static vortex shedding frequency (f_{vs}^o).

Figure 64b verifies the behaviour of the phase between the main frequency of lift coefficient and the motion of the cylinder. As it has been done previously (subsubsection 7.3.2), only the phase of the locked cases is presented. Moving to higher values of amplitudes at constant frequency it can be seen for the cases of $f_{osc}/f_{vs}^o = 1$ & $f_{osc}/f_{vs}^o = 0.816$ while the case at $|y|/D = 0.05$ lays close to the transitional boundary results in a phase close to 180° , moving to higher amplitudes results into a sudden reduction of ϕ_L to negative values.

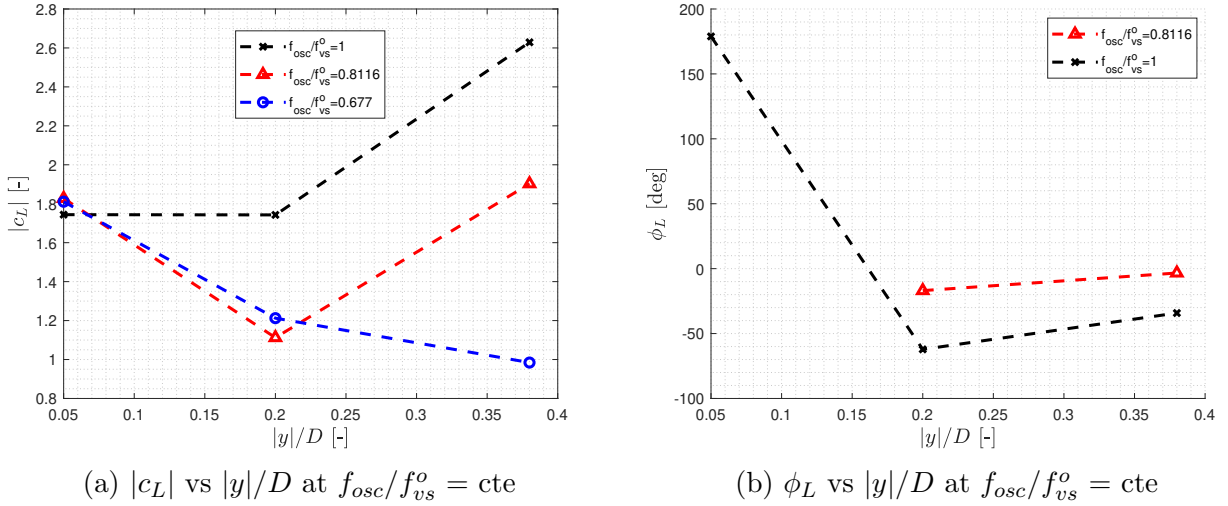


Figure 64: Evolution of $|c_L|$ (left) and ϕ_L (right) as a function of the non-dimensional amplitude of the imposed motion at constant imposed frequencies of $f_{osc}/f_{vs}^o = 0.677, 0.816, 1$ at $Re \sim 2.9 \cdot 10^4$

7.4.2 Time Mean Pressure Coefficient: \bar{c}_p

As it was done in subsubsection 7.4.1 three different amplitudes have been analyzed at three constant frequencies. As a general rule, for the three imposed frequencies, independently of being

locked or unlocked, a higher amplitude results in lower maximum \bar{c}_p value at the foremost point of the cylinder in streamwise location. This difference gets more remarked as moving to higher imposed frequencies. Moreover, the negative slope that the pressure presents in the first half of the cylinder also is being reduced in magnitude. This could be seen as greater amplitudes of motion reduces the maximum velocity that attached flow gets over the cylinder and the adverse pressure that fluid suffers is smaller too. Hence, the separation point moves to higher x/D values.

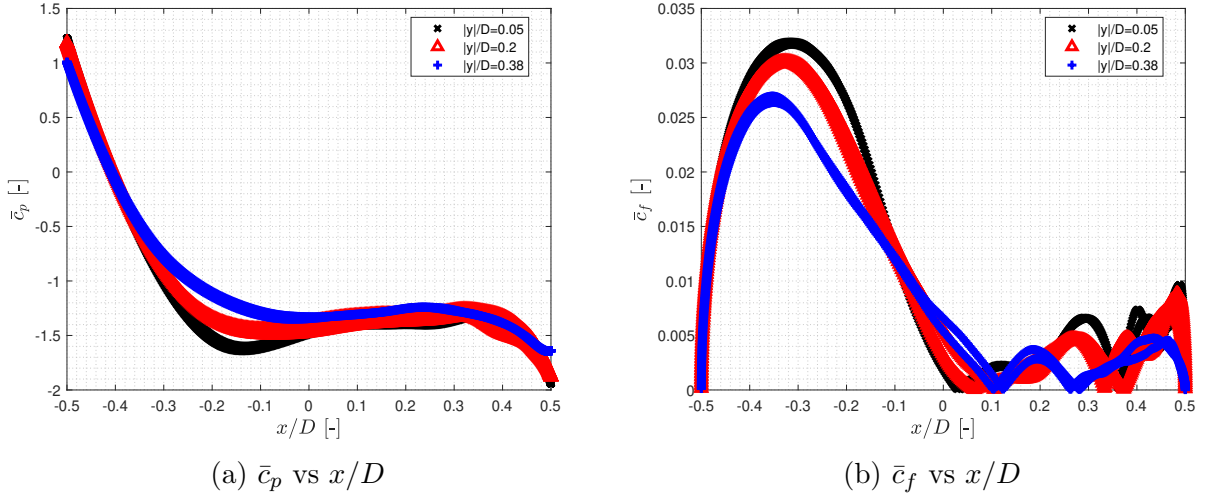


Figure 65: Time mean pressure coefficient distribution (right) and time friction coefficient (\bar{c}_f) distribution (left) over the cylinder with constant $f_{osc}/f_{vs}^o = 0.677$ frequency and different imposed amplitudes at $Re \sim 2.9 \cdot 10^4$ for locked and unlocked cases

Amongst the unlocked cases at $f_{osc}/f_{vs}^o = 0.677$ (Figure 65a), the two lower amplitudes show a flatter region at $x/D \in (0 - 0.4)$ compared to $|y|/D = 0.38$ case as the separated flow region is wider in the two first cases (see Figure 65b). Furthermore, the deep decrease of \bar{c}_p at the end part of the cylinder (Figure 65a) could be due to the fact that the flow from the wake that reattaches to the cylinder incides at higher mean velocity at lower imposed amplitudes.

At $f_{osc}/f_{vs}^o = 0.816$, the characteristic bump in the \bar{c}_p distribution at the mid-region of the cylinder discussed in subsubsection 7.3.3 arises and moves to lower streamwise coordinates when increasing the amplitude of the imposed motion (Figure 66a). In other words, at this frequency the amplitude triggers the transition from unlocked to locked situation. It makes the flow detached region narrower (moving the separation point to higher streamwise coordinates and the reattachment point to lower as it can be distinguished in Figure 66b), "arising" the characteristic bump (which illustrates a recirculation bubble) on the \bar{c}_p distribution over the cylinder.

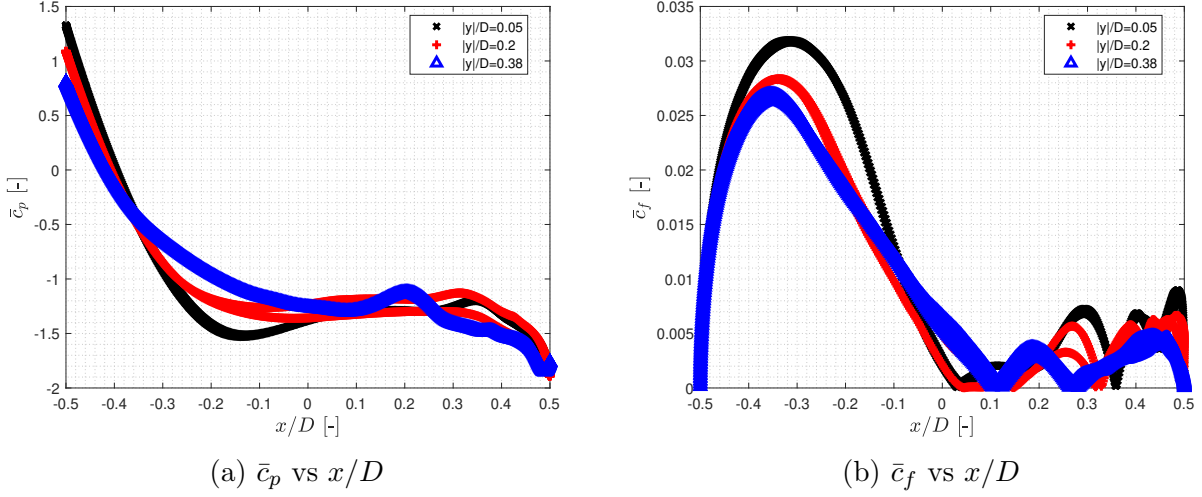


Figure 66: Time mean pressure coefficient distribution (right) and time mean friction coefficient (\bar{c}_f) distribution (left) over the cylinder with constant $f_{osc}/f_{vs}^o = 0.816$ frequency and different imposed amplitudes at $Re \sim 2.9 \cdot 10^4$ for locked and unlocked cases

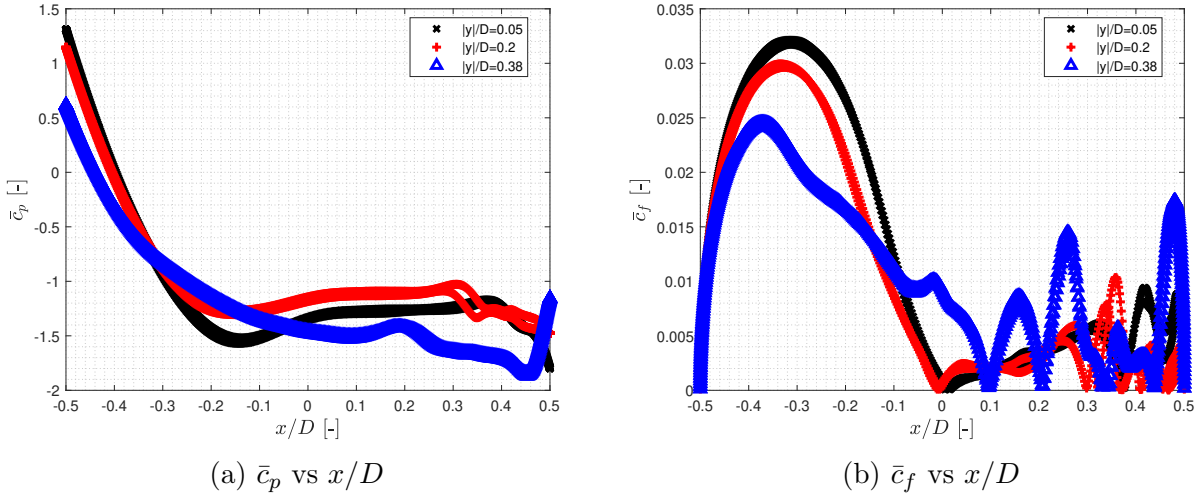


Figure 67: Time mean pressure coefficient distribution (right) and time mean friction coefficient (\bar{c}_f) distribution (left) over the cylinder with constant $f_{osc}/f_{vs}^o = 1$ frequency and different imposed amplitudes at $Re \sim 2.9 \cdot 10^4$ for locked and unlocked cases

At $f_{osc}/f_{vs}^o = 1$ (Figure 67a) the three cases present locked shedding frequencies. Apart from the aforementioned behaviour discussed previously in this section, it can be seen that the bump (recirculation bubble) in the \bar{c}_p distribution moves from nearly the end of the cylinder towards mid-region of the cylinder as the imposed amplitude increases. Furthermore, a characteristic steep climb of the loading at the end part of the cylinder arises. This last phenomenon was also present in subsection 7.3.3 at frequencies close to $f_{osc}/f_{vs}^o \sim 1$ and getting more pronounced as reaching this value. As mentioned before, it could be the consequence of a high mean velocity vortex flow impacting the back part of the cylinder in opposite direction to the main flow.

Summing up, as discussed in subsubsection 7.3.2 for $c_L(t)$, \bar{c}_p behaves in a similar way, either modifying the amplitude or the frequency of the imposed motion in the cylinder, being the main key how close the case (combination of amplitude and frequency of the imposed motion) lays to the lock-in region, and more precisely to the static vortex shedding frequency set by the Strouhal law ($f_{osc}/f_{vs}^o = 1$).

7.4.3 Wake Mode

- $f_{osc}/f_{vs}^o = 0.677$

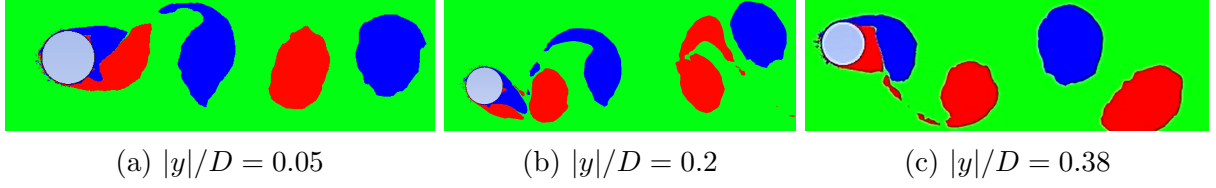


Figure 68: Vorticity (Equation 8) patterns in the wake behind the oscillatory cylinder at $f_{osc}/f_{vs}^o = 0.677$ for three different motion amplitudes: (a) $|y|/D = 0.05$; (b) $|y|/D = 0.2$; (c) $|y|/D = 0.38$. Red color refers to positive vorticity and blue to negative

- $f_{osc}/f_{vs}^o = 0.816$

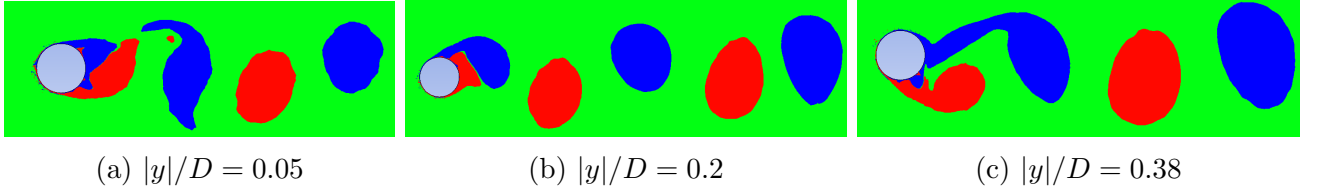


Figure 69: Vorticity (Equation 8) patterns in the wake behind the oscillatory cylinder at $f_{osc}/f_{vs}^o = 0.816$ for three different motion amplitudes: (a) $|y|/D = 0.05$; (b) $|y|/D = 0.2$; (c) $|y|/D = 0.38$. Red color refers to positive vorticity and blue to negative

- $f_{osc}/f_{vs}^o = 1$

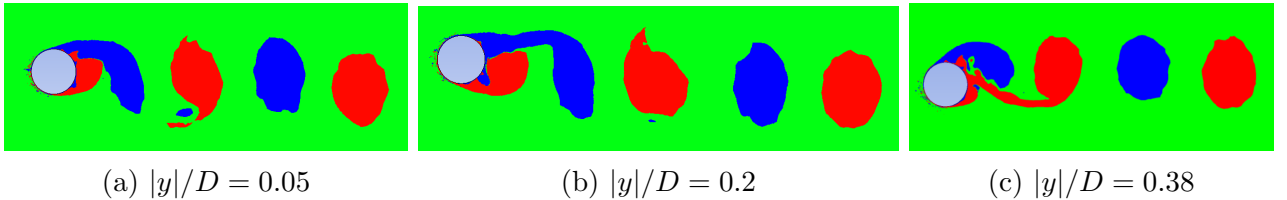


Figure 70: Vorticity (Equation 8) patterns in the wake behind the oscillatory cylinder at $f_{osc}/f_{vs}^o = 1$ for three different motion amplitudes: (a) $|y|/D = 0.05$; (b) $|y|/D = 0.2$; (c) $|y|/D = 0.38$. Red color refers to positive vorticity and blue to negative

Basically, no new conclusions have been taken from this analysis. The only difference between the amplitude analysis at constant frequency and the frequency analysis at constant amplitude is that the forcing parameter is different but the conclusions are the same. The wake patterns depend on where the combination of the motion parameters (f_{osc} and $|y|$) sets the case in the locked-unlocked graph (Figure 51). If the motion results in being locked around $f_{osc}/f_{vs}^o = 1$, a clear 2S vortex shedding will arise. If the case is locked but close to the locked-unlocked transition boundary, there is no well-defined wake pattern but looks like a 2P vortex shedding mode will take place. Eventually, unlocked cases do not have a remarkable vortex shedding mode.

8 Evolution of the Unsteady Pressure over Oscillating Circular Cylinders

8.1 Introduction

The present section will analyse the evolution of the unsteady pressure distribution, $c_p(t)$, over the moving cylinder under different imposed motions (combination of amplitude, $|y|$, and frequency, f_{osc}) at $U_\infty = 4.2786$ [m/s] ($Re \sim 2.9 \cdot 10^4$). The final objective will be setting overall behaviours that differentiates the unsteady pressure loading within the locked-in region and outside of it. The present study could have been introduced in the previous section but it has been decided to pay special focus on it and reserve an individual section as it is at the same time the direct consequence of the after-body wake behaviour and the imposed motion. Moreover, it is the base cause of the lift and drag time signals behaviour over the circular cylinder that have been analyzed previously along the present report.

Keeping the trend of working with non-dimensional parameters, the time evolution of the pressure coefficient (Equation 11) at several points on the surface of the cylinder will be analyzed. The reference values (ρ_{ref} , u_{ref} , p_{ref}) applied on the definition of the non-dimensional parameters will be referred to the inlet boundary of the computational domain.

The results will be plotted against θ [°] angular coordinate defined in Figure 71. θ is null at the front of the circular cylinder and increases clockwise reaching 180 [°] at the rear. The new reference system has been chosen in order to unify the convention set in the current and Martina Lomele's final thesis [68] and enable direct comparison between the results. The comparison will be developed in section 9

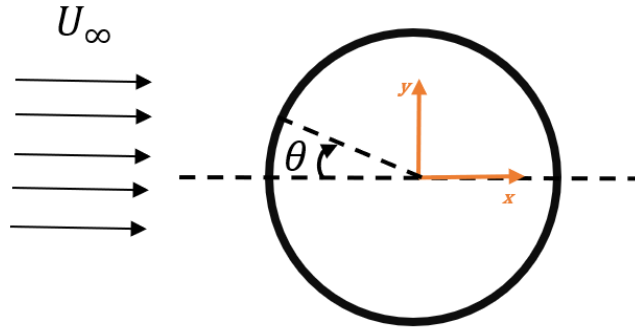


Figure 71: Definition of θ angular coordinate

8.2 Analysis of the time signal of the pressure coefficient

The present study will be a frequency based analysis by means of FFT procedure. The spatial distribution of the component related to 0 frequency will not be discussed. The time mean value has already being analyzed and scrutinized in subsubsection 7.3.3 and subsubsection 7.4.2. The time dependent components are of main interest in the current section.

As it could have been expected beforehand, once all the different combinations of imposed motion presented in Table 23 have been analyzed, two differentiated groups can be defined: locked and unlocked cases. However, in contrary of what has been concluded in section 7, imposed amplitude and frequency were different ways to trigger the same (or similar) consequences, it will be shown that the amplitude of the motion of the cylinder introduces some differences in the frequency content of the resultant time signals amongst unlocked cases.

8.2.1 Locked Cases

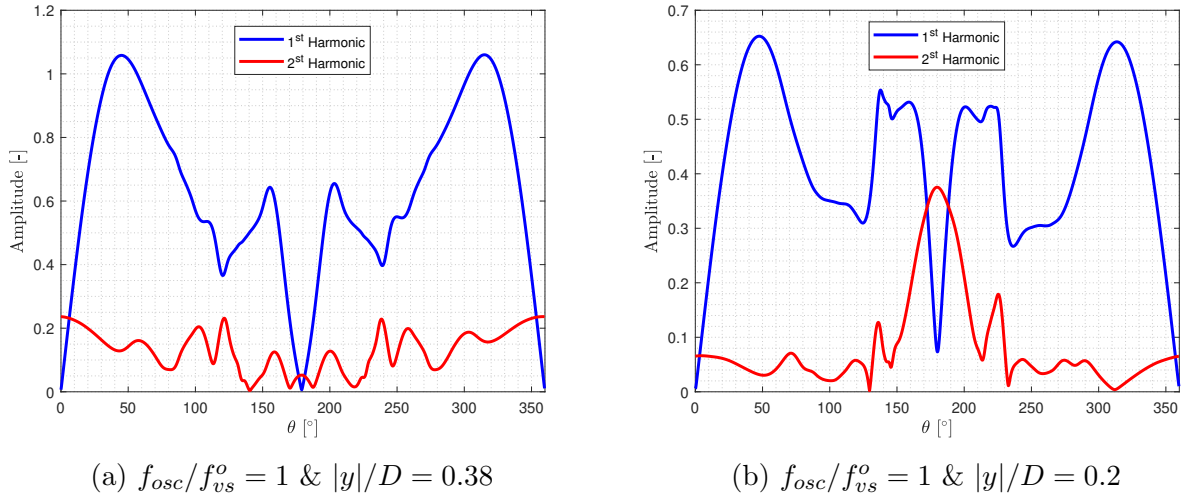


Figure 72: Unsteady components of $c_p(t)$ over the oscillating cylinder with locked vortex shedding at $Re \sim 2.9 \cdot 10^4$. Magnitudes related to 2 frequencies are presented: f_{osc} (blue) & $2 \cdot f_{osc}$ (red). Imposed motions: $f_{osc}/f_{vs}^o = 1$ & $|y|/D = 0.38$ (left) ; $f_{osc}/f_{vs}^o = 1$ & $|y|/D = 0.2$ (right)

The extracted time signals of the pressure coefficient over the cylinder present similar time dependent behaviour. Their frequency content is composed by the frequency of the imposed motion and its multiple upper harmonics, being the greatest part of energy concentrated on the first two harmonics and the steady component. All the spatial distributions of the main frequency component of $c_p(t)$ present close to a symmetric shape; however, it is not. As the vortex shedding pattern of these imposed motions resulted in 2S mode, it was expected this distribution to be symmetric. Two possible reasons arise at this point: (a) 10 vortex shedding periods are not enough to extract the unsteady frequency content of $c_p(t)$ due to the low resolution of the FFT ; (b) The 2D numerical simulation is not able to capture the exact numerical values of $c_p(t)$ over the whole cylinder.

It is remarkable that for locked cases (see Figure 72, Figure 73 & Figure 75) at both, front ($\theta = 0$ [°]) and rare ($\theta = 180$ [°]) of the circular section, the main frequency of the resultant $c_p(t)$ is two times the oscillating frequency. Furthermore, higher multiples of it are completely negligible. However, the amplitude of this component is orders of magnitude lower compare to the static component at the front of the cylinder (discussed in subsubsection 7.3.3) which is understandable as this location corresponds to the stagnation point of the cylinder and to center of the wake.

Regarding the maximum amplitudes of the main component, they are located at $\theta \sim 50^\circ$ and $\theta \sim 310^\circ$ and seem not to change with the imposed amplitudes. It also presents a local peak between $\theta \in [110 - 160] \cup [200 - 240] [^\circ]$ which slightly varies with the parameters of the imposed motion. These coordinates lay close to the local "separation-reattachment" discussed in subsubsection 7.3.3 for the time mean c_p distribution over the cylinder. Actually, it coincides with the re-circulation bubble that switches from the upper to lower part of the cylinder during its vibratory motion.

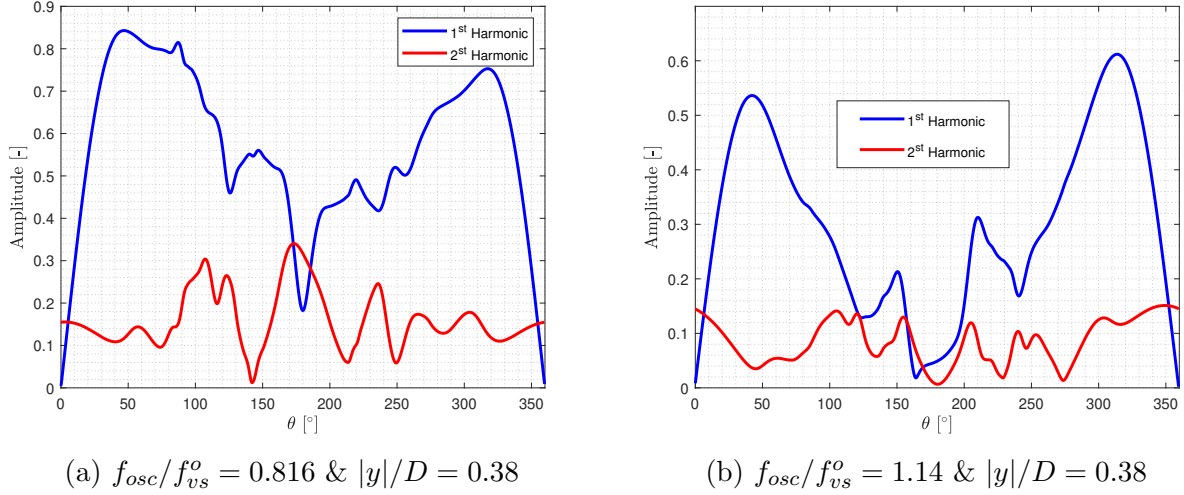


Figure 73: Unsteady components of $c_p(t)$ over the oscillating cylinder with locked vortex shedding at $Re \sim 2.9 \cdot 10^4$. Magnitudes related to 2 frequencies are presented: f_{osc} (blue) & $2 \cdot f_{osc}$ (red). Imposed motions: $f_{osc}/f_{vs}^o = 0.816$ & $|y|/D = 0.38$ (left) ; $f_{osc}/f_{vs}^o = 1.14$ & $|y|/D = 0.38$ (right)

Comparing the locked cases between them, the general trend of the different $c_p(t)$ time signals is similar. However, the closer the imposed frequency (f_{osc}) is to the static vortex shedding frequency (f_{vs}^o), the "cleaner" the signal becomes. "Cleaner" signal means lower content of frequency and smaller magnitude of the components related to higher multiples of the main frequency. Hence, the simulated cases laying close to the unlocked-locked transition boundary present a wider frequency spectrum than the ones near $f_{osc}/f_{vs}^o = 1$, as it happened with $c_L(t)$ in subsubsection 7.3.2. Figure 74 shows the FFT of $c_p(t)$ at $\theta = 50 [^\circ]$ angular coordinate for two different imposed motions of same amplitude. While the 3^{rd} harmonic can barely be distinguished for $f_{osc}/f_{vs}^o = 1$ (Figure 74a), one can identify up to the 5^{th} harmonic for $f_{osc}/f_{vs}^o = 0.82$ in Figure 74b.

Comparing the two imposed motions presented in Figure 72 ($|y|/D = 0.38$ (left) & $|y|/D = 0.2$ (right)), it can be deduced that increasing the imposed amplitude of motion results in the increment in amplitude of the main frequency of $c_p(t)$. Regarding the imposed frequencies of motion, the magnitude of the main frequency of $c_p(t)$ presents the same trend as $c_L(t)$. The amplitude of it increases as getting closer to $f_{osc}/f_{vs}^o = 1$ (see Figure 72a, Figure 73a & Figure 73b).

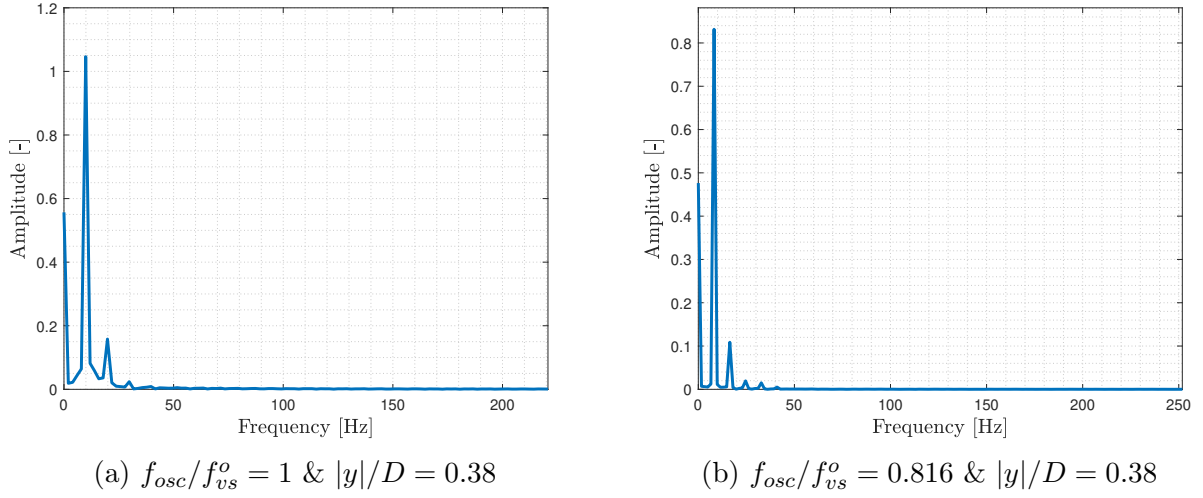


Figure 74: FFT of $c_p(t)$ at $\theta = 50^\circ$ for $f_{osc}/f_{vs}^o = 1$ & $|y|/D = 0.38$ (left) and $f_{osc}/f_{vs}^o = 0.816$ & $|y|/D = 0.38$ (right) imposed motions at $Re \sim 2.9 \cdot 10^4$

Eventually, the imposed motions that result in locked vortex shedding process but lay close to the 'unlocked-locked' transition boundary will be analyzed. section 7 demonstrates even if the component related to f_{osc} of $c_L(t)$ is greater than the one related to f_{vs} (vortex shedding frequency that follows the Strouhal law), both present similar order of magnitude. Figure 75a presents the amplitude of the components related to those frequencies over the cylinder. f_{osc} (blue line) is greater in magnitude compared to f_{vs} (red line) over the cylinder apart from a narrow range of θ values around the rare of the cylinder. Moreover, they present the same order of magnitude over the range $\theta \in (120 - 250)^\circ$. Figure 75b demonstrates that these cases follow the same trend as the rest of locked cases (Figure 72, Figure 73) regarding f_{osc} and upper harmonics of it.

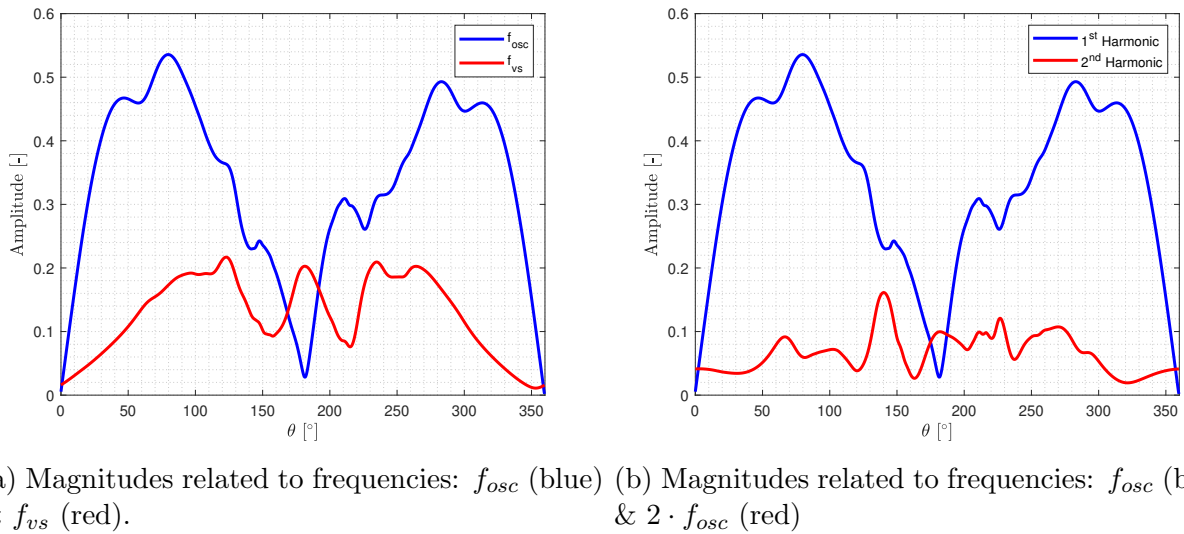


Figure 75: Unsteady components of $c_p(t)$ over the oscillating cylinder with locked vortex shedding at $Re \sim 2.9 \cdot 10^4$. Imposed motion: $f_{osc}/f_{vs}^o = 0.816$ & $|y|/D = 0.2$

8.2.2 Unlocked Cases

The unlocked cases present a general $c_p(t)$ distribution over the cylinder which can be splitted into two differentiated regions in terms of their frequency content (see Figure 76):

- A first region around the front of the cylinder in which the time signal is characterized by the frequency of the imposed motion and its upper harmonics. The order of the higher harmonics (3^{rd} and following) is negligible compare to the steady component and the main frequency.
- A second region (considerably wider in space than the first) in which the time signal is characterized by the frequency of the dynamic shedding frequency (f_{vs}) and its upper or lower harmonics.

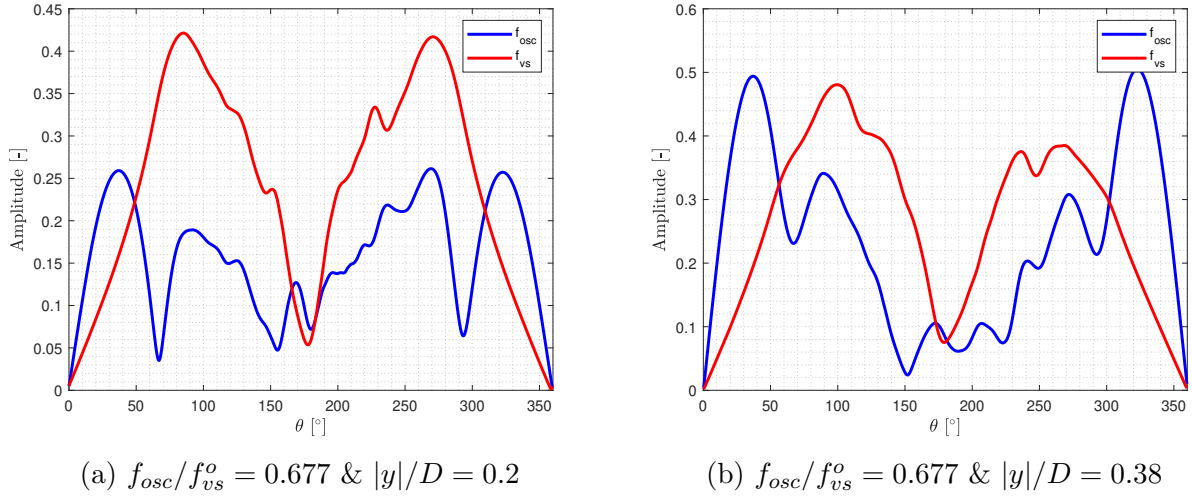


Figure 76: Unsteady components of $c_p(t)$ over the oscillating cylinder with unlocked vortex shedding at $Re \sim 2.9 \cdot 10^4$. Imposed motions: $f_{osc}/f_{vs}^o = 0.677$ & $|y|/D = 0.2$ (left) ; $f_{osc}/f_{vs}^o = 0.677$ & $|y|/D = 0.38$ (right)

Between these two marked regions, there is a transition (range of θ values) in which the $c_p(t)$ time signal contains frequency components of both f_{osc} and f_{vs} of the same order of magnitude. Moving to higher values of θ coordinate, the component related to f_{osc} decreases in magnitude and the one corresponding to f_{vs} arises. At some point, the second overcomes the first. Note that this location will depend of the properties of the imposed motion but it takes places around $\theta \sim 50$ [°] & $\theta \sim 300$ [°] (Figure 76). The extension in which one component or the other is the main one and their magnitudes varies with simulated case (imposed frequency and amplitude of the motion).

This behaviour explains the fact that the time spectrum of $c_L(t)$ for the unlocked cases presents two peaks at those frequencies and the resultant magnitude of each. For the cases of imposed motion that lay closer to the unlocked-locked transition f_{osc} will be the main frequency during

a wider range of θ values which results in a higher magnitude related to this frequency in $c_L(t)$ (Figure 52) and vice-versa.

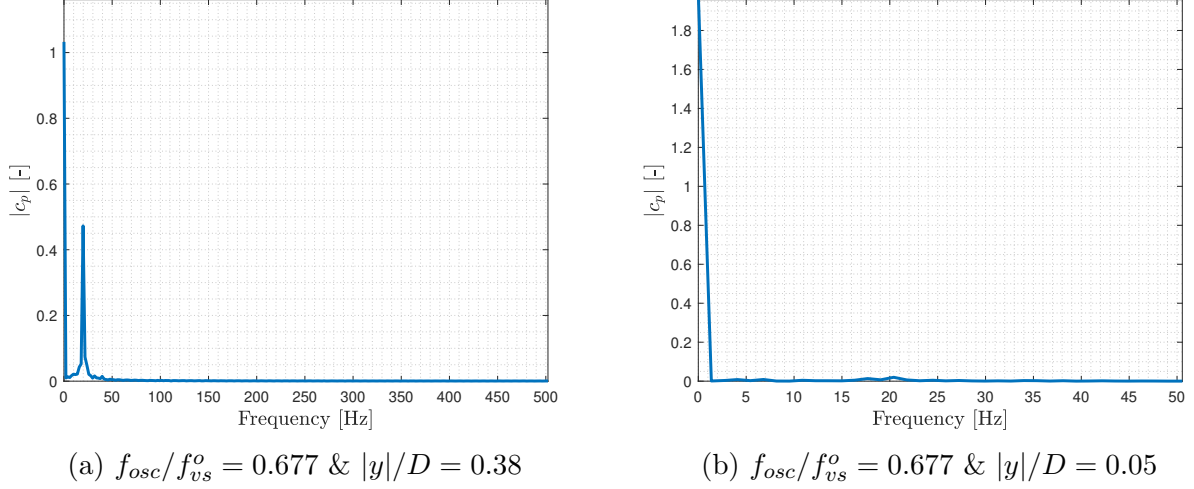


Figure 77: FFT of $c_p(t)$ at $\theta = 0$ [°] for $f_{osc}/f_{vs}^o = 0.677$ & $|y|/D = 0.38$ (left) and $f_{osc}/f_{vs}^o = 0.677$ & $|y|/D = 0.05$ (right) imposed motions at $Re \sim 2.9 \cdot 10^4$

In the same way that the cases laying within the lock-in region, at both front ($\theta = 0$ [°]) and rare ($\theta = 180$ [°]) coordinates of the cylinder section, the main frequency of the resultant $c_p(t)$ is two times the main frequency of the signal (see Figure 77). However, locked cases present the component related $2 \cdot f_{osc}$, whereas unlocked case $2 \cdot f_{vs}$. Furthermore, the rest of the higher multiples of it are completely negligible and the main component is the steady part of the signal (0 [Hz]).

It is remarkable that amongst unlocked cases, if the imposed frequency of motion is small enough (e.g $|y|/D = 0.05$), the component of $c_p(t)$ that corresponds to f_{osc} will never overcome the one set by the Strouhal law (see Figure 78). This behaviour has been identified in both unlocked cases at $|y|/D = 0.05$ ($f_{osc}/f_{vs}^o = 0.677$ and $f_{osc}/f_{vs}^o = 0.816$). However, amongst imposed motions that lay within the lock-in region at that imposed magnitude (see Figure 79) the main frequency is f_{osc} .

The magnitude of the imposed amplitude also affects the oscillatory behaviour of $c_p(t)$. Comparing different imposed amplitudes, $|y|/D$, at the same motion frequency, f_{osc} , a greater value of $|y|$ will result in higher magnitudes of the component related to f_{osc} . Comparing subfigures in Figure 72, one can observed that at $|y|/D = 0.38$ (Figure 72a) the magnitude of the first harmonic barely goes under 0.4 and overcomes unity. At $|y|/D = 0.2$ (Figure 72b), instead, it does never reach unity. Eventually, in Figure 79 it can be seen that at the imposed amplitude of $|y|/D = 0.05$, the same component of $c_p(t)$ barely overcomes 0.5.

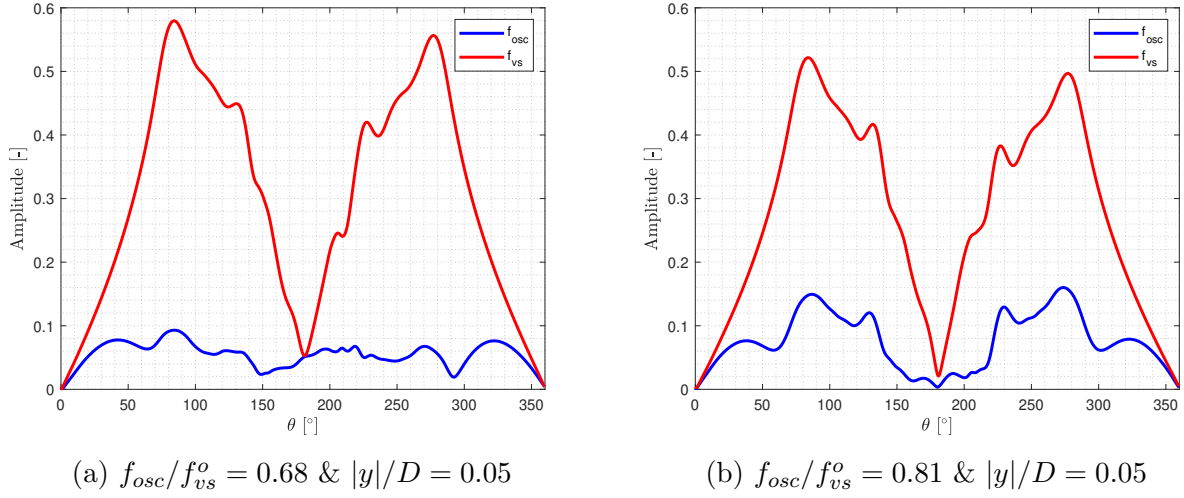


Figure 78: Unsteady components of $c_p(t)$ over the oscillating cylinder with unlocked vortex shedding at $Re \sim 2.9 \cdot 10^4$. Imposed motions: $f_{osc}/f_{vs}^o = 0.68$ & $|y|/D = 0.05$ (left) ; $f_{osc}/f_{vs}^o = 0.81$ & $|y|/D = 0.05$ (right)

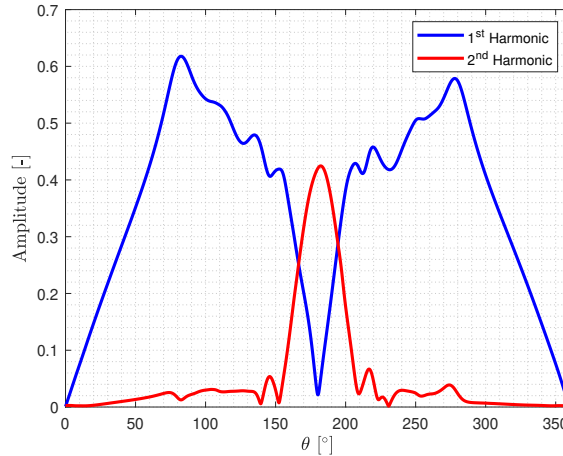


Figure 79: Unsteady components of $c_p(t)$ over the oscillating cylinder with locked vortex shedding at $Re \sim 2.9 \cdot 10^4$. Imposed motion: $f_{osc}/f_{vs}^o = 1$ & $|y|/D = 0.05$

8.3 Conclusions

It has being concluded that in overall the $c_p(t)$ over the cylinder can be divided in two differentiated regions (for both locked and unlocked cases). The first part of the cylinder (narrow range of θ around the front of the cylinder), related to the imposed motion of the cylinder; the second part (wide range of θ that takes most of the cylinder), related to the vortex shedding process.

In the first region of the cylinder, the main component of the time signal of the different locations, is the one related to the frequency of the imposed motion. As moving to the rare of the cylinder, there is a transition until, at some point which varies with the imposed motion, the main component of the signal becomes the shedding frequency. Hence, for the cases laying

within the lock-in region there will not be any transition as the imposed frequency and shedding frequency is identical. The unlocked cases, however, present a transition region in which the magnitude of the motion frequency component decays at the same time as the one related to the shedding frequency gets greater until the second overcomes the first one. This point varies with the imposed motion but lays around $\theta \sim 50$ [°] & $\theta \sim 300$ [°] for the analyzed cases. This behaviour, as discussed before, justifies the frequency content of $c_L(t)$ presented in Figure 52. Depending on the length and magnitude over the cylinder surface whether f_{osc} or f_{vs} is the main frequency, it will affect correspondingly to $c_L(t)$.

In the second region of the cylinder, the time signal is composed basically by the frequency of the vortex shedding process and its multiple higher harmonics.

All the analyzed cases present a interesting behaviour at the front, $\theta = 0$ [°], and rare, $\theta = 180$ [°], locations of the cylinder. The time signal presents a frequency spectrum in which the biggest component is the steady one followed by the 2nd harmonic of the leading frequency over that region.

Eventually, amongst the unlocked cases, when the imposed amplitude of the cylinder is small enough, the component related to the shedding process of $c_p(t)$ presents always higher magnitude than the imposed motion one. However, it cannot be taken as a strong conclusion as it was visualized only at $|y|/D = 0.05$. Amongst the locked cases, instead, a higher imposed amplitude (and constant imposed frequency) results in higher amplitude of the component related to f_{osc} of $c_p(t)$.

9 Comparison between 2D & 3D Results

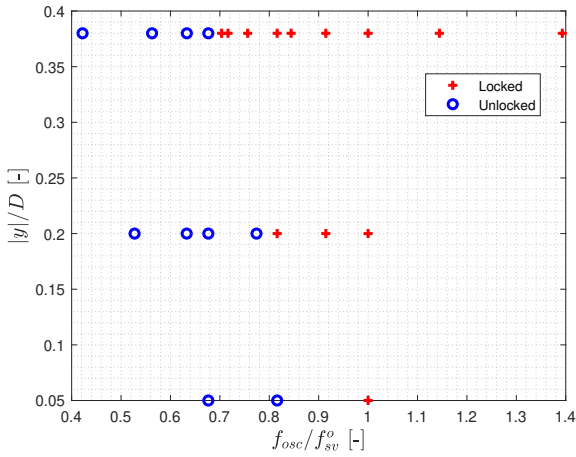
This section aims to compare the 2D results presented in the current report and the ones discussed by Martina Lomele in her final thesis project ('Computational Study of the Unsteady Pressure Around a 3D Circular Cylinder Undergoing Forced Motion') [68].

As described in her report, a 3D computational domain has been built in order to model a 3D circular cylinder with a spanwise length of $L_z = \pi D$. A free-stream velocity of $U_\infty = 4.282$ [m/s] ($Re \sim 2.9 \cdot 10^4$) and an incoming turbulence level of 0.2% has been assumed. The results are extracted from the circular section at mid-span over 7 vortex shedding periods [68].

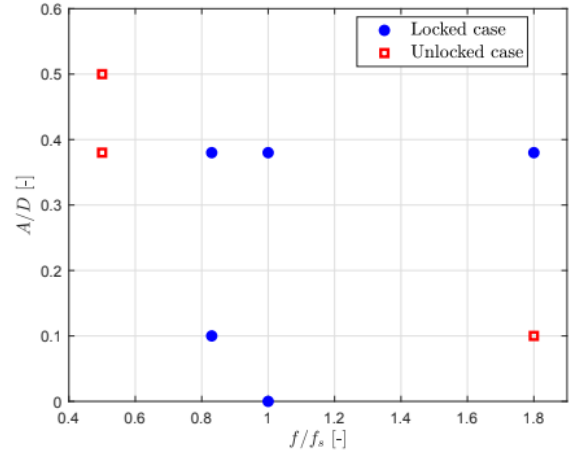
9.1 Lock-in Region

The lock-in region plotted on the imposed motion amplitude-frequency plane (Figure 80) presents similar boundaries in both works. However, as different values of f_{osc} and $|y|$ have been analyzed by the authors, the comparison between the boundaries of the theoretical V shaped lock-in region is not trivial. A greater number of simulated cases (combinations of f_{osc} & $|y|$) would allow a conciser analysis of its shape between the 2D & 3D numerical computations.

As discussed in section 7, both regions (3D & 2D) present a non-symmetric shape of the lock-in region with respect to $f_{osc}/f_{vs}^o = 1$ value. The locked cases extend to higher imposed frequencies on the right side of $f_{osc}/f_{vs}^o = 1$ (higher values of f_{osc}) rather than on the left side (lower values of f_{osc}). Also, both show a wider range of locked frequencies for increasing amplitudes of motion.



(a) Results from 2D domain



(b) Results from 3D domain (mid-span) [68]

Figure 80: Lock-in region for the cylinder oscillation transverse to the incoming flow at $Re \sim 2.9 \cdot 10^4$. Results from 2D domain (left): \circ , unlocked; $+$, locked. Results from 3D domain at mid-span section (right): \circ , locked; \square , unlocked [68]

9.2 Time-varying lift coefficient

The comparison of the resultant unsteady lift coefficient, $c_L(t)$, will be performed in terms of frequency, amplitude and phase difference with respect to $y(t)$ of its main component. The 2D lift coefficient, $c_L(t)$, will be compared against the lift coefficient on the mid-span section of the 3D computations, $C_L(t)$.

9.2.1 Main frequencies of the time signals $c_L(t)$ & $C_L(t)$

Both numerical simulations confirm the results presented by the authors in the literature. On the one hand, the imposed motions that lay within the lock-in region result in a main frequency of the lift coefficient equal to the imposed motion. On the other hand, unlocked cases present two predominant frequencies in the time-varying lift coefficient (see Figure 81). The shedding frequency that follows the Strouhal law, the greatest in amplitude; and the imposed frequency of motion:

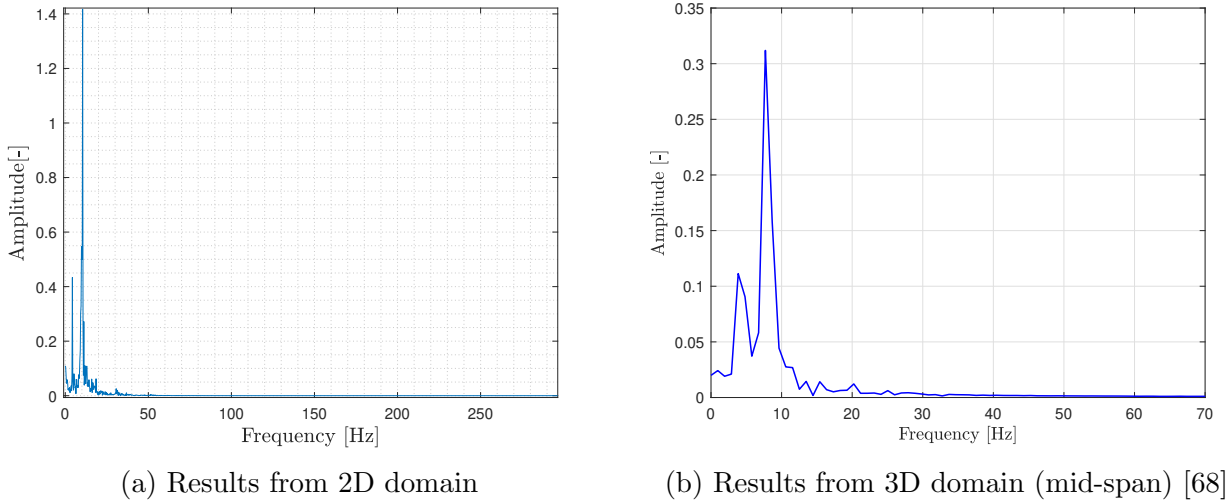


Figure 81: FFT of the lift coefficient for unlocked cases at $Re \sim 2.9 \cdot 10^4$. Results from 2D domain (left): $f_{osc}/f_{vs}^o = 0.4$ & $f_{osc}/f_{vs}^o = 0.38$. Results from 3D domain at mid-span section (right): $|y|/D = 0.5$ & $f_{osc}/f_{vs}^o = 0.5$ [68]

9.2.2 Amplitude of the main frequency: $|c_L|$ & $|C_L|$

Table 25 collects the different resultant $|C_L|$ (amplitude related to the main frequency of $C_L(t)$) values presented in [68] for the numerical 3D computations at $Re \sim 2.9 \cdot 10^4$. These values will be compared to the ones extracted from 2D simulations discussed in section 7 and presented again in Figure 82.

Analyzing the locked cases, two different behaviors of $|C_L|$ can be distinguished. On the one hand, increasing the amplitude of the imposed motion results in higher values of the amplitude related to the main frequency of $C_L(t)$. Same behaviour of $|c_L|$ can be detected in Figure 82b for the case of $f_{osc}/f_{vs}^o \sim$ in 2D simulations. On the other hand, analysing the effect that f_{osc} has on $|C_L|$ a clear difference can be detected between the results obtained from the 2D and 3D simulations. The former, presents a violent increase around $f_{osc}/f_{vs}^o = 1$ and it keeps increasing

in a really low rate (nearly constant) for higher imposed frequencies (see Figure 82a). The later, however, presents its lowest value at $f_{osc}/f_{vs}^o = 1$ (Table 25). This will be the main difference encounter in the project comparing results from 2D and 3D simulations. However, there are only 3 cases of the 3D cylinder at $|y|/D = 0.38$ amplitude available and no concluding remark should be taken as at $f_{osc}/f_{vs}^o = 1.8$, $|C_L|$ keeps increasing with respect to the two lower values of imposed frequency.

f_{osc}/f_{vs}^o	$ y /D$	$ C_L $
0.83	0.38	1.232
0.83	0.1	0.173
1	0.38	1.022
1.8	0.38	1.812

Table 25: Amplitude of the main frequency of $C_L(t)$ for different locked motions at $Re \sim 2.9 \cdot 10^4$. Results at mid-span section of the moving 3D cylinder [68]

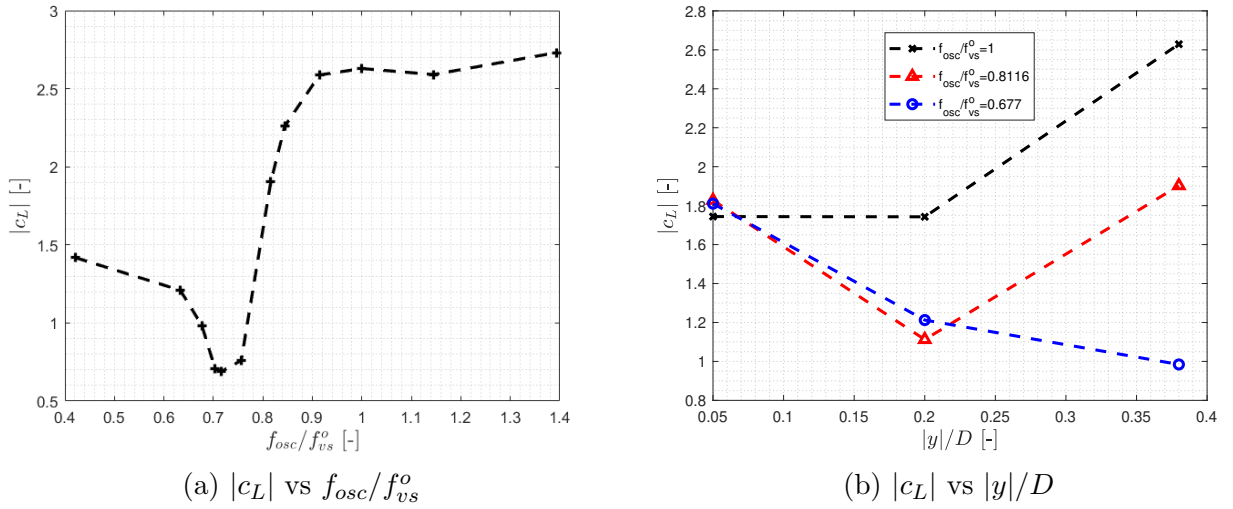


Figure 82: Evolution of the amplitude related to the main frequency of lift coefficient as a function of the imposed frequency (left) and of imposed amplitude (right). Results of 2D cylinder at $Re \sim 2.9 \cdot 10^4$

f_{osc}/f_{vs}^o	$ y /D$	Amp. f_{vs}	Amp. f_{osc}
0.5	0.38	0.312	0.111
0.5	0.5	0.36	0.176
1.8	0.1	1.263	0.2827

Table 26: Amplitude of the main frequency of $C_L(t)$ for different unlocked motions at $Re \sim 2.9 \cdot 10^4$. Results at mid-span section of the moving 3D cylinder [68]

On the other hand, amongst the unlocked cases, two predominant frequencies can be distinguished. One related to the vortex shedding frequency and another to the imposed motion

frequency. Relating the cases presented in Table 26 with Figure 80b it seems that the closer the imposed motion lays to the lock-in region, the higher the amplitude of f_{osc} becomes and lower f_{vs} . Same conclusion was reached in subsubsection 7.3.2 & subsubsection 7.4.1 from the 2D results.

Regarding the numerical values, the results from 2D and 3D simulations result in values of the same order of magnitude even if they are not the same.

9.2.3 Phase difference of the main frequency with respect to $y(t)$: ϕ_L

Table 27 collects the different resultant ϕ_L (phase difference between the main component of $C_L(t)$ with respect to $y(t)$) values presented in [68] for the numerical 3D computations at $Re \sim 2.9 \cdot 10^4$. These values will be compared to the ones presented in Figure 53b & Figure 64b.

f_{osc}/f_{vs}^o	$ y /D$	ϕ_L [°]
0.83	0.38	-58.945
0.83	0.1	93.831
1	0.38	-56.877
1.8	0.38	-4.112

Table 27: Phase difference between main component of $C_L(t)$ and $y(t)$ for different imposed motion at $Re \sim 2.9 \cdot 10^4$. Results at mid-span section of the moving 3D cylinder [68]

As discussed in subsubsection 7.3.2, the results from both computational domains (3D & 2D) can result in a positive or negative values of ϕ_L . The imposed motions closer to the 'unlocked-locked' boundary ($f_{osc}/f_{vs}^o = 0.83$ & $|y|/D = 0.1$ in Table 27) present positive values of it. Moving away from the transition, instead, negative. The same happens in 2D simulations. In terms of numerical values, however, the results from the 3D codes present lower values compared to 2D results in general. While in Figure 53b & Figure 64b the phase difference barely goes under $\phi_L = -50$ [°], values in Table 27 are around $\phi_L = -50$ [°], but always below it.

9.3 Unsteady pressure over the cylinder: $c_p(t)$

As the last step of the comparison between 2D and 3D at mid-span results, the distribution of the amplitude related to the main frequency of the unsteady pressure coefficient over the cylinder will be compared. It is remarkable, that the curves present close to a symmetric distribution around $\theta = 180$ [°] for both 2D and 3D results. Also, the numerical values even if they are not the same, their order of magnitude it is.

On the one hand, the locked cases present similar geometrical distribution over the cylinder showing more or less the same trend with the key points of the spatial distributions about the same θ coordinates (e.g see Figure 83b, 3D, & Figure 84b, 2D). The effect that the variation of the imposed amplitude at constant imposed frequency will be discussed. Also, variation of the imposed frequency at constant imposed amplitude. In both cases, 2D and 3D results, at lower values of $|y|/D$, the amplitude of the main frequency (f_{osc}) decreases as presented in Figure 83a and Figure 84a. This is translated in a decline of the amplitude related to main frequency of lift

coefficient as discussed in subsubsection 9.2.2. However, the variation of the imposed amplitude of motion, produces contrary effects in the results from 2D and 3D simulations. As it happened with the lift coefficient (subsubsection 9.2.2), $f_{osc}/f_{vs}^o = 1$ presents the lowest values in the magnitude of the main frequency of $C_p(t)$ (Figure 83b) in the numerical data extracted from 3D simulations. In contrary, the results from 2D simulation presents close to their maximum value at that imposed motion frequency (Figure 84b). However, there are only 3 cases of the 3D cylinder at $|y|/D = 0.38$ amplitude available and no concluding remark should be taken as at $f_{osc}/f_{vs}^o = 1.8$ the magnitude related to the main frequency of $C_p(t)$ keeps increasing with respect to the two lower values of imposed frequency.

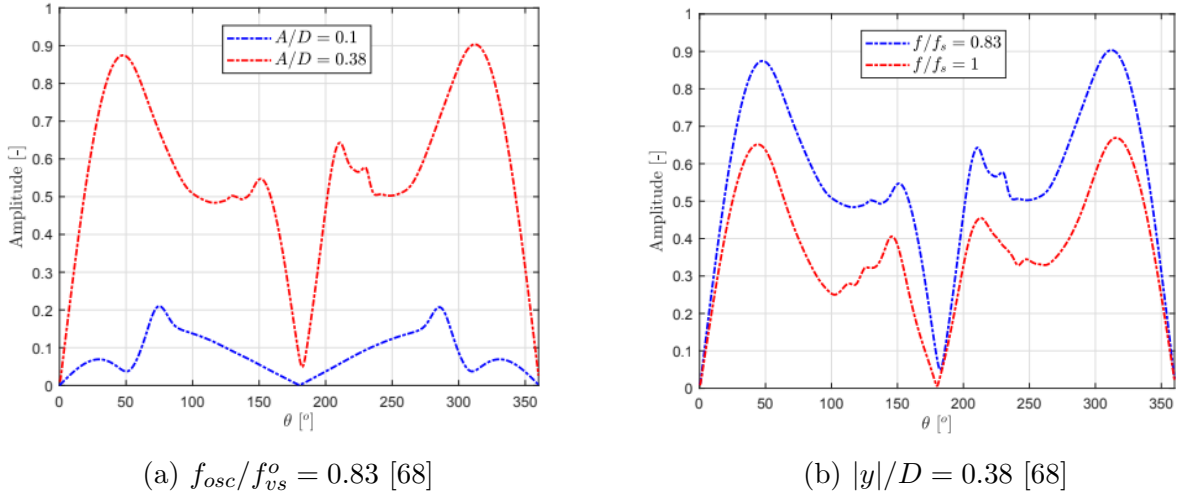


Figure 83: Amplitude of the main frequency of $C_p(t)$ over the mid-span section of the 3D cylinder at $Re \sim 2.9 \cdot 10^4$. Comparison of the effect of the imposed amplitude at $f_{osc}/f_{vs}^o = 0.83$ (left). Comparison of the effect of the imposed frequency at $|y|/D = 0.38$ (right) [68]

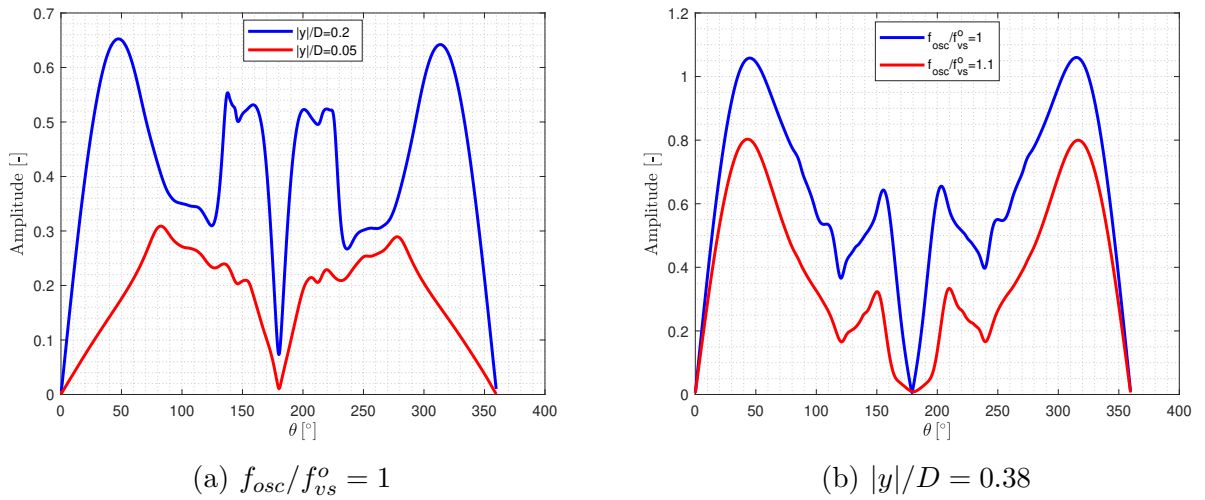


Figure 84: Amplitude of the main frequency of $c_p(t)$ over the 2D cylinder at $Re \sim 2.9 \cdot 10^4$. Comparison of the effect of the imposed amplitude at $f_{osc}/f_{vs}^o = 1$ (left). Comparison of the effect of the imposed frequency at $|y|/D = 0.38$ (right)

On the other hand, amongst the unlocked cases the distribution of the amplitudes related to f_{osc} and f_{vs} will be analyzed. In both results, from 2D and 3D simulations, the components of the time signal related to these frequencies are the predominant. Figure 85 & Figure 86 present the results obtained from different imposed motions with the 3D and 2D computations. Even if the spatial distributions are completely different (the properties of the imposed motion are quite different), the point at which the magnitude of f_{vs} overcomes f_{osc} happens around the same coordinates: $\theta \sim 50 [^\circ]$ & $\theta \sim 300 [^\circ]$.

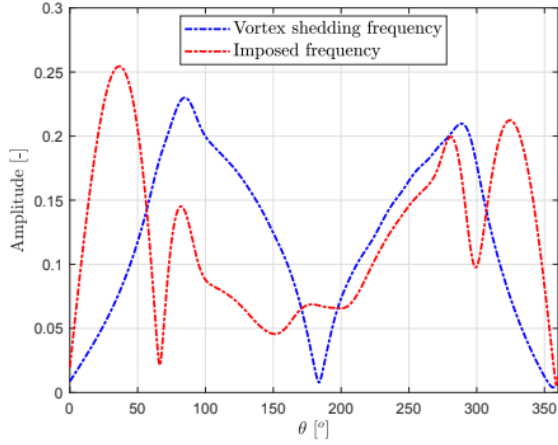
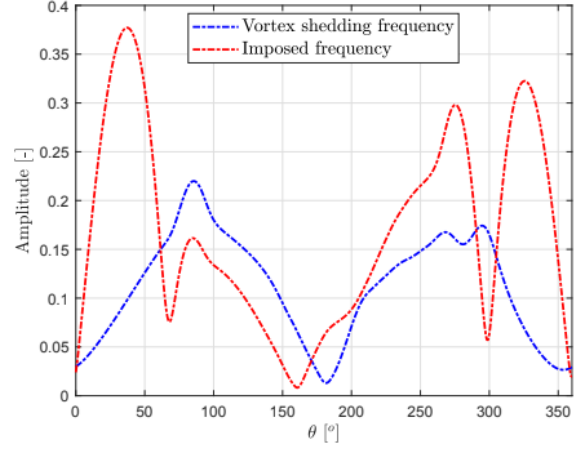

 (a) $f_{osc}/f_{vs}^o = 0.5$ & $|y|/D = 0.38$ [68]

 (b) $f_{osc}/f_{vs}^o = 0.5$ & $|y|/D = 0.5$ [68]

Figure 85: Amplitudes of the predominant frequencies of $C_p(t)$ over the mid-span section of the 3D cylinder at $Re \sim 2.9 \cdot 10^4$. Two unlocked cases are presented: $f_{osc}/f_{vs}^o = 0.5$ & $|y|/D = 0.38$ (left); $f_{osc}/f_{vs}^o = 0.5$ & $|y|/D = 0.5$ (right) [68]

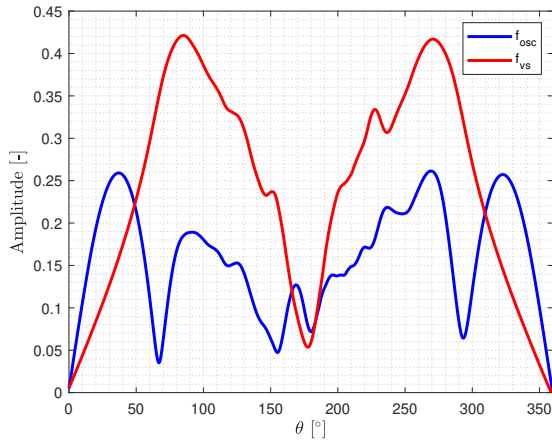
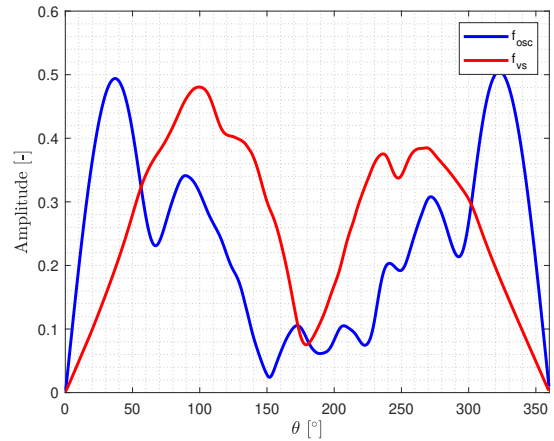

 (a) $f_{osc}/f_{vs}^o = 0.677$ & $|y|/D = 0.2$

 (b) $f_{osc}/f_{vs}^o = 0.677$ & $|y|/D = 0.38$

Figure 86: Unsteady components of $c_p(t)$ over the 2D oscillating cylinder with unlocked vortex shedding. Imposed motions: $f_{osc}/f_{vs}^o = 0.677$ & $|y|/D = 0.2$ (left) ; $f_{osc}/f_{vs}^o = 0.677$ & $|y|/D = 0.38$ (right)

10 Conclusions

The report intends to analyze the evolution of several aerodynamic and aeroelastic parameters, specially focused on the unsteady pressure distribution, over circular cylinders under imposed oscillatory motion in cross direction with respect to the incoming airflow. The prime objective is to characterize the time signals of the pressure over the cylinder in both locked and unlocked cases, as well as, the transition procedure between both situations. Furthermore, the effect of different imposed motions, varying frequency or amplitude, and how they trigger the vortex shedding process at the motion frequency is discussed.

The numerical research has been developed in a sequential manner. First, two CFD codes (flow over static, section 4, and moving, section 6, circular cylinder) have been built and validated against experimental data extracted from ULiege wind tunnel (section 3). Then, the lock-in region has been localized and analyzed based on key aerodynamic and aeroelastic parameters found in literature (section 7). Also, locked and unlocked cases have been compared between them in terms of those parameters. An independent section have been addressed for the analysis of the unsteady pressure time signals in section 8. Locked and unlocked cases have been compared in terms of frequency content and magnitude of their main frequency components.

Eventually, the current numerical two-dimensional research has been developed parallel to Martina Lomele's three-dimensional study and the results from both investigations have been analyzed, compared and discussed at the end of the report.

10.1 Conclusions on the Project

section 4 demonstrates that even after having done the corresponding mesh independence study, the convergence testing of the parameters related to the numerical schemes, and independently of the turbulence model implemented, no two dimensional code is able to well-represent and capture the inherent unsteadiness of the wake region and vortex shedding process from the bluff body. However, the fluid physics over the region of the cylinder where the flow is attached seems to be captured. Furthermore, the Scale Adaptive turbulence models behave in a conciser way rather than URANS models.

section 6 shows that in the case of the moving cylinder, the attached flow over the cylinder is well captured by all the turbulence models tested. Once the separation point is reached, however, the best behaviour is presented by SAS Transition SST turbulence model. It presents a good balance between the accuracy of the results and computational time for the resolution of the problem, even if the time mean pressure coefficient, \bar{c}_p , distribution over the cylinder slightly differs near the rear of the cylinder with respect to the experimental data. It could be due to several imperfections of the experimental set-up (inherent damping of the structure, no perfect 1D motion of the cylinder, surface roughness...) and the no perfectly 2D behaviour of the vortex shedding at the imposed motion conditions. Moreover, the slight difference between the pure sinusoidal motion of the cylinder imposed numerically and the close but not perfectly sinusoidal motion of the cylinder undergoing experimental VIV could introduce some incoherence between both results. In contrary, the numerical value of the vortex shedding frequency is captured.

section 7 locates the lock-in region and analyzes several aerodynamic parameters ($c_L(t)$, c_E , \bar{c}_p and wake pattern) over the locked cylinders. Furthermore, it describes their evolution from unlocked to locked situations being triggered the transition either by increasing the amplitude or the frequency of the imposed motion. It results that all the parameters behave in a similar way, either modifying the imposed amplitude or the frequency on the cylinder, being the main key how close the case (combination of amplitude and frequency) lays to the lock-in region, and more precisely to the static vortex shedding frequency set by the Strouhal law ($f_{osc}/f_{vs}^o = 1$).

The time varying signal of the lift coefficient on the cylinder, $c_L(t)$, of the unlocked cases presents two predominant frequencies: the biggest one at f_{vs} and a lower one at f_{osc} . As the imposed motion gets closer to the synchronization region, the amplitude related to the second frequency increases until it overcomes the first one. At that moment the case will become locked. There is a narrow range of imposed motions that lay close to the unlocked-locked transition boundary at which the frequency content is pretty wide. As moving towards $f_{osc}/f_{vs}^o = 1$, the frequency content of $c_L(t)$ concentrates at $f_{vs} = f_{osc}$ and the amplitude of the lift coefficient increases. Once the frequency of the imposed motion overcomes the static shedding frequency, the frequency spectrum of time signal gets wider again and the amplitude keeps increasing in a really low rate (nearly constant).

Amongst the locked cases two groups can be divided: a narrow range of imposed frequencies and amplitudes laying close to the unlocked-locked transition boundary and the cases around $f_{osc}/f_{vs}^o = 1$. On the one hand, the latter ones present a clear 2S vortex shedding mode and the energy transfer happens from the cylinder to the fluid. On the other hand, the former cases, the energy goes in the opposite direction and the wake mode seems to result in 2P (however, it is not complete clear). Furthermore, the transition between these two modes happens at the same f_{osc}/f_{vs}^o value at which the spatial averaged of \bar{c}_p gets its maximum value, the amplitude related to the main frequency of the lift coefficient, $|c_L|$, presents a steep increase and the phase of it with respect to the motion of the cylinder, $y(t)$, decays abruptly.

Regarding unlocked cases, they do not present a well-defined vortex shedding pattern and the energy transfer between the cylinder and the fluid presents the same direction as the 2S shedding vortex mode does. The direction in which the energy flows, it is specially interesting as it defines if the fluid-structure system is self-excited (air does work on the cylinder) or stable (cylinder does work on the air).

Eventually, the evolution of the spatial distribution of \bar{c}_p has been analyzed in section 7. 3 different situations can be identified: unlocked, locked and transitional cases. As described in subsubsection 7.3.3 each group of cases is characterized by its differentiated properties.

The extensive analysis carried out in section 8 concludes that the $c_p(t)$ distribution over the cylinder in all the cases (locked or unlocked) can be divided in two main spatial regions.

In the first region (front of the cylinder), the main component of the time signal at the different locations, is the one related to the frequency of the imposed motion. Also, higher multiple harmonics of it are present but they can be neglected. As moving to the rare of the cylinder, there is a transition until, at some point which varies with the imposed motion but lays around

$\theta \sim 50$ [°] (upper) & $\theta \sim 300$ [°] (lower), the main component of the signal becomes the shedding frequency. Hence, for the cases laying within the lock-in region there will not be any transition as the imposed frequency and shedding frequency is identical. The unlocked cases, however, present a transition region in which the magnitude of the motion frequency component decays at the same time as the one related to the shedding frequency gets greater until the second overcomes the first one. This behaviour, as discussed before, justifies the frequency content of $c_L(t)$. Depending on the length and magnitude over the cylinder surface whether f_{osc} or f_{vs} is the main frequency, it will affect correspondingly to $c_L(t)$.

In the second region of the cylinder, the time signal is composed basically by the frequency of the vortex shedding process and its multiple higher harmonics.

At the front ($\theta = 0$ [°]) and rear ($\theta = 180$ [°]) of the cylinder, the time signal presents a frequency spectrum in which the biggest component is the steady one followed by the 2^{nd} harmonic of the leading frequency over that region. Furthermore, the order of magnitude of the amplitude of the rest frequencies is negligible compare to it. It is understandable as $\theta = 0$ [°] coincides with the stagnation point and $\theta = 180$ [°] center of the wake.

It is remarkable that amongst the unlocked cases, it seems that when the imposed amplitude of the cylinder is small enough, the component related to the shedding process presents always higher magnitude than the imposed motion one. However, it is not a strong conclusion as this result was only found at one value of imposed amplitude: $|y|/D = 0.05$.

Eventually a comparison between the 2D numerical results presented in the current report and 3D numerical results at the mid-span section (extracted from [68]) has been carried out. Even if inconsistencies arise between the numerical values from the 2D & 3D simulations, the aerodynamic parameters seem to follow the same overall trend. Furthermore, the numerical values present the same order of magnitude.

The prime difference has been detected in the evolution of the magnitude of the main component of the unsteady pressure coefficient (and consequently in the lift coefficient) at constant imposed amplitude and varying the motion frequency amongst the locked cases. It seems that it produces contrary effects in the results from 2D and 3D simulations. On the one hand, an imposed motion of $f_{osc}/f_{vs}^o = 1$ & $|y|/D = 0.38$ presents the lowest values in the magnitude of the main frequency of $C_p(t)$ in the numerical data extracted from 3D simulations. On the other hand, the same imposed motion in 2D simulations shows close to its maximum values of the same aerodynamic property. However, there are only 3 cases of the 3D cylinder at $|y|/D = 0.38$ amplitude available and no concluding remark should be taken as at $f_{osc}/f_{vs}^o = 1.8$ the magnitude related to the main frequency of $C_p(t)$ keeps increasing with respect to the two lower values of imposed frequency.

To sum up, it seems that numerical 2D simulations capture the overall trends of the different aerodynamic and aeroelastic parameters that affect the flow around oscillating cylinders under imposed motion. However, the exact numerical values are not captured and possible inaccuracies could be present in the results. However, compared to the 3D simulations, a considerable reduction of computing time and CPU cost is introduced. Hence, it could be concluded that 2D

simulations, as the one discussed in the current report, present an alternative to 3D simulations or experimental experiments if a great accuracy or precision in the numerical values is not desired and the overall behavior of several aerodynamic parameters as a function of the imposed motion of the cylinder is of interest. However, further research and comparison between different imposed motions should be done, specially around the unlocked-locked transition boundary where the results seem to be more confusing due to the wide frequency content of the time varying signals.

10.2 Further Research on the Topic

The present work opens several paths in which the numerical research of the flow around oscillating circular cylinders under imposed motion can be continued:

- An improved and more extensive validation of the developed 2D CFD code could be carried out. Hence, it would be adequate to compare the computational and experimental data at different airspeeds. Different values of imposed airspeeds will result in the modification of y^+ on the cylinder's wall for each case. It would be necessary to re-mesh the model and test the accuracy of the mesh for each value of U_∞ (or Re) before being able to compare it against the experimental results. Indeed, the turbulence models used in the current report require $y^+ \leq 1$.
- A greater number of imposed motions (combinations of f_{osc} & $|y|$) will give a preciser comparison between the results from 2D and 3D computations. The limited number of simulated imposed motions of 3D cylinders available makes hard to reach solid concluding remarks. However, 3D dynamic computations require great computational time and cost. Also, a higher number of 2D simulations could lead to preciser results and comparison. Moreover, extracting the time dependent parameters over a higher number of vortex shedding periods would possibly increase the accuracy of the results.
- Building an experimental rig of a 3D moving cylinder under imposed motion in a wind-tunnel would be the precisest option to analyze the flow over it. Actually, it was the first approach of the current project; however, the worldwide situation caused by Covid-19 pandemic did not allow it.

A Definition of the Aerodynamic Coefficients

A.1 Introduction

This section introduces the different definitions of the aerodynamic coefficients used along the report. The main challenge is to understand the differences between the difference expressions for the lift coefficient (C_L) and drag coefficient (C_D). The usage of several coefficients is not trivial and it is done to deal with the different data sets that are available (wind tunnel, numerical, numerical from literature and experimental from literature). This is due to the fact that the information available is not the same and a comparison for validation is needed.

First, the pressure coefficient c_p is introduced, which is common for all of them, and how the mean value of the time distribution is obtained. Then, the different definitions and applications of $C_L(t)$ and $C_D(t)$ are discussed. The different aerodynamic coefficients present in the report:

- $c_p(\theta, z, t)$: Pressure Coefficient
- $C_{L_{mo}}(t)$ & $C_{D_{mo}}(t)$: Monitored coefficients by ANSYS Fluent while running the numerical simulations. They are defined by default and they can be 2D or 3D
- $C_L(t)$ & $C_D(t)$: Definitions of the coefficients widely used in the literature
- $C_{L_{exp}}(t)$ & $C_{D_{exp}}(t)$: Coefficients computed from experimental data. They do not contain the component due to the wall shear stress as it is not available
- $C_{L_{ma}}(t)$ & $C_{D_{ma}}(t)$: Numerical expressions defined manually in ANSYS Fluent to compare the obtained values to the results from the Wind Tunnel

A.2 Time Mean Value of the Pressure Coefficient: \bar{c}_p

One of the main aerodynamic parameters that will be used for experimental validation of the numerical codes. The direct disposal of this parameter at 36 discrete points on the cylinder surface and the ability to export it directly (via Time Statistics Section) from ANSYS Fluent ables a simple and rapid procedure of comparison. It is highly desired to avoid exporting the numerical c_p distribution over the cylinder from the commercial software as it is a tedious and time consuming process which depends on the size of the time step used in each simulation. Hence, this process would have been a nightmare when dealing with small time step size in the convergence study. Aiming to avoid the usage of the commercial software as a "Black Box" time step for the discretization was set to solid and equal to the one used in the time integration. This procedure does not allow the software to apply an automatic discretization of the parameters and compute the time mean of them using unknown weighting functions for the user.

$$c_{p_{ij}}(x, y, z, t) = \frac{p_{ij}(x, y, z, t) - p_{ref}}{q_{ref}} = \frac{p_{ij}(x, y, z, t) - p_{ref}}{\frac{1}{2} \rho_{ref} U_{ref}^2} \quad (11)$$

alternatively,

$$c_{p_{ij}}(\theta, z, t) = \frac{p_{ij}(\theta, z, t) - p_{ref}}{\frac{1}{2} \rho_{ref} U_{ref}^2} \quad (12)$$

where,

- x : Streamwise Coordinate
- z : Spanwise Coordinate
- y : Coordinate in the direction of the motion of the cylinder. It is orthogonal to x and z and it compounds the plane that contains the sectional area of the cylinder with x coordinate
- θ : Angular coordinate that starts from the foremost point of the cylinder in x coordinate and goes all around the surface of the sectional area of the cylinder
- i : Spatial discrete points
- j : Temporal discrete points
- p_{ref} : Reference static pressure
- q_{ref} : Reference dynamic pressure
- $p(x, y, z, t)$ & $p(\theta, z, t)$: 3D pressure distribution on the cylinder surface. For 2D and experimental results it will not depend on the spanwise coordinate as in the former z coordinate does not exist and the later is only available at mid-span
- ρ_{ref} : Reference air density
- U_{ref} : Reference airspeed

Eventually, the time mean C_p

$$\bar{c}_{p_i}(\theta, z) = \frac{1}{K} \sum_{j=1}^K c_{p_{ij}}(\theta, z, t) \quad ; \quad \bar{c}_{p_i}(x, y, z) = \frac{1}{K} \sum_{j=1}^K c_{p_{ij}}(x, y, z, t) \quad (13)$$

where j is the time discretization of each discrete spatial value of the pressure coefficient and K is total number of them. In case of experimental data $K = 9000$. In the numerical simulations will depend on the total number of time steps used once the result has converged.

A.3 ANSYS Fluent: Monitored $C_{L_{mo}}$ and $C_{D_{mo}}$

The time evolution of these two aerodynamic parameters are used to verify the convergence of the numerical simulations. The force applied by the fluid on the cylinder is defined in Equation 14

$$\vec{F}_{cylinder}(t) = F_x(t) \vec{x} + F_y(t) \vec{y} + F_z(t) \vec{z} = D(t) \vec{x} + L(t) \vec{y} + F_z(t) \vec{z} \quad (14)$$

where D is the Drag force(Equation 16) and L the Lift force(Equation 15) acting on the cylinder

$$L_j(t) = \sum_{i=1}^M (p_{ij}(\theta, z, t) \cdot n_{y_i}(\theta) \cdot A_i(\theta) + \tau_{y_i}(\theta, z, t) \cdot A_i(\theta)) \quad (15)$$

$$D_j(t) = \sum_{i=1}^M (p_{ij}(\theta, z, t) \cdot n_{x_i}(\theta) \cdot A_i(\theta) + \tau_{x_i}(\theta, z, t) \cdot A_i(\theta)) \quad (16)$$

where

- M : Total spatial discrete points
- n_{yi} : y component of the normal vector on the cylinder at each spatial discrete point
- n_{xi} : x component of the normal vector on the cylinder at each spatial discrete point
- τ_{yi} : y component of the wall shear stress on the cylinder at each spatial discrete point
- τ_{xi} : x component of the wall shear stress on the cylinder at each spatial discrete point
- A_i : Surface area related to each spatial discrete point on the cylinder

Eventually, the monitored lift and drag coefficients by ANSYS Fluent commercial software are shown in Equation 17. These definitions for the aerodynamic coefficients include both pressure and shear forces applied by the fluid flow on the cylinder for their computation. Their usage is limited to the verification of the converge for numerical simulations. No comparison to experimental results can be done as there is no information about the wall shear stress in the latter data.

$$C_{Lmo_j}(t) = \frac{L_j(t)}{\frac{1}{2} \rho_{ref} U_{ref}^2} \quad ; \quad C_{Dmo_j}(t) = \frac{D_j(t)}{\frac{1}{2} \rho_{ref} U_{ref}^2} \quad (17)$$

A.4 C_L & C_D from Literature

Equation 18 shows the widely extended definitions for the aerodynamic coefficients in the literature ([59] [9] [67]). This definition will be used to compare computational 3D results with works of authors of reference. The data extracted from the wind tunnel does not account for the wall shear stresses and only the mid-span c_p distribution over the cylinder is known. Hence, if this data is extended to 3D, uniform c_p distribution in spanwise direction is assumed which is not the real situation and ignoring the dependence on the z coordinate is not correct ([53] [37]). Equation 18 presents the expression and $L_j(t)$ and $D_j(t)$ are extracted directly from ANSYS Fluent [73].

$$C_{L_j}(t) = \frac{L_j(t)}{\frac{1}{2} \rho_{ref} S U_{ref}^2} \quad ; \quad C_{D_j}(t) = \frac{D_j(t)}{\frac{1}{2} \rho_{ref} S U_{ref}^2} \quad (18)$$

where,

- $S = D$ and $A = \frac{\pi D}{M}$ in 2D
- $S = L \cdot D$ and $A = \frac{\pi D}{M} \cdot L$ in 3D
- D : Diameter of the cylinder
- L : Spanwise Length

A.5 Experimental $C_{L_{exp}}$ & $C_{D_{exp}}$

The lift and drag coefficient from the experimental data will be obtained based only in the pressure term that the fluid flow applies on the cylinder. There is not data related to the wall shear stress available (Equation 19 & Equation 20).

$$C_{L_{exp_j}}(t) = \frac{\sum_{i=1}^M (p_{ij}(\theta, z, t) \cdot n_{y_i}(\theta) \cdot A(\theta))}{\frac{1}{2} S \rho_{ref} U_{ref}^2} \quad (19)$$

$$C_{D_{exp_j}}(t) = \frac{\sum_{i=1}^M (p_{ij}(\theta, z, t) \cdot n_{x_i}(\theta) \cdot A(\theta))}{\frac{1}{2} S \rho_{ref} U_{ref}^2} \quad (20)$$

where,

- $M = 36$. Number of pressure taps at midspan
- n_{x_i} & n_{y_i} : x and y components of the normal vector of the circular section of the cylinder at the points where each pressure tap is located.
- $A = \frac{\pi D}{36}$ (2D)
- $A = \frac{\pi D}{36} \cdot L$ (3D)

The time mean values are presented in Equation 21.

$$\bar{C}_{L_{exp}} = \frac{1}{N} \sum_{j=1}^N C_{L_{exp_j}}(t) \quad ; \quad \bar{C}_{D_{exp}} = \frac{1}{N} \sum_{j=1}^N C_{D_{exp_j}}(t) \quad (21)$$

A.6 ANSYS Fluent: Manually Defined $C_{L_{ma}}$ and $C_{D_{ma}}$

In order to compare the numerical values of C_L and C_D to the experimental ones, a new definition was implemented manually which does not contain the force component related to the wall shear stress. The definition of $C_{L_{ma}}$ and $C_{D_{ma}}$ are presented in Equation 22 and Equation 23 :

$$C_{L_{ma_j}}(t) = \frac{\sum_{i=1}^M (p_{ij}(\theta, z, t) \cdot n_{y_i}(\theta) \cdot A(\theta))}{\frac{1}{2} S \rho_{ref} U_{ref}^2} \quad (22)$$

$$C_{D_{ma_j}}(t) = \frac{\sum_{i=1}^M (p_{ij}(\theta, z, t) \cdot n_{x_i}(\theta) \cdot A(\theta))}{\frac{1}{2} S \rho_{ref} U_{ref}^2} \quad (23)$$

Practically, as these parameters will be used for comparison and verification of the experimental data, they will be obtained from the time mean c_p distribution at mid span (Equation 24 & Equation 25).

$$\bar{C}_L = \frac{\sum_{i=1}^M \bar{c}_{p_i}(\theta, z) \cdot n_{y_i}(\theta) \cdot A(\theta)}{S} \quad (24)$$

$$\bar{C}_D = \frac{\sum_{i=1}^M \bar{c}_{p_i}(\theta, z) \cdot n_{x_i}(\theta) \cdot A(\theta)}{S} \quad (25)$$

B Basics of SIMPLE and PISO Algorithms

SIMPLE & PISO algorithms are two of the most extended schemes to solve the pressure-velocity coupling of the incompressible NSE in a segregated manner. Both of them are pressure based predictor-corrector schemes which by means of a modification of the original continuity equation, they apply an additional condition to the pressure field.

Incompressible NSE:

$$\nabla \cdot \vec{V} = 0 \quad (26)$$

$$\frac{\partial \vec{V}}{\partial t} + \vec{V} \cdot \nabla \vec{V} - \nu \nabla^2 \vec{V} = \frac{1}{\rho} \nabla p + \vec{g} \quad (27)$$

The previous system of equations is composed by 4 equations and 4 unknowns (V_x, V_y, V_z, p). The resultant velocity and pressure fields must satisfy both continuity and momentum equations at the same time. Moreover, the continuity equation rather than being an easy equation to solve, it works as a restriction on the computed momentum field [69] [70].

Starting from Equation 26 and Equation 27, an expression for pressure will be derived which will be used as a corrector for the velocity so that it satisfies the continuity equation. Aiming to keep the derivation simple, all the steps related to numerical discretization will be neglected and focused on the main steps to obtain the resultant solution schemes or algorithms. The first step consists in rewriting the momentum equation in matrix form (Equation 28), usually done by means of a finite volume discretization. The coefficients of this matrix \mathcal{M} are all known values.

$$\mathcal{M} \vec{V} = -\frac{1}{\rho} \nabla p \quad (28)$$

At this point, \mathcal{M} matrix will be decomposed into a diagonal matrix, \mathcal{D} , and the residual matrix \mathcal{H} that is left when extracting the diagonal from \mathcal{M} .

$$\mathcal{M} \vec{V} = \mathcal{D} \vec{V} - \mathcal{H} \quad (29)$$

$$\mathcal{H} = \mathcal{D} \vec{V} - \mathcal{M} \vec{V} \quad (30)$$

The point in doing that is on the one hand, a diagonal matrix is really simple to inverse and hence to solve the equation; on the other hand, \mathcal{H} "matrix will allow us to calculate the source term for the pressure equation" [69] [70].

Introducing Equation 29 in Equation 28 and operating, one obtains Equation 33.

$$\mathcal{D} \vec{V} - \mathcal{H} = -\frac{1}{\rho} \nabla p \quad (31)$$

$$\mathcal{D}^{-1} \mathcal{D} \vec{V} = \mathcal{D}^{-1} \mathcal{H} - \mathcal{D}^{-1} \frac{1}{\rho} \nabla p \quad (32)$$

$$\vec{V} = \mathcal{D}^{-1} \mathcal{H} - \mathcal{D}^{-1} \frac{1}{\rho} \nabla p \quad (33)$$

Eventually, combining Equation 33 and Equation 26 one ends up with the Poisson equation:

$$\nabla \cdot \left(\mathcal{D}^{-1} \frac{1}{\rho} \nabla p \right) = \nabla \cdot (\mathcal{D}^{-1} \mathcal{H}) \quad (34)$$

B.1 Pressure-Velocity Coupling Algorithm

The base scheme for both approaches is the same: A pressure based predictor-corrector algorithm. First, the momentum predictor (Equation 28) is solved for the velocity field \vec{V} where the coefficients of \mathcal{M} are known and we do have a initial "guess" (or the previous iteration) of the pressure field. However, \vec{V} does not satisfy the continuity equation yet. Then, \mathcal{H} will be calculated from the previous velocity field.

Now, the pressure field can be computed from Equation 34 which actually satisfies the continuity equation. Eventually, by means of a pressure-corrector stage, the velocity field that satisfies the continuity equation (corrected velocity field) will be extracted directly from Equation 33 using the new pressure field.

After the velocity has been corrected, the pressure field does not satisfy Equation 34 as \mathcal{H} does depend on the velocity and it has been modified. At this point, SIMPLE and PISO algorithms arise.

- **SIMPLE Algorithm:** It goes all the way back until the beginning and solves again the momentum predictor. The resultant \vec{V} it is used to compute a new \mathcal{H} matrix. In other words, it does an "Outer Loop" or "long loop" [70]. The procedure is repeated iteratively until convergence is reached.

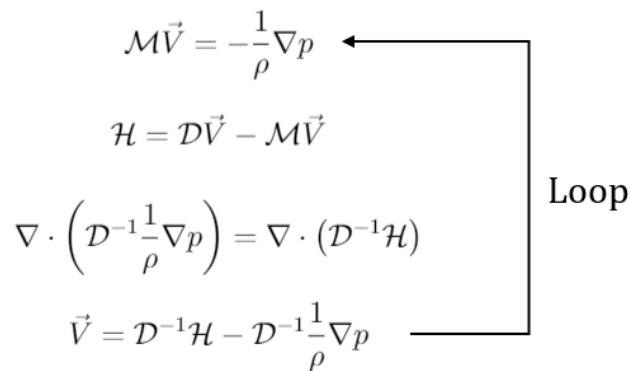


Figure 87: Basic Scheme of SIMPLE Algorithm [70]

- **PISO Algorithm:** Instead of going all the way back and solving the momentum predictor again, it uses the resultant velocity field, \vec{V} , from Equation 33 to update directly \mathcal{H} matrix. In other words, it does an "Inner Loop" or "short loop" [69]. The procedure is repeated iteratively until convergence is reached.

$$\begin{aligned}
 \mathcal{M}\vec{V} &= -\frac{1}{\rho}\nabla p \\
 \mathcal{H} &= \mathcal{D}\vec{V} - \mathcal{M}\vec{V} \quad \leftarrow \\
 \nabla \cdot \left(\mathcal{D}^{-1} \frac{1}{\rho} \nabla p \right) &= \nabla \cdot (\mathcal{D}^{-1} \mathcal{H}) \\
 \vec{V} &= \mathcal{D}^{-1} \mathcal{H} - \mathcal{D}^{-1} \frac{1}{\rho} \nabla p \quad \rightarrow
 \end{aligned}$$

Loop

Figure 88: Basic Scheme of PISO Algorithm [69]

C Derivation of the Scalar Expression for Vorticity

Vorticity is generally defined as the pseudo-vectorial field obtained from the rotational of the fluid velocity (\vec{v}). The resultant field, generally speaking, has three components (3D flows), one component in each direction.

$$\vec{\Omega} = \Omega_x \cdot \vec{i} + \Omega_y \cdot \vec{j} + \Omega_z \cdot \vec{k} = \nabla \times \vec{v} = \left(\frac{\partial w}{\partial y} - \frac{\partial v}{\partial z} \right) \vec{i} + \left(\frac{\partial u}{\partial z} - \frac{\partial w}{\partial x} \right) \vec{j} + \left(\frac{\partial v}{\partial x} - \frac{\partial u}{\partial y} \right) \vec{k} \quad (35)$$

However, in the present case:

- Two dimensional fluid domain. Homogeneous distribution of each velocity component in spanwise (z coordinate) can be assumed: $\frac{\partial u}{\partial z} = \frac{\partial v}{\partial z} = 0$
- Two dimensional fluid flow: z component of the fluid does not exist in the current model: $\frac{\partial w}{\partial u} = \frac{\partial w}{\partial v} = 0$

Hence, Equation 35 will be simplified in Equation 36:

$$\vec{\Omega} = \Omega_x \cdot \vec{i} + \Omega_y \cdot \vec{j} + \Omega_z \cdot \vec{k} = 0 \cdot \vec{i} + 0 \cdot \vec{j} + \left(\frac{\partial v}{\partial x} - \frac{\partial u}{\partial y} \right) \vec{k} \quad (36)$$

Which written in the scalar way is presented in Equation 37. This version of fluid vorticity will be used in the current report to visualize and compare the shedding vortices from the oscillating circular cylinder:

$$\omega = \frac{\partial v}{\partial x} - \frac{\partial u}{\partial y} \quad \left[\frac{1}{s} \right] \quad (37)$$

D Energy Transfer per Cycle

The energy transfer that happens in one oscillatory cycle between the two counterparts of the fluid-structure system is defined as the work done by the fluid on the dynamic structure³:

$$E = W = \int F(t) ds \longrightarrow E_{cycle} = W_{cycle} = \int_o^T F(t) \cdot dy = \int_o^T L(t) \cdot \dot{y}(t) dt \quad (38)$$

Defining the different terms of Equation 38:

$$dy = \dot{y}(t) \cdot dt \quad (39)$$

$$y(t) = |y| \sin(2\pi f_{osc} \cdot t) \quad (40)$$

$$\dot{y}(t) = \frac{dy(t)}{dt} = 2\pi f_{osc} |y| \cos(2\pi f_{osc} \cdot t) \quad (41)$$

$$F(t) = L(t) = \frac{1}{2} \rho U_\infty^2 D c_L(t) = \frac{1}{2} \rho U_\infty^2 D |c_L| \sin(2\pi f_{vs} \cdot t + \phi_L) \quad (42)$$

where,

- $y(t)$ [m]: Imposed sinusoidal displacement of the cylinder in cross direction to the fluid flow
- $\dot{y}(t)$ [$\frac{m}{s}$]: Velocity of the cylinder in cross direction to the fluid flow
- $L(t)$ [$\frac{N}{m}$]: Lift force acting on the cylinder. In other words, the fluid force acting on the cylinder in the direction of its motion, It has being modelled as a pure sinusoidal time signal.
- f_{vs} [Hz]: Frequency of vortex shedding or main frequency of L(t)
- f_{osc} [Hz]: Frequency of the motion of the cylinder in y direction
- ϕ_L [°]: Phase between the motion of the cylinder and L(t)
- $|y|$ [m]: Amplitude of the motion of the cylinder in y direction
- $c_L(t)$ [-]: Time signal of the lift coefficient
- $|c_L|$ [-]: Amplitude of the lift coefficient. It has been modelled as a pure sinusoidal signal
- ρ [$\frac{kg}{m^3}$]: Density of the fluid flow
- D [m]: Diameter of the cylinder
- U_∞ [$\frac{m}{s}$]: Airspeed

³Note that the force component in streamwise direction have been neglected as the motion in that direction is null, and consequently, the work produced by that component of the force. Hence the force is treated as 1D even if in reality is 2D in order to make the mathematical derivation more understandable

- $T = \frac{1}{f_{osc}}$ [s]: Period of the motion of the cylinder

Substituting Equation 39, Equation 40, Equation 41 and Equation 42 in Equation 38, one can obtain the energy transfer per cycle as a function of known parameters (Equation 43):

$$E_{cycle} = \int_0^T \frac{1}{2} \rho U_\infty^2 D |c_L| \sin(2\pi f_{vs} \cdot t + \phi_L) \cdot |y| \sin(2\pi f_{osc} \cdot t) dt \quad (43)$$

Applying general trigonometric rules (Equation 44), Equation 43 can be simplified in Equation 45:

$$\sin(a + b) = \sin a \cdot \cos b + \cos a \cdot \sin b \quad (44)$$

$$\sin(2\pi f_{vs} t + \phi_L) = \sin(2\pi f_{vs} t) \cdot \cos(\phi_L) + \cos(2\pi f_{vs} t) \cdot \sin(\phi_L) \quad (45)$$

$$E_{cycle} = \frac{2\pi f_{osc} |y| \rho U_\infty^2 D |c_L|}{2} \int_0^T \cos(2\pi f_{osc} t) \cdot [\sin(2\pi f_{vs} t) \cdot \cos(\phi_L) + \cos(2\pi f_{vs} t) \cdot \sin(\phi_L)] dt$$

The boxed equation is the general expression for the energy transfer between the fluid and structure in each oscillatory cycle. It can be applied to both unlocked and locked cases in the case of pure sinusoidal $c_L(t)$ signals. However, practically, the resultant $c_L(t)$ from unlocked cases is composed by two main frequencies (f_{osc} & f_{vs}); hence, this approach would not be precise. In contrary, locked cases laying around $f_{osc}/f_{vs}^o = 1$ imposed frequency of motion, present close to a sinusoidal $c_L(t)$ signal. Therefore, this modelling would be an adequate approximation and further simplification can be developed. For locked cases where the vortex shedding happens at the oscillating frequency of the motion : $f_{vs} = f_{osc}$

$$\begin{aligned} E_{cycle} &= \frac{2\pi f_{osc} |y| \rho U_\infty^2 D |c_L|}{2} \int_0^T \cos(2\pi f_{osc} t) \cdot (\sin(2\pi f_{osc} t) \cdot \cos(\phi_L) + \cos(2\pi f_{osc} t) \cdot \sin(\phi_L)) dt = \\ &= \pi f_{osc} |y| \rho U_\infty^2 D |c_L| \left[\int_0^T \cos^2(2\pi f_{osc} t) \cdot \sin(\phi_L) dt + \int_0^T \cos(2\pi f_{osc} t) \cdot \sin(2\pi f_{osc} t) \cdot \cos(\phi_L) dt \right] \end{aligned}$$

where,

$$\begin{aligned} \int_0^{T=\frac{1}{f_{osc}}} \cos(2\pi f_{osc} t) \cdot \sin(2\pi f_{osc} t) \cdot \cos(\phi_L) dt &= 0 \\ \int_0^{T=\frac{1}{f_{osc}}} \cos^2(2\pi f_{osc} t) \cdot \sin(\phi_L) dt &= \frac{1}{2\pi f_{osc}} \left[\frac{2\pi f_{osc} t}{2} + \frac{\sin(4\pi f_{osc} t)}{4} \right]_0^{\frac{1}{f_{osc}}} = \frac{\sin \phi_L}{2 f_{osc}} \end{aligned}$$

Eventually,

$$E_{cycle} = \frac{\pi |y| \rho U_\infty^2 D |c_L|}{2} \sin(\phi_L)$$

(46)

The energy coefficient (c_E) will be defined as the non-dimensional parameter that represents the energy transfer between the solid-fluid medias of the system [45]:

$$c_E = \frac{E_{cycle}}{\frac{1}{2} \rho U_\infty^2 D} \quad (47)$$

Simplified for locked cases:

$$\boxed{c_E = \pi |y| |c_L| \sin(\phi_L)} \quad [-] \quad (48)$$

References

- [1] A. Roshko. “On the drag and shedding frequency of two-dimensional bluff bodies”. In: *NACA Tech. Note N0. 3169* (1954).
- [2] F. Abernathy and R. Kronauer. “The formation of vortex streets”. In: *Journal of Fluid Mechanics* 13 (1962), pp. 1–20.
- [3] R. Bishop and A. Hassan. “The lift and drag forces on a circular cylinder oscillating in flowing fluid”. In: *Royal Society London* 277 (1964), pp. 51–75. DOI: <https://doi.org/10.1098/rspa.1964.0005>.
- [4] J. Gerrard. “The mechanics of the formation region of vortices behind bluff bodies”. In: *Journal of Fluid Mechanics* 25 (1966), pp. 401–413.
- [5] J. Lienhard. “Synopsis of lift, drag and vortex frequency data for rigid circular cylinders”. In: *Technical Extension service, Pullman, Washington* 300 (1966), pp. 1–32.
- [6] C. Feng. “The measurement of vortex induced effects in flow past stationary and oscillating circular and D-section cylinders”. In: *MASc Thesis. Univ. Br. Columbia, Vancouver* (1968).
- [7] J. Batham. “Pressure distributions on circular cylinders at critical Reynolds numbers”. In: *Journal of Fluids and Structures* 57.2 (1973), pp. 209–228.
- [8] J. Mercier. “Large amplitude oscillations of a cylinder in a low-speed stream”. In: *Stevens Institute of Technology, PhD* (1973).
- [9] S. Kacker and B. Pennington. “Fluctuating lift coefficient for a circular cylinder in cross flow”. In: *Department of Mechanical Engineering, The University of Newcastle* (1974).
- [10] M. Davies. “A comparison between the wake structure of a stationary and oscillating bluff body, using a conventional averaging technique”. In: *Journal of Fluid Mechanics* 75 (1976), pp. 209–231.
- [11] T. Sarpkaya. “Vortex-Induced Oscillations: A Selective Review”. In: *Journal of Applied Mechanics* 46.2 (1979), pp. 241–258. DOI: <https://doi.org/10.1115/1.3424537>.
- [12] T. Sarpkaya and R. Schoaff. “Inviscid model of two-dimensional vortex shedding by a circular cylinder”. In: *AIAA Journal* 17 (1979), pp. 1193–1200. DOI: <https://doi.org/10.2514/3.61300>.

- [13] O. Güven, C. Farell, and V. C. Patel. “Surface-roughness effects on the mean flow past circular cylinders”. In: *Journal of Fluid Mechanics* 98.4 (1980), pp. 673–701. DOI: <https://doi.org/10.1017/S0022112080000341>.
- [14] P. Stansby. “A numerical Study of vortex shedding from one and two circular cylinders”. In: *Aeronaut* 32 (1981), pp. 48–71. DOI: <https://doi.org/10.1017/S000192590000901X>.
- [15] D. Gerich and H. Eckelmann. “Influence of end plates and free ends on the shedding frequency of circular cylinders”. In: *Journal of Fluid Mechanics* 122 (1982), pp. 109–121.
- [16] M. Zdravkovich. “Modification of Vortex Shedding in the Synchronization Range”. In: *Journal of Fluids Engineering* 104.4 (1982), pp. 513–517. DOI: <https://doi.org/10.1115/1.3241895>.
- [17] P. Bearman. “Vortex Shedding from Oscillating Bluff Bodies”. In: *Annual Review of Fluid Mechanics* 16 (1984), pp. 195–222. DOI: <https://doi.org/10.1146/annurev.fl.16.010184.001211>.
- [18] P. Bearman. “Vortex shedding from oscillating bluff bodies”. In: *Annual Review of Fluid Mechanics* 16 (1984), pp. 195–222. DOI: <https://doi.org/10.1146/annurev.fl.16.010184.001211>.
- [19] O. M. Griffin and S. E. Ramberg. “The vortex-street wakes of vibrating cylinders”. In: *Journal of Fluid Mechanics* 66 (1984), pp. 553–576. DOI: <https://doi.org/10.1017/S002211207400036X>.
- [20] A. Ongoren and D. Rockwell. “Flow Structure from Oscillating Cylinder Part 1. Mechanisms of phase shift and recovery in the near wake”. In: *Journal of Fluid Mechanics* 191 (1988), pp. 197–223. DOI: <https://doi.org/10.1017/S0022112088001569>.
- [21] C. Williamson and A. Roshko. “Vortex Formation in the Wake of an Oscillating Cylinder”. In: *Journal of Fluids and Structures* 2 (1988), pp. 355–381. DOI: [https://doi.org/10.1016/S0889-9746\(88\)90058-8](https://doi.org/10.1016/S0889-9746(88)90058-8).
- [22] A. Kareem, C. Cheng, and P. Lu. “Pressure and Force Fluctuations on Isolated Circular Cylinders of Finite Height in Boundary Layer Flows”. In: *Journal of Fluids and Structures* 3 (1989), pp. 481–508.
- [23] T. Lee and R. Budwig. “A study of the effect of aspect ratio on vortex shedding behind circular cylinders”. In: *Physics of Fluids* 3 (1990), pp. 309–315. DOI: <http://dx.doi.org/10.1063/1.858140>.
- [24] R. Gopalkrishnan. “Vortex Induced Forces on Oscillating Bluff Cylinders”. In: *MIT Doctoral Dissertation* (1993).
- [25] F. Menter. “Two-Equation Eddy-Viscosity Turbulence Models for Engineering Applications”. In: *AIAA Journal* 32.8 (1994), pp. 1598–1605. DOI: <https://doi.org/10.2514/3.12149>.
- [26] F. Menter and Y. Egorov. “Development and Application of SST-SAS Turbulence Model in the DESIDER Project”. In: *Notes on Numerical Fluid Mechanics and Multidisciplinary Design, Springer* 97 (1994), pp. 261–270. DOI: https://doi.org/10.1007/978-3-540-77815-8_27.
- [27] C. Norberg. “An experimental investigation of the flow around a circular cylinder: influence of aspect ratio”. In: *Journal of Fluid Mechanics* 258 (1994), pp. 287–316.

- [28] T. Sarpkaya. “Hydrodynamic damping, flow-induced oscillations, and biharmonic response”. In: *Journal of Offshore Mechanics and Arctic Engineering* 177 (1995), pp. 232–238.
- [29] F. Hover, S. Miller, and N. Triantafyllou. “Vortex-induced vibration of marine cables: experiments using force feedback”. In: *Journal of Fluids and Structures* 11.3 (1997), pp. 307–326. DOI: <https://doi.org/10.1006/jfls.1996.0079>.
- [30] W. Rodi. “Comparison of LES and RANS calculations of the flow around bluff bodies”. In: *Journal of Wind Engineering and Industrial Aerodynamics* 69.69-71 (1997), pp. 55–75. DOI: [https://doi.org/10.1016/S0167-6105\(97\)00147-5](https://doi.org/10.1016/S0167-6105(97)00147-5).
- [31] J. Frölich et al. “Large Eddy Simulation of Flow around Circular Cylinders on Structured and Unstructured Grids”. In: *Notes on Numerical Flow Simulation I* 66 (1998), pp. 319–338. DOI: <https://doi.org/10.1007/978-3-540-44437-4>.
- [32] S. Jordan and S. Ragab. “A large eddy simulation of the near wake of a circular cylinder”. In: *Journal of Fluids Engineering* 120 (1998), p. 243. DOI: <https://doi.org/10.1115/1.2820640>.
- [33] A. Khalak and C. Williamson. “Motion, forces and mode transitions in vortex-induced vibrations at low mass-damping”. In: *Journal of Fluids and Structures* 13 (1999), pp. 813–851. DOI: <https://doi.org/10.1006/jfls.1999.0236>.
- [34] R. Govardhan and C. Williamson. “Modes of Vortex Formation and Frequency Response of a Freely Vibrating Cylinder”. In: *Journal of Fluid Mechanics* 420 (2000), pp. 85–130. DOI: <https://doi.org/10.1017/S0022112000001233>.
- [35] A. Kravchenko and P. Moin. “Numerical Studies of Flow Over a Circular Cylinder at $Re_D = 3900$ ”. In: *Physics of Fluids* 12.2 (2000), pp. 403–417. DOI: <https://doi.org/10.1063/1.870318>.
- [36] X. Ma, G. Karamanos, and G. Karniadakis. “Dynamic and low-dimensionality of a turbulent near wake”. In: *Journal of Fluid Mechanics* 410 (2000), pp. 29–65. DOI: <https://doi.org/10.1017/S0022112099007934>.
- [37] P. Spalart. “Strategies for turbulence modelling and simulations”. In: *International Journal of Heat and Fluid Flow* 21 (2000), pp. 252–263. DOI: [https://doi.org/10.1016/S0142-727X\(00\)00007-2](https://doi.org/10.1016/S0142-727X(00)00007-2).
- [38] A. Travin et al. “Detached Eddy Simulations Past a Circular Cylinder”. In: *Flow, Turbulence and Combustion* 63 (2000), pp. 293–313. DOI: <https://doi.org/10.1023/A1009901401183>.
- [39] M. Facchinetti, E. de Langre, and F. Biolley. “Vortex-induced waves along cables”. In: *Bulletin of the American Physical Society* 46 (2001), p. 128. DOI: <https://doi.org/10.1016/j.euromechflu.2003.04.004>.
- [40] J. Frölich et al. “Large Eddy Simulation of Flow around Circular Cylinders on Structured and Unstructured Grids II”. In: *Notes on Numerical Flow Simulation II* 75 (2001), pp. 231–249. DOI: <https://doi.org/10.1007/978-3-540-44567-8>.
- [41] M. Matsumoto et al. “Vortex-induced cable Vibration of cable-stayed bridges at high reduced wind velocity”. In: *Journal of Wind Engineering and Industrial Aerodynamics* 89 (2001), pp. 533–647. DOI: [https://doi.org/10.1016/S0167-6105\(01\)00063-0](https://doi.org/10.1016/S0167-6105(01)00063-0).

- [42] J. Franke and W. Frank. “Large eddy simulation of the flow past a circular cylinder at $Re = 3900$ ”. In: *Physics of Fluids* 90 (2002), pp. 1191–1206. DOI: <https://doi.org/10.18869/acadpub.jafm.68.228.24178>.
- [43] E. Guilmineau and P. Queutey. “A numerical Simulation of Vortex Shedding from an Oscillating Circular Cylinder”. In: *Journal of Fluids and Structures* 16.6 (2002), pp. 773–794. DOI: <https://doi.org/10.1006/jfls.2002.0449>.
- [44] C. Norberg. “Fluctuating lift on a circular cylinder: review and new measurements”. In: *Journal of Fluids and Structures* 17 (2003), pp. 57–96.
- [45] J. Carberry, J. Sheridan, and D. Rockwell. “Controlled Oscillations of a Cylinder: forces and wake modes”. In: *Journal of Fluid Mechanics* 538 (2005), pp. 31–69. DOI: <https://doi.org/10.1017/S0022112005005197>.
- [46] S. Dong and G. Karniadakis. “DNS of flow past a stationary and oscillating cylinder at $Re = 10000$ ”. In: *Journal of Fluids and Structures* 20 (2005), pp. 519–531. DOI: <https://doi.org/10.1016/j.fluidstructs.2005.02.004>.
- [47] R. Gabbai and H. Benaroya. “An overview of modeling and experiments of vortex-induced vibration of circular cylinders”. In: *Journal of Sound and Vibration* 282 (2005), pp. 575–616. DOI: <https://doi.org/10.1016/j.jsv.2004.04.017>.
- [48] J. Shao and C. Zhang. “Numerical analysis of the flow around a circular cylinder using RANS and LES”. In: *International Journal of Fluid Dynamics* 20.5 (2006), pp. 301–307. DOI: <https://doi.org/10.1080/10618560600898437>.
- [49] B. M. Sumer. “Hydrodynamics around cylindrical structures”. In: *Advanced Series on Ocean Engineering* 26 (2006). DOI: <https://doi.org/10.1142/6248>.
- [50] G. T. B. Stappenbelt F. Lalji. “Low mass ratio vortex-induced motion”. In: *16th Australasian Fluid Mechanics Conference* (2007).
- [51] M. Young and A. Ooi. “Comparative assessment of LES and URANS for flow over a cylinder at Reynolds of 3900”. In: *Proceedings of the 16th Australian Fluid Mechanics Conference, Gold Coast, Australia* 11 (2007), pp. 41–48.
- [52] O. Inoue and A. Sakuragi. “Vortex shedding from a circular cylinder of finite length at low Reynolds numbers”. In: *Physics of Fluids* 20.033601 (2008). DOI: <https://doi.org/10.1063/1.2844875>.
- [53] S. Behara and S. Mittal. “Flow past a circular cylinder at low Reynolds number: Oblique vortex shedding”. In: *Physics of Fluids* 22.054102 (2010). DOI: <https://doi.org/10.1063/1.3410925>.
- [54] J. You and O. Kwon. “Numerical comparisons between URANS and hybrid RANS/LES at high Reynolds number flow using unstructured meshes”. In: *International Journal of Aeronautical and Space Science* 11 (2010), pp. 41–48. DOI: <https://doi.org/10.5139/IJASS.2010.11.1.041>.
- [55] J.-Y. You and J. Kwon. “Numerical Comparisons Between URANS and Hybrid RANS/LES at a High Reynolds Number Flow Using Unstructured Meshes”. In: *Journal of Aeronautical and Space Sciences* 11.1 (2010), pp. 41–48. DOI: <https://doi.org/10.5139/IJASS.2010.11.1.041>.

- [56] N. Cagney and S. Balabani. “Wake modes of a cylinder undergoing free streamwise vortex-induced vibrations”. In: *Journal of fluids and structures* 38 (2013), pp. 127–148. DOI: <http://dx.doi.org/10.1016/j.jfluidstructs.2012.12.004>.
- [57] N.-S. Cheng. “Calculation of Drag Coefficient for Arrays of Emergent Circular Cylinders with Pseudofluid Model”. In: *Journal of Hydraulic Engineering* 139 (2013). DOI: [https://doi.org/10.1061/\(ASCE\)HY.1943-7900.0000722](https://doi.org/10.1061/(ASCE)HY.1943-7900.0000722).
- [58] M. Mobassher et al. “Experimental and numerical studies of vortex induced vibration on cylinder”. In: *Jurnal Teknologi (Sciences and Engineering)* 66 (2014), pp. 169–175. DOI: 10.11113/jt.v66.2512.
- [59] A. Stamou and G. Papadonikolaki. “Modelling the 3-D flow around a cylinder using the SAS hybrid model”. In: *Global NEST Journal* 16.5 (2014), pp. 901–918.
- [60] S. Chevula. “Aerodynamic loads on bluff bodies under wind gusts”. PhD thesis. 2015. DOI: <https://doi.org/10.13140/RG.2.2.21970.96967>.
- [61] S. Yagmur et al. “Experimental and Numerical Investigation of Flow Structures around Cylindrical Bluff Bodies”. In: *EPJ Web of Conferences* 92 (2015). DOI: <https://doi.org/10.1051/epjconf/20159202113>.
- [62] F. M. Besem et al. “An aeroelastic model for vortex-induced vibrating cylinders subject to frequency lock-in”. In: *Journal of Fluids and Structures* 61 (2016), pp. 42–59. DOI: <https://doi.org/10.1016/j.jfluidstructs.2015.10.009>.
- [63] E. Palkin, R. Mullyadzhannov, and M. Hadziabdic. “Scrutinizing URANS in Shedding Flows: The Case of Cylinder in Cross-Flow in the Subcritical Regime”. In: *Flow, Turbulence and Combustion* 97 (2016). DOI: <https://10.1007/s10494-016-9772-z>.
- [64] E. Palkin et al. “Flow around a confined cylinder: LES and PIV study”. In: *MATEC Web Conferences* 115 (2017). DOI: <https://10.1051/matecconf/201711502010>.
- [65] G. Abeloos et al. *Aeroelasticity Lab report 1*. 2019.
- [66] G. Abeloos et al. *Aeroelasticity Lab report 2*. 2019.
- [67] P. T. Andrianne. *Aeroelasticity and experimental Aerodynamics (Aero0032-1): Lecture 5-Vortex Induced Vibrations*. 2020.
- [68] M. Lomele. *Computational Study of the Unsteady Pressure Around a 3D Circular Cylinder Undergoing Forced Motion*. 2020.
- [69] D. A. W. (M. 101). *PISO Algorithm*. URL: <https://www.fluidmechanics101.com/pages/shop.html>. (accessed: 22.07.2020).
- [70] D. A. W. (M. 101). *SIMPLE Algorithm*. URL: <https://www.fluidmechanics101.com/pages/shop.html>. (accessed: 22.07.2020).
- [71] E. Achenbach and E. Heinecke. “On Vortex Shedding from Smooth and Rough Cylinders in the Range of Reynolds Numbers 6×10^3 to 5×10^6 ”. In: *Journal of Fluid Mechanics* 109 (), pp. 239–251. DOI: <https://doi.org/10.1017/S002211208100102X>.
- [72] D. of Aerospace and M. Engineering. *Wind Tunnel Laboratory*. URL: <http://labos.ulg.ac.be/wind-tunnel-lab/>. (accessed: 01.04.2020).
- [73] A. Inc. *ANSYS Help*. URL: https://ansyshelp.ansys.com/account/secured?returnurl=/Views/Secured/main_page.html?v=194. (accessed: 25.03.2020-01.07.2020).

REFERENCES

- [74] L. McKinney. *Streamlined body. flow follows contours of body: Bluff Body*. URL: <https://slideplayer.com/slide/13063812/>. (accessed: 15.07.2020).